AUS DEM LEHRSTUHL
FÜR UNFALLCHIRURGIE
PROF. DR. DR. VOLKER ALT
DER FAKULTÄT FÜR MEDIZIN
DEN UNIVERSITÄT REGENSBURG

Laser-induced transfer of human mesenchymal cells using near infrared femtosecond
laser pulses for the precise configuration of cell nichoids

Dissertation
zur Erlangung des Doktorgrades
der Biomedizinischen Wissenschaften
(Dr. rer. physiol.)

vorgelegt von
Jun Zhang
aus
Jin Hua

im Jahr
2021

Dekan: Prof. Dr. Dirk Hellwig

Betreuer: Prof. Dr. Denitsa Docheva
Ko-Betreuer: Prof. Dr. Heinz Huber (Hochschule für angewandte
Wissenschaften München)
 Prof. Dr. Hauke Clausen-Schaumann (Hochschule für
 angewandte Wissenschaften München)

Tag der mündlichen Prüfung: 21.12.2021

Zusammenfassung

Tissue Engineering basiert auf der Erzeugung künstlicher Gewebe durch eine Kombination von Zellen und geeigneten, biokompatiblen Materialien, zur Reparatur, zum Ersatz oder zur Regeneration von erkranktem oder beschädigt Gewebe. Die größte Herausforderung bei der Herstellung von funktionellem Gewebeersatz *ex vivo* liegt in der Replikation und Nachahmung der komplexen und einzigartig Gewebemikroarchitektur aus verschiedenen Zelltypen und der extrazellulären Matrix. Die Zellnische im Sehnengewebe beispielsweise ist durch eine strikte hierarchische Organisation von Kollagen-1-Fasern und eingebetteten Sehnenzellen in hochparallelen Reihen gekennzeichnet, die die Basis für die einzigartige und anisotrope Gewebemorphologie der Sehne bilden.

Der Laser-induzierter Zelltransfer ist ein vielversprechender Ansatz für das schnelle Drucken von Biomolekülen und Säugetierzellen mit hoher räumlicher Genauigkeit. Die übertragenen Zellen haben eine hohe Überlebensrate und behalten ihre Fähigkeit zur Proliferation und Differenzierung. Die meisten bisherigen Verfahren benutzen allerdings auf dünne anorganische Opferschichten für die Lichtabsorption, was dazu führt, dass beim Zelltransfer auch Materialspuren dieser Opferschicht mitübertragen werden und das Produkt kontaminieren. In den anderen Fällen werden proteinbasierte Hydrogele wie Gelatine, Matrigel oder Kollagen für die Energieabsorption verwendet. Diese proteinbasierten Absorptionsschichten erfordern jedoch UV-Laserquellen mit Wellenlängen unter 200 nm für eine effektive Energieabsorption, was die Gefahr von DNA-Schäden und Karzinogenese mit sich bringt.

In dieser Arbeit wird ein neuartiges laserinduziertes Bioprinting-Verfahren für den Transfer von Hydrogelen und lebenden Säugetierzellen vorgestellt, z. B. menschliche mesenchymale Zellen, der erstmals sowohl den Einsatz von nicht-biologischen, anorganischen Absorptionsschichten als auch von UV-Laserquellen vermeidet. Um den Transferprozess zu analysieren und die Transferparameter weiter zu optimieren, wurde ein Setup implementiert, das zeitaufgelöste mikroskopische Aufnahmen des Transferprozesses in Seitenansicht ermöglicht. Die Auswirkungen der experimentellen Parameter wie Laserpulsenergie, Fokustiefe, Hydrogel-Viskosität, Laserpulsdauer und sphärische Aberration des Objektivs auf die Kinetik der induzierten Kavitationsblase und des daraus entstehenden Hydrogel-Jets sowie die entsprechende Hydrodynamik wurden systematisch untersucht. Mit zunehmender Jetgeschwindigkeit ändert sich das Jetverhalten: Ist der Jet zu langsam, verbleibt das Hydrogel im Reservoir und es erfolgt kein Transfer. Bei höheren Geschwindigkeiten wird ein laminarer Jet erzeugt, der sich gradlinig zum Akzeptor-Substrat bewegt. Wird Geschwindigkeit weiter erhöht, kommt es zu einem leicht gekrümmten Jet, was die genaue Positionierung beeinträchtigt und schließlich zu einem unkontrollierten Verspritzen des Hydrogels. Um maximale laterale Auflösung auf dem Akzeptor, die dem minimalen Durchmesser des Hydrogelspots entspricht) und damit die beste Positionierungsgenauigkeit (die mittlere quadratische Abweichung der Zellpositionen von einer willkürlich gewählten Zielposition) zu erhalten, sollte möglichst die Schwellenenergie für den Transfer von Hydrogel und Zellen gewählt werden. In diesem Fall ist die kinetische Energie für die Jetausbreitung gerade hoch genug, um die Oberflächenenergie des Hydrogels und die Gravitation zu überwinden, was zu einem Ablösen des primären Tropfens, der die ausgewählten Zellen enthält, vom Hydrogeljet führt und es dem Tropfen anschließend ermöglicht, gegen die Schwerkraft auf den Akzeptor zu gelangen. Zellschädigungen in diesem Prozess, werden möglicherweise durch die sich rasch ausdehnende Kavitationsblase, die Scherkräfte, denen die Zelle bei der Bewegung durch das Hydrogel ausgesetzt ist, und die Kräfte, die durch den Aufprall auf dem Akzeptor entstehen, verursacht. Wir konnten jedoch zeigen, dass solche Zellschädigungen durch die Verwendung des Schwellenwerts deutlich reduziert und minimiert werden können. Zellen, die unter diesen Bedingungen übertragen werden, zeigen Zellüberlebensraten auf dem Zielsubstrat von 93-99%. Sie behalten ihre Fähigkeit zu migrieren und zu proliferieren und zeigen normales, zelltypspezifisches Verhalten nach dem Transfer. Es konnten keine DNA-Doppelstrangbrüche nachgewiesen werden. Für

die Selektion und anschließende Sortierung einzelner Zellen aus heterogenen Zellpopulationen anhand von Zellmorphologie (z. B. Zellform oder -größe) fluoreszierender Marker wurde in das bestehende Transfer-Setup ein inverses Lichtmikroskop integriert. Mit diesem Aufbau konnte eine Positioniergenauigkeit von nahezu 10 µm auf dem Zielsubstrat realisiert werden. Darüber hinaus haben erste Experimente gezeigt, dass mit diesem Aufbau das Verdrucken von Hydrogelen in 3D möglich ist. So konnten wir erfolgreich einen laserbasierten Ansatz zum Aufbau der für die Sehnennische charakteristischen Zellreihenstruktur demonstrieren.

Die Integration eines inversen Lichtmikroskops ermöglicht in Zukunft den Einsatz einer automatisierten Bildanalyse und einer Zellerkennungssoftware, was eine Voraussetzung für einen vollautomatischen Prozess ist. Durch die Verwendung eines Multiplexing-Ansatzes mit schnellen Laserscannern sollen so wesentlich schnellere Zellübertragungsraten erreicht werden, als das derzeit möglich ist. Der in dieser Arbeit vorgestellte Ansatz ermöglicht somit in Zukunft die präzise, schnelle und zellschonende Herstellung von Präzisionsnichoide, 3D-Organoide Zellchips, Organs-on-Chips und letztlich von funktionellem Gewebeersatz.

Abstract

Tissue Engineering is based on the generation of artificial tissues through a combination of cells and suitable, biocompatible materials to repair, replace or regenerate diseased or injured tissue. However, the major challenge in producing functional tissue substitutes *ex vivo* lies in the replication of the complex and unique tissue microarchitecture of native tissue, consisting of different cell types and ECM. The cell niche in tendon tissue, for example, is characterized by a strictly hierarchical organization of collagen-1 fibers and embedded tendon cells in highly parallel rows that form the basis for the unique and anisotropic tissue morphology of the tendon.

Laser-induced cell transfer presents a promising approach for the fast printing of biomolecules and mammalian cells with high spatial accuracy. The transferred cells have a high survival rate and maintain their ability to proliferate and differentiate. Nevertheless, for the absorption of the laser energy, most previous setups relied on inorganic light absorbing sacrificial thin films, and inorganic material was transferred to the printed product along with the cells and contaminates the product. In some cases, protein-based hydrogels, such as gelatin, Matrigel or collagen have been used for energy absorption. However, these protein-based absorbing layers require UV laser sources with wavelengths below 200 nm for effective energy absorption, which brings along the risk of DNA damage and carcinogenesis.

In this thesis, a novel film-free laser-induced bioprinting approach for the transfer of living mammalian cell e.g. human mesenchymal cells is presented, which for the first time avoid both, the use of non-biological, inorganic absorption layers and of UV laser sources. To analyze the transfer process and further optimize the transfer parameters, a laterally time-resolved microscopic setup was implemented to observe the transfer process. The effects of the experimental parameters such as laser pulse energy, focus depth, hydrogel viscosity, laser pulse duration and spherical aberration of the microscope objectives on the cavitation bubble formation and jet kinetics and the corresponding hydrodynamics have been systematically investigated. As the jet velocity increases, the jet behavior changes: if the jet is too slow, the hydrogel remains in the reservoir and no transfer occurs. At higher speeds, a laminar jet is generated which moves in a straight line to the acceptor substrate. As the velocity increases further, a slightly curved jet occurs, which affects accurate positioning and eventually leads to uncontrolled splashing of the hydrogel. To obtain the maximum lateral resolution (hydrogel spot diameter) and best positioning accuracy (the root mean square deviation of the cell positions from an arbitrary chosen target position), the threshold energy for hydrogel and cell transfer should be selected. In this case, the kinetic energy for the jet propagation is just high enough to overcome the hydrogel surface energy and gravity, resulting in a breakup of the primary droplet containing the selected cells and subsequently allowing the droplet to reach the acceptor. The mechanical stress from the expanding cavitation bubble, shear forces, as cells are moving through the hydrogel, and forces caused by the impact of landing on the acceptor are believed to be the key source of cell damage. However, we could show that cell damage could be significantly reduced and minimized by using the threshold transfer conditions. Under threshold conditions, the transferred cells have 93–99% survival rates on a target substrate. They maintain their ability to migrate and proliferate, and show normal, cell type specific behavior after transfer. No DNA double strand breaks could be detected. In addition, the transfer setup was integrated into an inverted optical microscope, which allowed to select and sort individual cells from heterogeneous cell populations, based on cell morphology (e.g. cell shape or size) or fluorescence markers and to position them on the target substrate with a positioning accuracy close to 10 µm. Thus, we could successfully demonstrate a laser-based approach to build the cell row structure that is characteristic of the tendon niche.

After all, our hydrogel bioprinting approach can readily be extended from 2D into 3D. The integration into an inverted optical microscope setup, will allow for the use of automated image analysis and a cell recognition software in the future, which is a prerequisite for a fully automated process. By using a

multiplexing approach with fast laser scanners, one can envision much faster cell-transfer rates in the future than currently possible. The approach presented in this thesis will thus enable the precise, fast, and cell-friendly fabrication of precision nichoids, 3D organoids, cell-chips, organs-on-chips, , and ultimately of functional tissue substitutes in the future.

Table of Contents

2

1 Introduction

Preface: Parts of this thesis have been published in peer reviewed journals (the exact articles are listed on pages 4 and 5) and the text from these articles displays in *italic font* throughout the thesis.

Tissue Engineering has been developed with a broad range of applications that aim to repair, replace or regenerate diseased, injured or whole tissues (i.e., bone, cartilage, tendon, blood vessels, muscles, skin, bladder etc.). However, at present, the major challenge in producing functional tissue substitutes *ex vivo* lies in the replication of the complex and unique tissue microarchitecture of native tissue, consisting of different cell types and extracellular matrix (ECM) (1–3). For example, at the cellular level, tendon cell niche, is characterized by a strictly hierarchical organization of collagen-1 fibers and embedded tendon cells in highly parallel rows that form the basis for the unique and anisotropic tissue morphology of the tendon, while in cartilage tissue, cells are positioned in columns embedded in isotropic collagen type II-rich matrix (4). To engineer tendon or cartilage tissue, the establishment of appropriate cell–matrix and cell-cell contacts is therefore critical to obtain functional tissue mimetic constructs (5).

"*The fabrication of three-dimensional tissue substitutes will improve the treatment of lesions caused by injuries or diseases, as well as age-related tissue degeneration,* for example, the degeneration of tendon and articular cartilage tissues (6–9)*. Additionally, it has the potential of providing more relevant 3D test systems for drug development* (6,9–11) *and new insights into how cells interact with their environment and with one another* (8,12,13)*. In vivo, cells receive multiple biological, chemical and physical stimuli from neighboring cells, the ECM and the surrounding tissue. Cell behavior and fate crucially depend on these stimuli, many of which originate from their direct cell vicinity* (14–18)*. Controlling the cellular microenvironment in vitro with single cell precision is therefore an important factor for the generation of instructive cell environments and cell niches, which stimulate cells to migrate, differentiate, proliferate and to form functional tissue* (19)*.*

The introduction of such detailed microenvironments will advance the fabrication of cell chips and organs-on-chips and provide a better understanding of cell-matrix and cell-cell interactions under normal and pathological conditions (19–21)*. However, suitable tools which*

allow a cell-friendly, fast and reliable transfer of living mammalian cells with single cell precision onto 2D and 3D structures are still scarce". The text is obtained from the article (22).

1.1 Laser-based bio-printing

Laser-induced forward transfer (LIFT) presents a promising approach for the fast printing of biomolecules and mammalian cells with high spatial accuracy. This technique has been successfully applied to a variety of cell types, including MG63 human osteosarcoma cells, P16 pluripotent embryonal carcinoma cells, skin cell lines (fibroblasts/keratinocytes), human mesenchymal stem cells (hMSCs), EA.hy926 human endothelial cells, B35 neuroblasts, and others (23–29). LIFT has become an important tool for the fast and gentle 3D-printing of cells, with superior cell survival rates above 95% (30–33). *"It was originally developed to transfer inorganic materials from a thin donor film to an acceptor surface through a transparent support (34,35). In recent years, it was demonstrated that LIFT is also possible for printing liquid and therefore has been applied to biological material as an alternative bio-printing technology (33). It can overcome some of the drawbacks of the more conventional ink-jet printing, pipetting, or micro-extrusion based technologies, such as clogging of the printing nozzles, or high shear forces. Because printer parts do not come into direct contact with printing material, cross-contamination of different materials can easily be avoided. In addition, due to the high repetition rates of pulsed laser sources, laser printing has the potential for high transfer rates and fast processing times. In the past, biomolecules (23) like proteins (36,37) or DNA (36,38,39), as well as mammalian cells (24–27,40–42) have been successfully transferred through laser-induced printing with almost no loss of bioactivity".*

In a typical setup for laser-induced cell transfer, the transparent substrate is coated with a sacrificial layer such as gold, titanium (24,25,27,40) for the laser energy absorption, or a UV light-absorbing polymer (43–45). The cell-containing hydrogel is deposited onto the absorbing layer with a typical thickness of about 100 μm. By focusing a nanosecond (ns) pulsed laser through the transparent substrate onto the absorbing layer, which is evaporated by the energy of the incoming pulse, resulting in a high gas pressure, which propels the cell-laden hydrogel in a jet towards an acceptor surface. The transferred cells usually display a high viability and maintain their ability to proliferate (25,40,41). Scaffold-free 3D cell microstructures for the study of cell-cell interactions and tissue engineering applications have

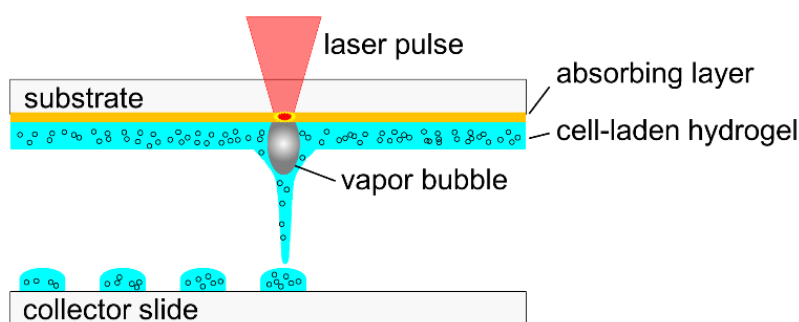*been successfully fabricated in this manner (24,25,40)"*. The text is obtained from the article (22).

Figure 1.1 Schematic setup of laser-induced cell transfer with absorbing layer.

"One drawback of the laser-based transfer for bioprinting applications, is the fact that the material from the energy absorbing layer can also be transferred along with the printed biomaterial, thus contaminating the printed constructs, where it can be found in the form of nanometer-sized and larger fragments and particles (36,46). To avoid contamination of constructs with inorganic material, protein-based hydrogels, such as Matrigel or collagen hydrogels, have been used as the light-absorbing layer (45) in matrix-assisted pulsed-laser evaporation direct writing (MAPLE DW) (41,47,48). Nevertheless, these approaches are limited to UV laser irradiation, such as emitted from argon fluoride excimer lasers (193 nm), because they rely on the effective UV absorption of proteins at 200 nm wavelength and below (49). However, at these wavelengths, UV light may also cause severe DNA damage, including double-strand breaks (45) and photochemical crosslinking, which may both lead to cell death or carcinogenesis (50)". The text is obtained from the article (22). Lots of previous works demonstrated that the printing parameters including the laser sources (wavelength, pulse energy, pulse duration) and the properties of the bioink, such as the type of the hydrogel, the viscosity and the thickness of the layer can significantly affect the jet dynamics and printing quality (44,51–53). A lot of hydrogels, such as alginate (25,54), cell culture medium (55), collagen (56) and fibrinogen (24) have been used as bioink. Preparation of a uniform and stable bioink into a thin film with a typical thickness of about 100 μm is not easy to perform (57). Additionally, if the transfer process is carried out under dry environmental conditions, the drying of the bioink is inevitable and can furthermore affect the printing reproducibility and quality (52,54). A previous study demonstrated that the rheological properties of bioink can also be varied by embedding living cells into the bioink, which results in non-ideal jet behavior because of inhomogeneous cell distribution and cell aggregation (58). There is not

4

one bioink that can be used for all applications, as it needs to be compatible with cells and with the desired structure to be printed (59). A real-time visualization of the printing process is required for optimization of jet dynamics and printing quality either by using a high-speed camera (52) or by using the pump-and-probe principle in combination with short illumination pulses (60,61). The selection and optimization of laser printing parameters including laser source, absorbing layer, bioink and cell type is costly and time-consuming (53,59). Until now, there is no reliable laser-assisted bioprinting technique enabling efficient and precise printing of living cells at the single cell precision from the thin bioink layer.

Non-linear optical effects can be used as an alternative approach to avoid both, the use of non-biological, inorganic absorption layers and of UV laser sources. By tightly focusing a near-infrared (NIR) ultrashort laser pulse into a transparent material, nonlinear optical interactions such as self-focusing and multi-photon absorption create a controlled optical breakdown with a few micrometers diameter, in which the laser pulse is absorbed without the need for a light absorbing layer (62–67). In addition, the near-infrared window is used, at wavelengths with minimal interaction of electro-magnetic radiation with biological materials (49,50) and thereby the risk of inducing photochemical DNA damage is avoided. In aqueous media, the high-pressure plasma generated by the ultrashort laser pulses forms a rapidly expanding cavitation bubble (65,68). If the femtosecond laser pulse is focused between 50 μm to 100 μm underneath the liquid surface, the cavitation bubble can be used to propel a water or hydrogel jet, which is subsequently ejected from the free liquid surface (60,69–71). The laser pulse energy can convert into kinetic energy for the jet propagation, avoiding a significant heat transfer to the surrounding medium (65,72). Current applications of this technique, which mainly focus on the controllable and reproducible transfer of biomolecules like proteins and DNA, showed no loss of bioactivity (57,60), indicating that this approach might also be feasible for the printing of living cells. However, so far, no living mammalian cells have been printed with this technique yet.

As indicated in the preface, parts of this thesis have been published in peer reviewed journals in advance in the following articles and the text from these articles displays in *italic font* throughout the thesis:

-       Zhang et al., "**Sacrificial-layer free transfer of mammalian cells using near infrared femtosecond laser pulses**" PloS One, 2018, see reference (73) of this thesis.

- Zhang et al., "**Single Cell Bioprinting with Ultrashort Laser Pulses**" Advanced Functional Materials, 2021, see reference (22) of this thesis.

Two additional manuscripts containing results of this thesis will be submitted to peer reviewed journals:

- Zhang et al. "**Single-cell bioprinting by using femto- and picosecond laser pulses**" (to be submitted to Special Issue "Advanced Laser Bio-Printing" in Micromachines)

- Zhang et al, "**Jet dynamics study of femtosecond laser-induced single-cell printing**" (manuscript in preparation)

The results of my previous colloquia submitted to the faculty of medicine of the University of Regensburg are included in this thesis.

Results of bachelor and master students under my supervision (project's / bachelor's / master's theses), which were submitted to the Department of Applied Sciences and Mechatronics of Munich University of applied sciences, are included in this thesis: Patrick Byers established the upright time-resolved configuration in his bachelor thesis (chapter 3.1.1), Christine Frank implemented some of the time-resolved experiments with various on laser pulse energies and focus depths as an intern (chapter 3.1.4 and 3.1.5), Levin Schulte-Spechtel worked on the 3D Bioprinting in his internship report (chapter 3.4.4), Sasa Djordjevic investigated the comparison of upright and inverted configuration in his master thesis (chapter 3.2.2) and Yasemin Geiger established experiments for Bioprinting depending on pulse duration in her projects study (chapter 3.2.3).

1.2 Hypothesis and goals

The **main hypothesis** of the doctoral study is that the film-free femtosecond laser-induced transfer approach can be used to transfer micro-droplets containing single or multiple mammalian cells, specifically of mesenchymal origin, with high survival rates. To test this hypothesis, a novel setup for the printing of living cells using femtosecond NIR laser pulses was established.

The **main goals** of the doctoral study were defined as follows:

1. Establishing a cell-friendly and easy to use bioprinting technology for selecting and printing living cells with single cell precision and high cell viability.

2. Establishing a time-resolved imaging setup for visualizing the transfer process to investigate and optimize the effects of the experimental parameters on the cell viability and the printing precision.

3. Creating a 2D cell configurations or precision cell nichoids with single cell precision.

Doctoral thesis organization:

The mechanisms of the film-free laser-induced transfer and the hydrodynamic analysis of the jet propagation are given in **chapter 2 "Materials and Methods"**, where the protocols for the sample preparation and for assessing the viability and behavior of the transferred cells (e.g. live-dead assays, time-lapse microscopy, and immunofluorescence staining) are described.

The obtained results are presented in **chapter 3**. The analysis of the transfer process and the further optimization of the transfer parameters (upright configuration) are given in **chapter 3.1**. We successfully combined the NIR laser with an optical setup, enabling time-resolved microscopy for observing the transfer process of cell-free and cell-laden hydrogel. We systematically investigated the influence of laser pulse energy and focus depth on the jet dynamics.

Chapter 3.2 contains the integration of the transfer setup into an inverted optical microscope, which allowed us to select and sort individual cells from heterogeneous cell populations, based on cell morphology (e.g. cell shape or size) or fluorescent labelling. Here we also compared the fs laser-induced transfer process in the upright and the inverted configuration. In addition, we analyzed the influence of the laser pulse duration and the hydrogel viscosity on the jet dynamics.

High survival rates and good cell viability are key parameters for biofabrication techniques in tissue engineering. In **chapter 3.3** are included our results regarding the effects of laser pulse energy, focus depth, laser pulse duration and the applied microscope objectives on the cell viability after the transfer. The optimization of these parameters as well as examples of bioprinting applications are presented in **chapter** 3.4.

Chapter 4 discusses the main results, the hydrodynamics of the transfer process, namely the difference between the cell-free and cell-laden jet dynamics, and the potential causes of cell damage in this bioprinting technique.

2 Materials and Methods

2.1 Mechanisms of the film-free femtosecond laser-induced printing

An optical breakdown can be generated by focusing an ultrashort laser pulse in transparent and weakly absorbing liquids. This method has been used as microsurgical tool with a highly confined localized tissue damage (65,66). The collimated laser beam can be focused by a microscope objective with a numerical aperture (NA):

$$NA = n \cdot sin\theta \approx \frac{D}{2 \cdot f} \tag{1}$$

where n is the medium refractive index, θ is the maximal half-angle of the cone of light, f is the focal length and D is the objective entrance pupil diameter. For the best focus ability it is recommended to overfill the aperture of the objective by about 30%. When focusing an ideal Gaussian beam the focal spot diameter $2\omega_0$ can be calculated as:

$$2\omega_0 = \frac{4 \cdot f}{\pi \cdot D}\lambda \approx \frac{2 \cdot \lambda}{\pi \cdot NA} \tag{2}$$

where ω_0 denotes the laser beam radius at the focal plane, measured at $^1/_{e^2}$ intensity level and λ is the vacuum wavelength of laser beam. The laser radial intensity distribution of a Gaussian profile can be expressed as follows:

$$I = I_0 \cdot e^{-2(\frac{r}{\omega_0})^2} \tag{3}$$

where r is the radial distance from the optical axis and maximum intensity I_0 at the focus can be calculated by:

$$I_0 = \frac{2 \cdot E_p}{\pi \cdot \omega_0^2 \cdot \tau} \tag{4}$$

where, E_p is the laser pulse energy and τ is the laser pulse duration (FWHM, full width at half maximum). Non-linear absorption takes places at the laser focus due to its highly irradiance (65,70). The threshold intensity for optical breakdown I_{th}, which is defined as the laser intensity required to reach the critical free-electron density of $\rho_{cr} = 10^{21}$ cm^{-3} (65). I_{th} has been measured to be 3×10^{12} W/cm^2 in aqueous solutions for near infrared femtosecond

laser pulses. A few nanoseconds after the high energy density plasma generation, pressure waves with high initial pressures of a few GPa are generated at the focus, expanding radially with velocity of a 1.5-2.5 km/s (72). After that, an expanding cavitation bubble of a few micrometers in diameter is generated in the liquid.

The mechanism of film-free femtosecond laser-induced printing bases on a rapid expanding cavitation bubble near to the liquid surface (60,70). The liquid jet and cavitation bubble behavior have been described by a standoff parameter γ (74,75):

$$\gamma = \frac{Z}{R_{max}} \tag{5}$$

which describes the ratio of the distance of the bubble centroid from the free surface Z (here laser focus depth) and the maximum radius of the cavitation bubble in the liquid R_{max} (see Figure 2.1). It was experimentally and numerically demonstrated, that a narrower and faster jet can be generated by decreasing the standoff parameter γ (75).
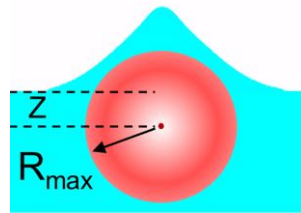

Figure 2.1 Schematic of cavitation bubble near to free surface.

The laser beam is mainly transmitted when the laser intensity is below the optical breakdown threshold. Above the threshold also reflection and scattering come into play (76). Only the absorbed energy can be converted into energy for plasma generation, thermal energy for evaporation and mechanical energies for the cavitation bubble expansion and the mechanical bubble energy can be calculated by (63,76):

$$E_B = \frac{4\pi}{3}(p_0 - p_v)R_{max}^3 \tag{6}$$

where the hydrostatic pressure p_0 and vapor pressure p_v are determined to be 0.1 MPa and 2.33 kPa at 20°C, respectively (76,77).

As the cavitation bubble rapidly expanded, the liquid near to the surface can be much easily displaced due to lower pressure and resistance on the surface (60,70,71). This

asymmetrical expansion leads to a pressure gradient between the surface and bubble side, which results in liquid flows around the bubble wall (Figure 2.2a). Flows converge at the top of bubble and lead to a high-pressure stagnation point, where opposing jets can be generated: an outward spike jet (i.e. the first jet) and an inward jet in Figure 2.2b. When the inward jet has sufficient energy, it can then penetrate the bottom wall of the collapsing bubble resulting in a new toroidal bubble (Figure 2.2c). This new toroidal bubble reaches a high-pressure due to compression after the bubble collapses. Similar to the original spherical bubble expansion the toroidal bubble expands again and propels a much thicker jet (i.e. the second jet in Figure 2.2c) with a lower speed.
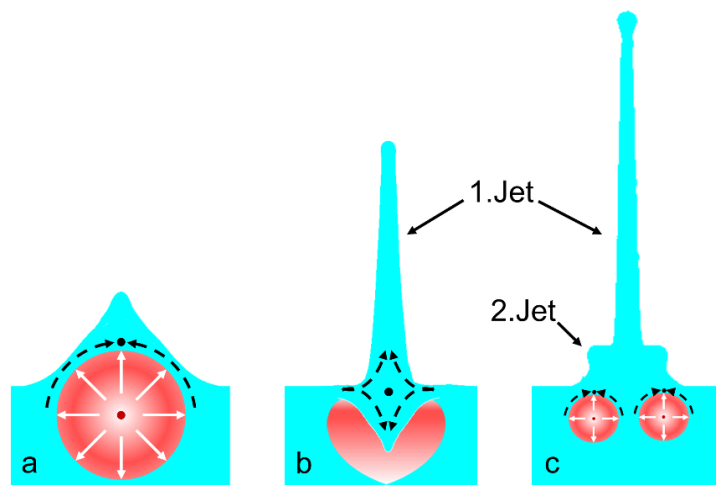

Figure 2.2 Mechanism of the film-free femtosecond laser-induced printing process. (a) Rapid expansion of a cavitation bubble in the liquid and creation of liquid flow around the bubble. (b) Convergence of flows and generation of two opposing jets: outward spike jet (i.e. the first jet) and inward jet. (c) Formation of a new toroidal bubble by penetration of the inward jet, resulting in a much thicker jet (the second jet) with a lower speed.

2.2 Spherical aberration

It is known that light can be refracted, when passing through an interface between two different transparent media. Figure 2.3 shows the laser focus in liquid indicated by red point due to the refraction of laser beam at hydrogel surface. The laser focus in air is indicated by the gray point. The laser focus length in liquid Z, which will be referred to laser focus depth in rest of this work, can be calculated by Snell's law:

$$Z = nZ_0 \qquad\qquad (7)$$

where n is the refractive index of liquid and Z_0 the laser focus length in air. The laser focus depth can be controlled in our experiments through vertical displacement of the objective.
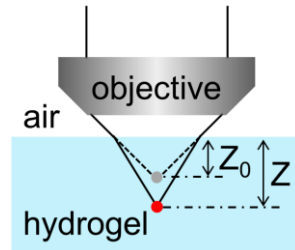

Figure 2.3 Schematic of laser focus through microscope objective in liquid

For focusing the fs laser beam, in this work, three different microscope objectives were applied, whose specification can be found in Table 2.1. For the upright transfer optical configuration, the collimated NIR fs-pulse was focused through a transparent acceptor into the hydrogel, using a 32× microscope objective (Leica Wetzlar, Germany) with a numerical aperture of 0.6, a transmittance of 65% at 1030 nm wavelength, and a working distance of 6 mm (Figure 2.4a). For the inverted configuration, two objectives were used for focusing the fs-laser beam through the reservoir bottom (Figure 2.4b and c): a 40× dry objective (Nikon40×/0.6 CFI S Plan Fluor) with a numerical aperture of 0.6 and a 25× water immersion microscope objective (Leica HC FLUOTAR L 25×/0.95 W VISIR) with a numerical aperture of 0.95. For printing of living cells the acceptor is usually coated with a hydrogel to cushion the impact of landing cells, and to maintain a humidified environment to protect the transferred cells from drying out. Cells and hydrogel can be transferred from the reservoir to an acceptor slide, resting above the hydrogel reservoir at a distance of about 1 mm.
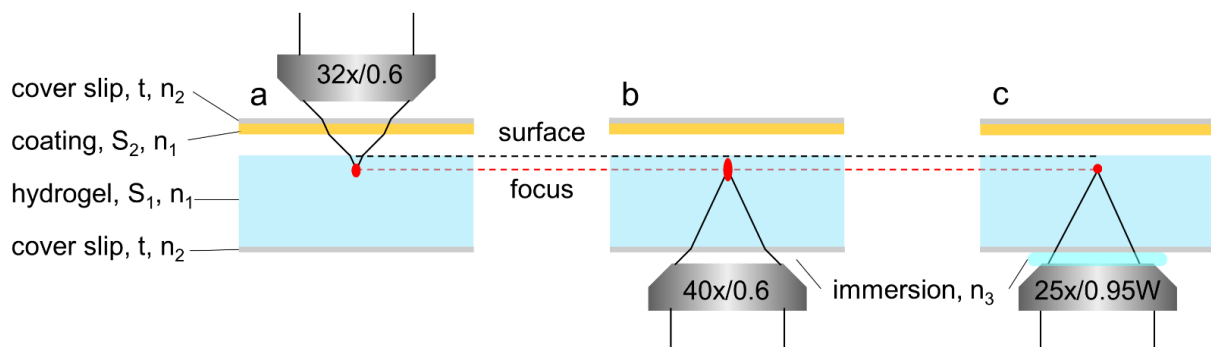

Figure 2.4 Setups of fs laser-based printing through three different microscope objectives.

Table 2.1 Specifications of the applied three microscope objectives

Objective	Magnification	NA	Working distance	Immersion	Cover slip correction	Transmission at 1030 nm
Leica L32x0.6	32x	0.6	6 mm	Air	0 mm	65%
Leica25x/0.95W HC FLUOTAR L	25x	0.95	2.5 mm	Water	0.17 mm	80%
Nikon40x/0.6 CFI S Plan Fluor	40x	0.6	3.6-2.8 mm	Air	0-2 mm	40%

The difference of refractive indices between laser focus and microscope objective can lead to a spherical aberration of microscope objective (78). The collimated laser beam can be ideally focused through the objective at same point O which results in an optimal focus (indicated by dashed red lines in Figure 2.5a) without difference of refractive indices. However, when we use the upright optical configuration, the laser beam is focused in the hydrogel through 3 transparent materials with different refractive indices ($n_2 > n_1$ and n_3) as shown in Figure 2.5a. The light passing near to the optical axial is slightly refracted, resulting in a shorter focus length (O_1). However, a longer focus (O_3) is resulting when the light passes through the periphery of the microscope objective with larger angle of incidence. This phenomenon with more focal points in the optical axis is known as longitudinal spherical aberration (LA), which represents the distance between O_1 and O_3 and can be calculated (78)

$$LA = S_0 \sqrt{\frac{n_3{}^2 - NA^2}{n_1{}^2 - NA^2}} + t \sqrt{\frac{n_3{}^2 - NA^2}{n_2{}^2 - NA^2}} - (\frac{n_3}{n_1}S_0 + \frac{n_3}{n_2}t) \qquad (8)$$

where S_0 is the laser propagation length in hydrogel, t the thickness of acceptor slide, NA the numerical aperture of the applied objective which provides the maximal angle of incidence, and n_1, n_2 and n_3 are the refractive indices of the hydrogel in the reservoir, acceptor slide and the used immersion medium.

For the upright configuration through the Leica 32× objective, air is used as the immersion medium with $n_3 = 1$. The fs laser beam path goes through the acceptor slide (here a cover slip with $n_3 = 1.53$) with a thickness of $t = 170$ µm and then focuses into the hydrogel. For the inverted configuration, a Nikon 40× can focus laser beam goes through the reservoir bottom with a refractive index $n_2 = 1.52$ and about 50 µm underneath the free surface of the hydrogel (Figure 2.4b). Water ($n_3 = 1.3$) was used as the immersion medium for the Leica 25× water immersion objective as shown in Figure 2.4c. In this case, we assume that the hydrogel refractive index is similar to the refractive index of water (i.e. $n_1 \approx n_3 = 1.3$). The thickness of reservoir bottom between the immersion medium and the hydrogel can

14

be corrected by a specialized correction collar from the Nikon 40× and Leica 25× objective, leading to $t = 0$ µm for inverted configuration. The plot of $|LA|$ through 3 different objectives in a function of the laser propagation length in the hydrogel S_0 can be found in Figure 2.5b. LA increases linearly with the laser propagation length S_0 by using the Leica 32× objective for upright configuration and Nikon 40× objective for inverted configuration. However, a best focus with almost no spherical aberration ($LA \approx 0$) can be generated by Leica 25× regardless of the laser propagation length in the hydrogel S_0, which is only limited by working distance of objective.
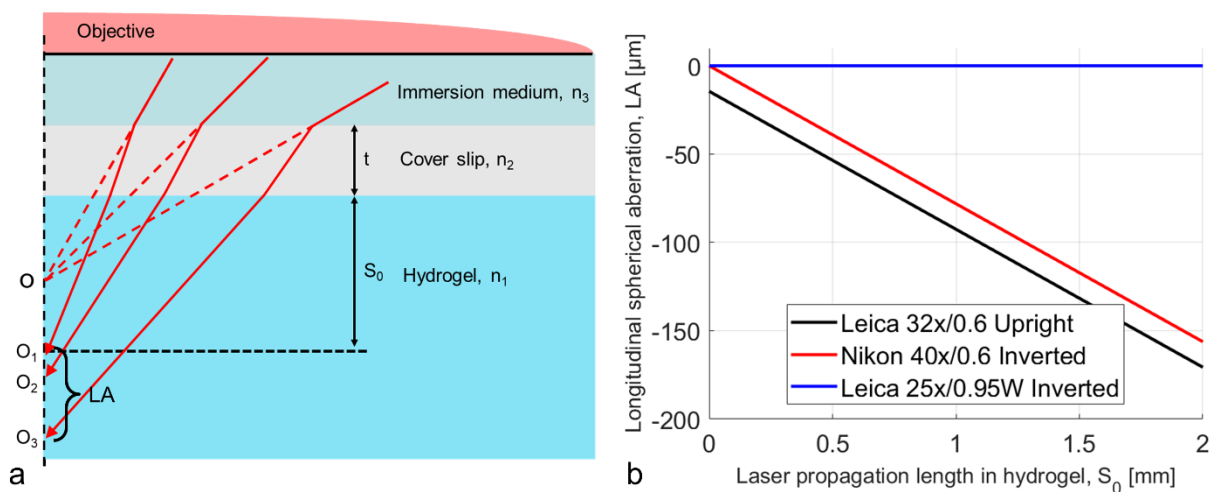

Figure 2.5 (a) Schematic of spherical aberration through 3 transparent media. The distance between O_1 and O_3 is the longitudinal spherical aberration LA because of the difference of refractive indices between laser focus and microscope objective. (b) Plot of the calculated LA by varying the laser focus length in hydrogel S_0 through 3 different objectives.

2.3 Hydrodynamic analysis of jet propagation

In order to analyze the jet dynamics, we apply the most important dimensionless numbers from literature (44,71,79–81). The first is the Weber number, which is often useful in analyzing the mechanics of the fluid jet and describes the ratio of kinetic energy of the propagating jet relative to surface energy:

$$W_e = \rho v^2 d/\sigma \tag{9}$$

where ρ is the hydrogel density (histopaque 1.083 g/ml), v is the jet velocity, d is the jet width, σ is the surface tension of hydrogel at room temperature (here is 72.75 mN/m for water).

The Reynolds number describes the relationship of inertial forces to viscous forces indicated by the internal movements within the fluid:

$$R_e = \rho v d / \mu \tag{10}$$

where μ is the dynamic viscosity of the hydrogel (measured to be 13 mPa·s for pure histopaque). The Reynolds number is usually applied to describe the fluid flow situations. At low Reynolds number, flows develop in laminar form. As the Reynolds number increases, the fluid flow trend to be turbulent.

The ratio of hydrogel viscosity is usually characterized by the Ohnesorge number:

$$O_h = \frac{\sqrt{W_e}}{R_e} = \mu / \sqrt{\sigma d \rho} \tag{11}$$

At low Weber number $W_e < 4$, the kinetic energy for jet propagation is insufficient to overcome the surface tension of the air–hydrogel interface and the jet collapses without leaving the hydrogel reservoir, leading to no material transfer in Figure 2.6. Above the Weber number $W_e > 4$, a continuous hydrogel jet can be formed (80,82). However, this jet is not able to develop infinitely, but breaks up into single or even multiple droplets, this phenomenon can be explained by the Rayleigh-Plateau instability (83). The breakup mechanisms can be classified into four different regimes by increasing the jet velocity as well as Weber and Reynolds numbers: Rayleigh breakup, first wind-induced as well as second wind-induced breakup and finally atomization (see Figure 2.6) (84,85). For Rayleigh breakup, the jet velocity is just sufficient to cause a pinch-off due to capillary forces (79,82,84,85). In the first wind-induced breakup regime, the breakup take place later and the corresponding breakup length increases with the increasing jet velocity (86). In this case, the aerodynamic force caused by the relative motion between the liquid jet and gas can be ignored. A primary droplet is pinched off from the first jet and its diameter is proportional to the jet width (79). However, the aerodynamic force cannot be ignored in the second wind-induced breakup and the atomization regimes. In this case, lots of smaller droplets can be observed and therefore are not suitable for printing.
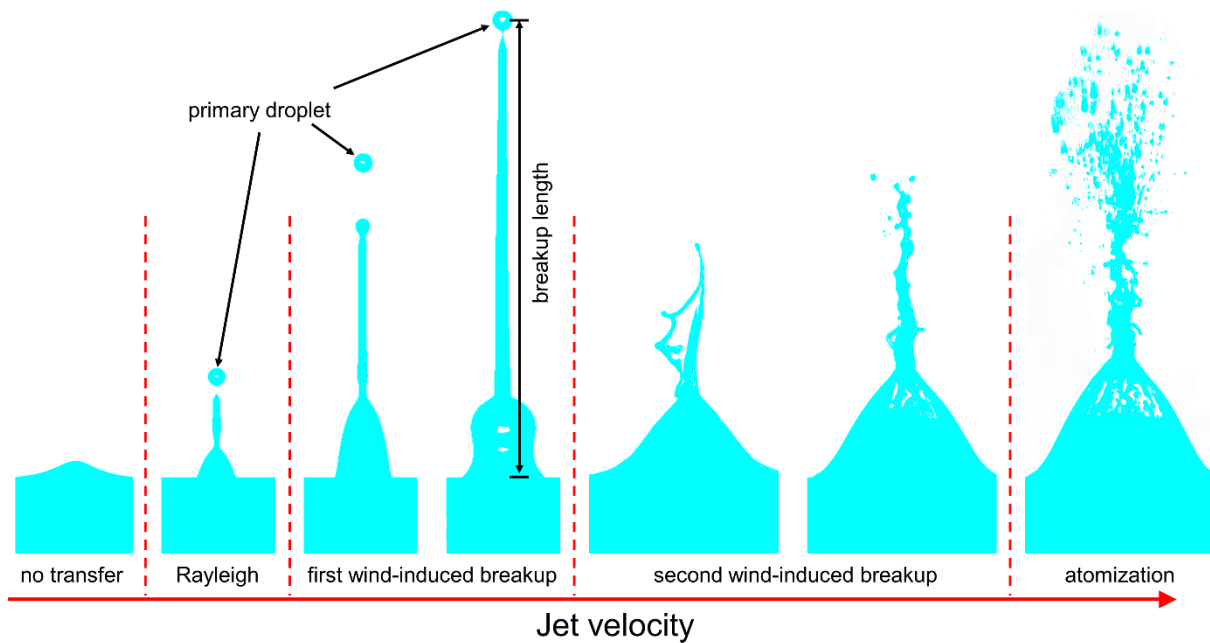
Figure 2.6 The schematic jet breakup mechanisms: Rayleigh breakup, first as well as second wind-induced breakup and atomization mechanisms by increasing the jet velocity.

2.4 Sample preparation

2.4.1 Cell culture

"Human mesenchymal stem cells (hMSC, SCP1 cell line) (87)*, murine skin melanoma cells (B16F1 cell line, ATCC, Wesel, Germany), human papillary thyroid carcinoma cells (TPC1cell line, ATCC, Wesel, Germany) and murine fibroblasts (NHI/3T3 cell line, ATCC, Wesel, Germany) were maintained in Dulbecco's Modified Eagle Medium (DMEM, Biochrom, Germany) supplemented with 10% fetal bovine serum (FBS, Biochrom, Germany), 1% GlutaMAX (Thermo Fisher Scientific, Germering, Germany) and 1% Penicillin/Streptomycin (P/S, Biochrom, Berlin, Germany). Human tendon stem/progenitor cells (hTSPCs) were previously isolated from Achilles tendon and characterized in detail by Kohler et al.*(88)*. The isolation of the cells was approved by the Ethical Commission of the LMU Medical Faculty (grant No. 166-08), and informed consent was obtained from the donors. hTSPCs were maintained in DMEM/HAMs F-12 Medium (Biochrom, Germany) supplemented with 10% FBS, 1% GlutaMAX, 1% P/S and 1% non-essential amino acids (Gibco, Germany). In routine cell culture, all cells were grown up to 80% confluency and maintained at 37°C in 5% humidified CO_2. For passaging, cells were detached with 0.25% trypsin/0.02% Ethylenediaminetetraacetic acid (EDTA) solution (Biochrom, Germany)".* The text is obtained from the article (22).

2.4.2 Preparation of the cell-containing hydrogel in a reservoir

"To transfer living cells using the inverted optical configuration, approximately 2x10^4 freshly detached cells were pelleted by centrifugation and suspended in 400 µl histopaque 1803 (Sigma-Aldrich, Deisenhofen, Germany). To detach cells, 0.25% trypsin/0.02% EDTA was used and the detachment was performed under microscopic control to ensure a complete detachment of the adherent cells, until only single cells remained in suspension. Detachment times were variable depending on the cell type. The cell-containing hydrogel was transferred to a µ-Dish (µ-Dish 35 mm low, Ibidi, Martinsried, Germany), which served as reservoir for cell transfer. Due to their lower mass-density, the cells concentrate at the surface of the histopaque 1803. For jet visualization with shadowgraphy, a rectangular, transparent dish (DIC Lid, Ibidi, Martinsried, Germany) was used as reservoir, which was filled with cell-laden hydrogel (1x10^4 cells/ml in histopaque 1083). For fluorescence-based jet visualization, 5 ml histopaque 1083 were mixed with 10 µl fluorescent dye (Alexa) 532-I amine-reactive Succinimidyl Ester (Abnova, Germany, 10 mM dissolved in DMSO, maximum excitation/emission wavelength of 542/558 nm), yielding a final concentration of 0.02 mM. For cell staining, 10^5 B1F1 cells were obtained by centrifugation. The cell pellet was suspended in 10 µl of the same fluorescent dye and incubated under gentle agitation for 2h at 37°C. The stained cells were added to the stained hydrogel within the reservoir". The text is obtained from the article (22).

2.4.3 High viscous hydrogel preparation and viscosity measurement

"For printing of high viscous hydrogel, histopaque 1083 was supplemented with alginic acid sodium salt from brown algae (Sigma-Aldrich) in concentrations up to 1.5%. The viscosity measurement of alginate hydrogels was carried out at room temperature (21°C) using the rotational viscometer RC01/02 (Rheotec, Dresden, Germany) at a rotational speed of 200 rpm. For the measurement of 1.5 % alginate hydrogel samples, the viscometer was equipped with the L4 standard spindle, while for the 1% alginate hydrogel the spindle was changed to the L3 standard spindle, and both, the 0.5 % hydrogel and the pure histopaque 1083 as control, were measured using the L2 standard spindle". The text is obtained from the article (22).

2.4.4 Preparation of the acceptor surface

"For jet visualization according to the pump probe principle, a standard coverslip with a thickness of 170 µm was used as acceptor slide. To print living cells, a hydrogel coated coverslip or a Petri dish (TC Dish 60, Standard Sarstedt, Germany) served as an acceptor surface

to protect the transferred cells from drying out. The respective hydrogel depended on the printed cell type: When printing TPC1 cells, gelatin (Sigma-Aldrich, Germany) was used for coating. The gelatin was dissolved in phosphate buffered saline (PBS) (10% w/v) at ~50°C, homogenously dispersed on the acceptor surface and then cooled to 4°C for 15 min, to form a film of ~100 µm thickness. The acceptor surface for hTSPCs was coated with 0.5% collagen (Collagen G1, MATRIX BioScience, Germany): The collagen stock solution was gently mixed with neutralizing buffer (1 ml of 0.7 M sodium hydroxide solution, 1 ml of 1 M 4-(2-hydroxyethyl)-1-piperazineethanesulfonic acid (HEPES) buffer and 2 ml 10x DMEM, pH adjusted to 7.9 - 8.05) at a ratio of 4:1. 5 ml of this mixture were homogenously dispersed on the bottom of the petri dish and then incubated over night at 37°C. To print B16F1 cells, Matrigel (BD Biosciences, Heidelberg, Germany) was used as an acceptor coating: Matrigel was thawed at 4°C overnight, 100 µl were evenly dispersed in the pre-cooled Petri dish and then incubated at 37°C for 10 min to obtain a ~100 µm hydrogel layer". The text is obtained from the article (22).

2.4.5 Cell viability analysis

"To detect dead cells, the hydrogel on the acceptor slide was supplemented with 2 droplets of Propidium Iodide (PI) ReadyProbes reagent (PI R37108, Thermo Fischer, Germering, Germany), per ml hydrogel solution. Intact cells reject PI, in dead cells PI binds to DNA and causes a red fluorescence. After cell transfer, the acceptor surface was incubated at 37°C for 15 min for PI staining. Dead cells were determined by fluorescence microscopy using an inverted optical microscope (Nikon Ti-E). The viability of non-transferred cells remaining in the reservoir was also investigated by PI staining: live and dead cells were counted using a standard hemocytometer chamber (Brand, Wertheim, Germany) in the fluorescence microscope. For hTSPC and TPC1 cells, (additional) PI staining of all cells in the cell reservoir prior to the laser transfer served as negative control and ensured that only viable cells were transferred in the cell viability experiments. For B16F1 cells, the numbers of live and dead cells after the transfer were determined in the inverted fluorescence microscope, as described above. The effective cell survival rate was then determined by dividing the percentage of viable cells after transfer to the percentage of viable cells without laser transfer, which was determined in an independent negative control experiment using PI staining of non-transferred cells. To ensure the effectiveness of PI staining, cells were deliberately killed during transfer,

and then stained with PI in a positive control experiment (see Figure 3.33 for PI staining of transferred cells, as well as negative and positive control experiments)".

"To determine the cell survival rate via time lapse microscopy, the hydrogel coated acceptor slide containing the transferred cells was placed in an incubation chamber, providing 37°C and 5% humidified CO_2 environment (Pecon, Erbach, Germany). This chamber was mounted on an inverted optical microscope (Observer Z.1, Carl Zeiss, Göttingen, Germany) and a first image was recorded. After 15 min, 3 ml of DMEM cell culture medium for B16F1 cells and DMEM/HAMs F-12 Medium for hTSPCs were gently added. From now on, microscopy images were collected in 20 min intervals for about 40 hours. The images were taken using an Orca Flash 4.0 scientific CMOS camera (Hamamatsu, Herrsching, Germany). In time lapse images, activity such as active cell spreading, polarization, migration and proliferation was used as indicator of cell viability". The text is obtained from the article (22).

2.4.6 Cell staining

"For phalloidin and DAPI staining, the cells on the acceptor surface were washed with PBS containing Ca^{2+}/Mg^{2+} (Biochrom, Germany), fixed with 3.7% formaldehyde (Carl Roth, Germany) for 15 min and washed 3 times with PBS. Cells were incubated with 0.5% Triton-X 100 (Sigma Aldrich) in PBS for permeabilization for 10 minutes. The cells were submersed in the staining solution containing Atto594-Phalloidin (Atto-Tec GmbH, Germany) in a final concentration of 200 ng/ml and DAPI (AppliChem GmbH, Germany) in a final concentration of 10 ng/ml in PBS, incubated for 20 min, washed 3 times with PBS and mounted with ProLong Diamond Antifade Mountant (ThermoFisher Scientific, Germany). To visualize F-actin in living cells, NIH/3t3 fibroblasts were transfected with the plasmid (pCMV-LifeAct-TagRFP, Ibidi, Germany) using the Torpedo^{DNA} transfection reagent (Ibidi, Germany). Sorting of the LifeAct expressing cells from non-expressing cells was done 48 h after transfection. For orange labeling of TPC1 cells, the Cell Explorer^{TM} Live Cell Tracking Kit Orange (AAT Bioquest, Sunnyvale, USA) was used according to the manufacturer's instructions". The text is obtained from the article (22).

2.4.7 DNA damage analysis

The radiation and thermal effect arising from the laser pulse created optical breakdown used for the printing process or the mechanical stresses arising from the expanding cavitation bubble may lead to DNA damage. DNA double strand breaks of printed

SCP1 cells were detected using the STA-321 DNA DSB staining kit from Biolabs, which is based on the phosphorylation of the histone HA2.X at serine 139. The DSB staining protocol was carried out according to the manufacturer's instructions. For comparison, an immunofluorescence staining of non-transferred SCP1 cells was performed as a negative control. As a positive control, non-transferred SCP1 cells were treated with 100 µM etoposide (DNA DSB Inducer) for 1 hour to induce DNA double strand breaks and then stained as described before.

2.4.8 Preparation of the Pluronic F-127 for printing of 3D structures

"Dissolved Pluronic F-127 hydrogel is well suited for 3D printing as its thermo-responsive properties and fast gelation time, which can be adjusted by temperature and concentration (89). For 3D printing with our setup, Pluronic F-127 (Sigma Aldrich, Taufkirchen, Germany) was dissolved in PBS to a final concentration of 15 wt% and stored at 4°C overnight. At this temperature, the hydrogel stays liquid in the reservoir. Upon transfer to the acceptor slide, the pluronic hydrogel undergoes a fast gelation as the transferred spots reach room temperature very quickly as shown in Figure 3.43". The text is obtained from the article (22).

2.4.9 Preparation of protein-based 3D micro scaffolds

"3D micro scaffolds with a length of 80 µm, a width of 40 µm and a height of 100 µm were printed by someone else with Bovine Serum Albumin (BSA)-based resin and rose bengal as photo-initiator using a two-photon absorption stereolithography system Nanoscribe GT (Nanoscribe, Karlsruhe, Germany). BSA resin preparation and high-resolution 3D printing were conducted as described elsewhere (90). In brief: 40 wt% BSA stock solution was mixed with 85mM rose bengal stock solution in the ratio 9:1. A droplet of this suspension was placed on a 170 µm thick glass slide. The 3D scaffolds were then printed using the dip-in mode. After completing the printing process, subsequent resin was washed away and scaffolds were stored in PBS at 4°C until further usage". The text is obtained from the article (22).

2.5 Statistical methods

"Single cell positioning accuracy was defined and determined as the root mean square deviation (RMSD) of the cell positions from an arbitrary chosen the target position. E.g. the target position may be determined in an independent experiment with cell-free spots as the mean position of a number of transferred spots:

$$RMSD = \sqrt{\frac{1}{n}\sum_{i=1}^{n}[(x_i - x_0)^2 + (y_i - y_0)^2]} \qquad (12)$$

where (x_i, y_i) are the individual cell positions, and (x_0, y_{i0}) designate the target position.

Single cell positioning precision was determined as the root mean square deviation (SD) from mean cell position:

$$SD = \sqrt{\frac{1}{n}\sum_{i=1}^{n}[(x_i - \bar{x})^2 + (y_i - \bar{y})^2]} \qquad (13)$$

where (x_i, y_i) are individual cell positions, and $(\bar{x}, \bar{y})$ designate the mean cell position". The text is obtained from the article (22).

In this thesis, Microsoft Excel and Origin software have been used for collecting and calculating the experimental data. The experimental reproducibility is given for each result in the figure and table legends. Due to the experimental nature of this work, no direct comparison between study groups and statistical tests were carried out.

To determine the cell survival rate after transfer, 165 single hTSPCs transfers from 15 independent experiments were carried out (see Table 3.10), which were transferred to a collagen-coated substrate. For B16F1 cells, which were transferred to a Matrigel-coated substrate, the survival rate was determined by 134 cells from 13 independent experiments (Table 3.11). For TPC1 transferred to a gelatin-coated substrate, the survival rate was calculated with 64 cells from 6 independent experiments (Table 3.12).

To analysis the transfer process, the time-resolved images of the cavitation bubble in the hydrogel and the transferred hydrogel jet at each delay time were repeated at least three times. The results were presented as mean ± standard deviation of 3 independent experiments per laser parameter. To determine the obtained hydrogel spot diameter and the single cell positioning accuracy and precision on the acceptor slide, the mean ± standard deviation of 30-100 independent hydrogel spots were calculated. The data in Figure 3.22c

displays the cell deviation frequencies, which is obtained by dividing the number of transferred cells within the deviations from the target position to the total transferred cells.

3 Results

3.1 Upright configuration for fs laser-based cell transfer

Key aspect of this thesis was the establishment of an ultra-fast laser-based technique for the transfer of living mammalian cell with single cell precision. For this purpose, an upright fs laser set up was planned, designed and built *de novo*. In a series of experiments, transfer parameters and suited hydrogels were identified and continuously optimized and adapted to various cell types. The integration of a time-resolved imaging system allowed for the observation of the transfer process.

3.1.1 Setup description

In the upright configuration the fs laser pulse (λ = 1030 nm, 600 fs) is focused from above through the acceptor and the reservoir surface directly underneath a thin cell layer, which is suspended on the hydrogel surface in reservoir (Figure 3.1 left) (22,73). An identical configuration was used by Serra et al., who established this method for generating hydrogel jets without transferring cells (34,60,70). To analyze and optimize the jet dynamics, an optical setup was established for a shadowgraphy visualization of the transfer process from a side view, at defined delay times and with a nanosecond temporal resolution. This technique is commonly known as Pump-Probe Microscopy (PPM), and has been used in a variety of applications, such as investigation of laser-induced ablation of metals (91–93). The pulse duration for illumination is much shorter than the camera exposure time, therefore a time-resolved image series can be integrated by delaying the illumination of the probe pulse.

"As shown in Figure 3.1 right, a fs-laser pulse was isolated from a 500 Hz pulse train of the laser source with a mechanical shutter (Uniblitz, Rochester) and focused by a 32× microscope objective (Leica Wetzlar, Germany). For shadowgraphy, the transfer process including the pressure wave, cavitation bubble in the hydrogel and the transferred hydrogel jet were probed perpendicular to the transfer direction in transmission, using a pulsed 28 ns spark flash-lamp (Nanolite KL-L, High-Speed Photo-Systeme, Wedel, Germany). For fluorescence excitation and probing, a collimated frequency doubled q-switched laser pulse (523 nm wavelength, 5 ns pulse duration, 40 µJ pulse energy, Mosquitoo, InnoLas Photonics, Germany) was used. The probe-pulse imaging system comprised of a microscope objective with long working distance (M Plan Apo 5×/0.14 and 10×/0.28, Mitutoyo, Japan) perpendicular to

the 523 nm excitation ns laser beam, an emission bandpass filter (555/20 ET Bandpass, Chroma, Bellows Falls, VT), a tube lens (TTL200-A, Thorlabs, Bergkirchen, Germany) and a 1.4 MP, 14-bit monochrome CCD camera (CCD1 in Figure 3.1) with a full well capacity of 16,000 electrons and 6 electrons RMS read out noise (PCO, Pixefly USB, Kelheim, Germany). Synchronization was accomplished by a photodiode (DET10A/M, Thorlabs) and a delay generator (DG645, Stanford Research Systems, Sunnyvale, CA). By illuminating the transparent reservoir from below with a halogen lamp, a bright field image of the cell distribution at the hydrogel surface was obtained with the confocal camera CCD2 (DMK 41BU02.H, Imaging Source, Bremen, Germany, see also Figure 3.1). By moving the reservoir in x-y-direction the desired cells were positioned in the fs-laser focus and thereby selected for transfer. A separate x-y-z stage allowed for precise positioning of the acceptor slide, which caught and carried the transferred cell-laden spots. The distance between the hydrogel/cell surface and the acceptor slide was about 1 mm. The focus depth of the fs-laser pulse in the reservoir was controlled by a motorized objective on a z-stage (see Figure 3.1) (LS-65, Physik Instrumente, Karlsruhe, Germany)". The text is obtained from the article (22).
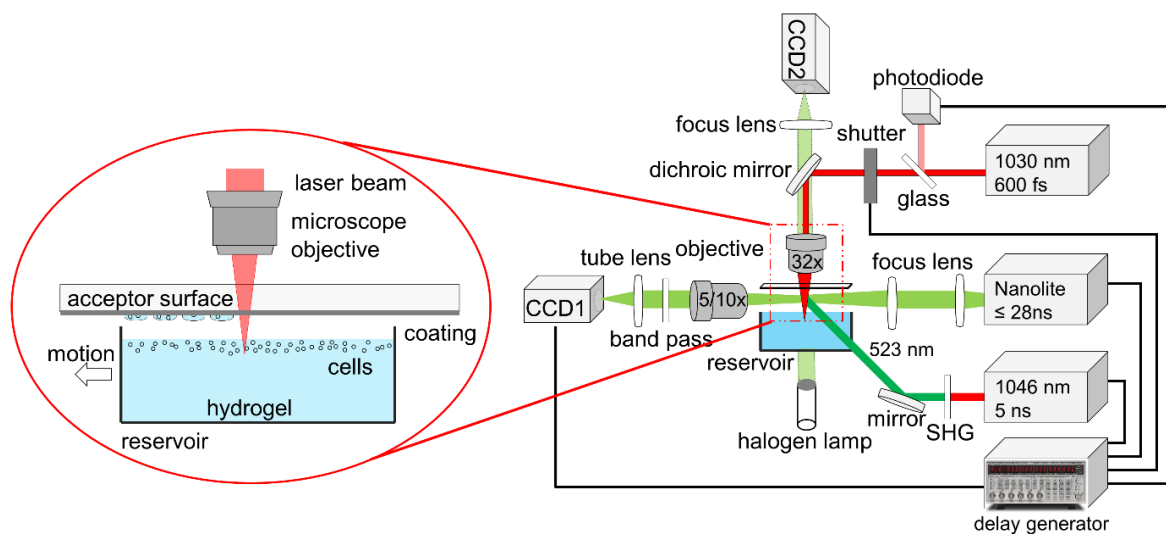

Figure 3.1 Upright setup for fs laser-based printing of mammalian cells. An fs-laser pulse is focused by a microscope objective into the reservoir containing the cell-laden hydrogel. The cell distribution at the hydrogel surface can be monitored with the confocal CCD2 camera. The transfer process is illuminated with a pulsed 28 ns white-light lamp or a 5 ns laser pulse and acquired with an imaging system comprising a CCD1 camera, a tube lens and a microscope objective (5×/10×). The delay time is triggered by photodiode and synchronized by a delay generator. The figure has been published in article (22).

3.1.2 Establishing multiple cell printing

First, to test the feasibility of printing living mammalian cells, the hydrogel consisted of 0.2% alginate in histopaque and was laden with a concentration of 5×10^6/ml GFP labelled human mesenchymal stem cells (hMSCs) of the SCP1 cell line. "*The laser pulse energy after the microscope objective was set to 5.0 µJ, the focus depth remained at 78 µm. The distance between liquid and acceptor dish was set to 500 µm. The single laser pulses to generate the jets were triggered at arbitrary x-y-position in the reservoir. Figure 3.2 shows bright field (a) and fluorescence (b) images of hydrogel micro-spots containing SCP1 cells, after laser-induced cell transfer to a gelatin coated acceptor petri dish. The large hydrogel spots are circular with an average diameter of about 200 µm, containing between 15 and 25 cells each, while the smaller hydrogel spots have a more irregular appearance, and an average diameter of 80 µm, containing only between 3 and 7 cells each. In the fluorescence image, live cells appear in green, while dead cells display in red, because of the PI staining (cf. materials and methods section 2.4.5 for details). In the large hydrogel spots, the cell survival rate is about 91%, while in the small irregular hydrogel spots the survival rate is only about 50%, calculated from 5 independent experiments (Table 3.1). For comparison, the survival rate of cells remaining in reservoir is about 92% (data not shown)".* The text is obtained from the article (73).
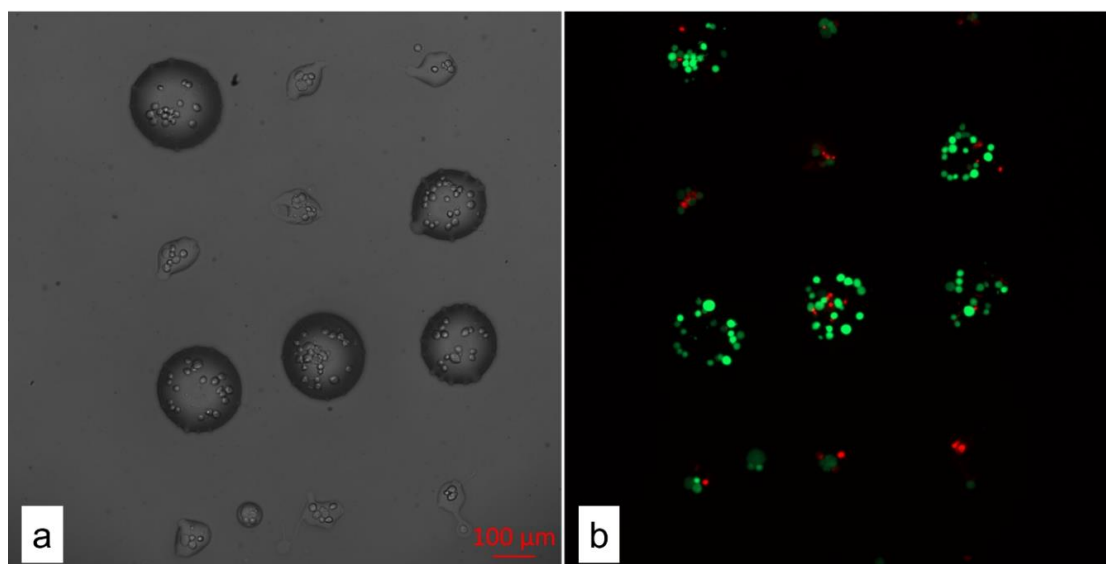

Figure 3.2 Representative microscope images of cell-laden hydrogel spots. (a) In the bright field image, the large hydrogel spots show a diameter of about 200 µm, while the small hydrogel spots size up to a diameter of only 80 µm. (b) The fluorescence image reveals a cell survival of up to 90% in the larger hydrogel spots (red PI staining indicates dead cells, live cells are displayed in green), in small hydrogel spots only 50% of cells survive the laser-induced transfer. The figure has been published in article (73). The number of transferred cells is presented in Table 3.1.

Table 3.1 Cell survival rate from larger and small hydrogel spots (absolute cell numbers)

large spot	live	121	347	280	336	217
	dead	11	42	34	25	19
small spot	live	39	189	201	45	67
	dead	32	62	86	72	28

"To investigate the long-term effects of laser-induced transfer on cell viability, time-lapse microscopy of the transferred cells was conducted over 40 hours. Figure 3.3 shows mouse melanoma cells (B16F1 cell line) transferred from a hydrogel reservoir at 5.4 μJ laser pulse energy, which is above the threshold energy for the second jet. Immediately after transfer (see Figure 3.3 at 00:00 h), the petri dish, which served as acceptor surface, was transferred into the incubation chamber of the fluorescence microscope and a first image was recorded (cf. materials and methods 2.4.5 for details). To allow the melanoma cells to adhere to the acceptor substrate, the surface was coated with a 100 μm layer of Matrigel. The cells were allowed to rest on the Matrigel coated substrate for 15 minutes before cell culture medium was added. Note that unlike the bone marrow derived SCP1 cells shown in Figure 3.2, which adhere well on pure gelatin gel, a hydrolyzed form of collagen, the most abundant protein in bone and cartilage, the melanoma cells prefer Matrigel as a substrate, because it resembles the protein composition of the basal lamina (94). After one hour (see Figure 3.3 at 01:00 h), the distribution and appearance of cells still resembled the appearance immediately after the transfer with the exception of three cells which were missing and were most likely washed off the substrate when adding the cell culture medium (indicated by arrows). These were presumably dead cells, which were not able to adhere to the Matrigel substrate. With a total cell number of 20 cells, this corresponds to a survival rate of transferred cells of 85% for the hydrogel spot shown. After two hours of incubation, the cells started to migrate towards each other and form first cell clusters, and after nine hours, all cells from the transferred hydrogel spot were forming a single cluster in the center of the image. Migration towards each other and clustering is a typical phenomenon, which is frequently observed for melanoma and other cancer cells (95). At 30 hours, a significant increase in the cluster volume and cell number could be observed. At 40 hours, the size of the cluster increased again, which shows that the cells are able to proliferate after laser-induced cell transfer". The text is obtained from the article (73).
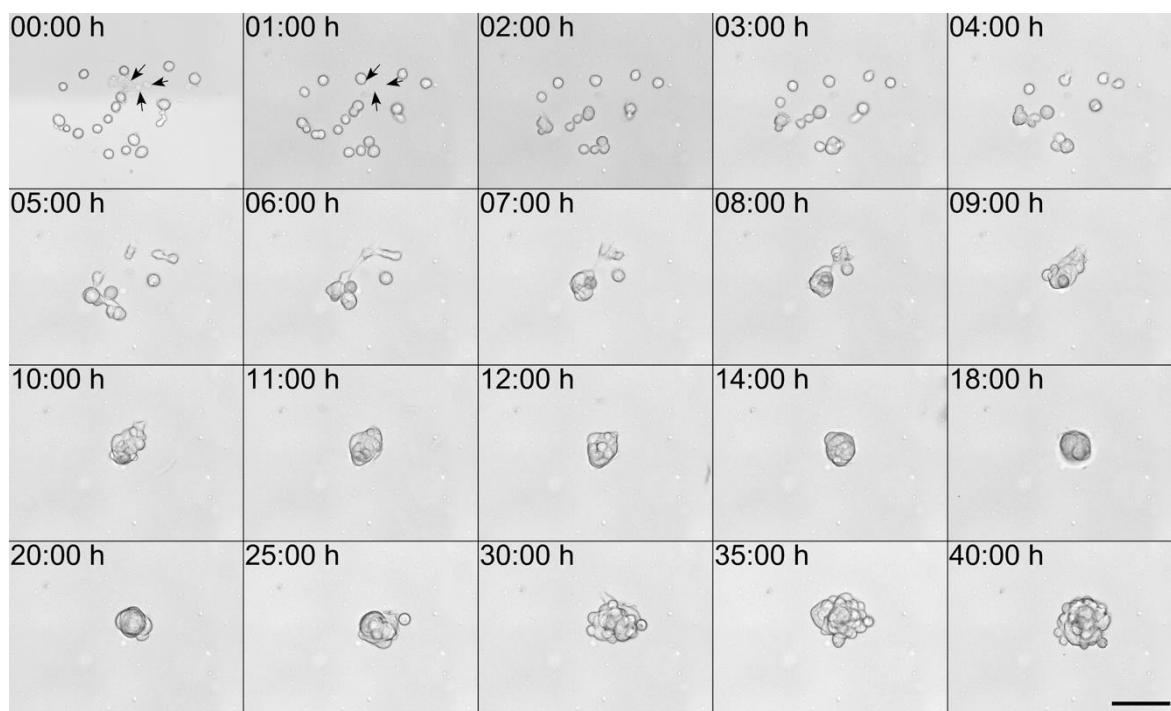
Figure 3.3 **Representative time-lapse microscopy of cell migration and proliferation from 3 independent experiments.** *Live cells are left to adhere to the Matrigel substrate for 15 min, whereas dead cells are washed away when adding 3 ml DMEM medium which was gently pipetted into the dish (arrows at 0:00 and 1:00 h). The cells were monitored for a period of 40 h. After two hours of incubation, individual cells start migration and cluster formation. After 09:00 h a common cluster comprising of all cells was formed. An increase of the number of cells and cluster volume after 30 h indicates proliferation. The scale bar corresponds to 100 µm.* The figure has been published in article (73).

In addition to cell survival and proliferation, the risk photo-induced DNA damage in the transferred cells should be avoided. Thus, we checked for DNA damage using a double strand break staining kit (STA321, Cell Biolabs Inc, USA), which is based on the phosphorylation of histone H2AX. Figure 3.4 shows phase contrast (top row) and fluorescence images (bottom row) of SCP1 human mesenchymal stem cells, after laser transfer and staining with the DSB staining kit (left column) to detect DNA double strand break, according to the protocol provided by Cell Biolabs (materials and methods 2.4.7 for details). For comparison, the immunofluorescence staining of non-transferred SCP1 cells was performed as negative control (middle column, control(-)), while a positive control of non-transferred SCP1 cells was treated with 100 µM etoposide for 1 hour to induce DNA double strand breaks (right column, control (+)). No DNA double strand breaks could be detected by fluorescence microscopy in cells after laser transfer (bottom left) as well as in the untreated negative control (bottom middle). Introduction of DSB by ectoposide in the positive control proved the functional capability of the experiment to reveal DNA damage indicated by the fluorescence signal (bottom right).

28

"A previous bioprinting study by Xiong et al., using a 193 nm UV-laser compared the survival rates and DNA damage of a cell-laden alginate bioink with and without an additional UV absorbing gelatin layer. Post-transfer cell survival rates of 77% and 68% and DNA double strand breaks in 10% and 21% of the cells, respectively, were reported (45)*. In comparison, with the 91±2% survival rate here (see Figure 3.2) and no detectable DNA double strand breaks (Figure 3.4), the film-free near-infrared fs laser printing method of this work displays significantly higher survival rates and prevents DNA damage".* The text is obtained from the article (73).
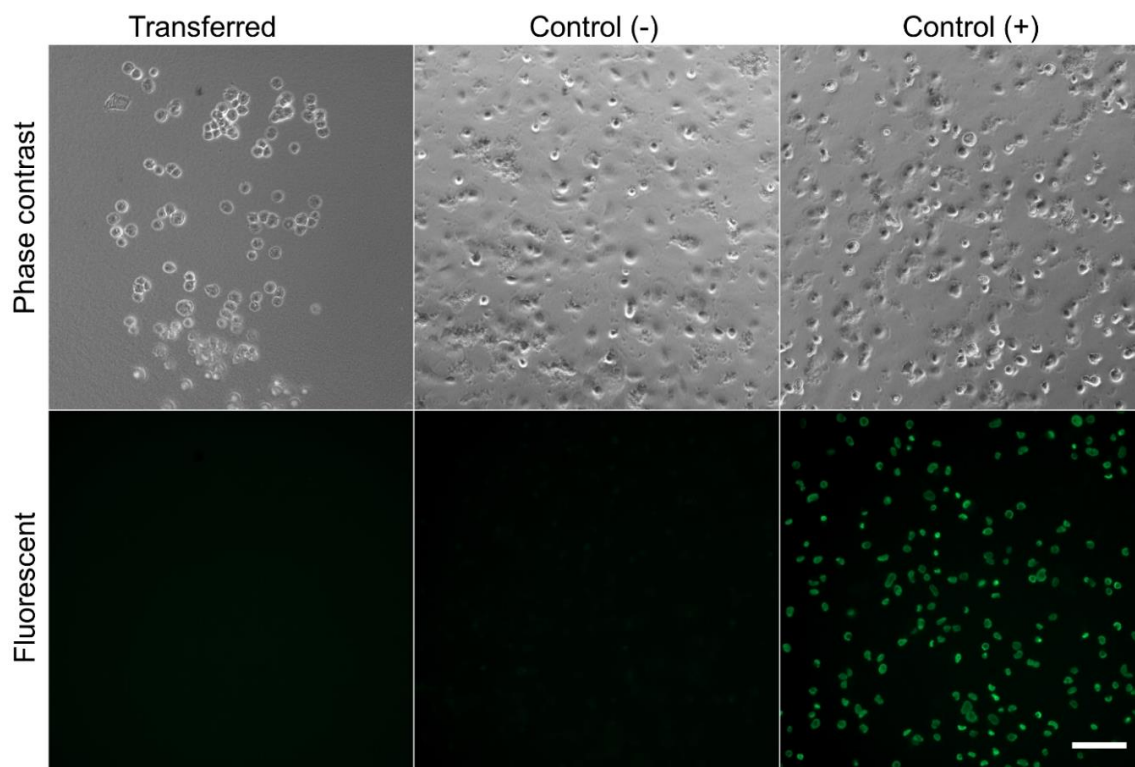
Figure 3.4 Phase contrast (top row) and fluorescence images (bottom row) of SCP1 cells with applied DSB staining kit after laser transfer (left column), non-transferred cells as a negative control (middle) and DNA damaged cells (via treatment with ectoposide) as a positive control (right column). White scale bar in right bottom image indicates a length of 100 μm. Representative figure from two experiments.

3.1.3 Establishing single cell printing

In the last section, the number of printed cells per transfer could not be controlled because the laser focus was placed arbitrarily underneath a random distribution of cells at the hydrogel surface in reservoir. The actual number of cells around the laser focus was unknown. Now a bright field observation of the reservoir and the acceptor slide was established to search, identify and select single cells and groups of cells in the reservoir and analyze transferred the cells after the transfer to the acceptor without changing the setup. *"The*

example given in Figure 3.5 shows bright field microscopy images of B16F1 mouse melanoma cells on the surface of the hydrogel (histopaque 1083) reservoir before (left images) and after transferring the cells to the target surface (middle column). After the laser pulse has arrived, the single cell (top) or the group of five cells (bottom) disappeared from the reservoir surface (middle row) and can be detected on the target surface (right column). In both cases, a 600 fs laser pulse with 3 μJ pulse energy was focused approximately 70 μm underneath the cell(s) to be transferred, as indicated by the red crosses (left images). With these parameters, hydrogel and cells within a radius of ~25 μm around the lateral position of the laser focus were transferred to the substrate. Consequently, if only one isolated cell is located within this ~25 μm radius, a single cell is transferred to the target. If several cells are located within the ~25 μm radius, all cells within this radius are transferred to the target. By choosing appropriate conditions for cell harvesting and reservoir preparation, e.g. suitable trypsinization protocols and cell concentrations, a sufficient amount of isolated cells within the cell reservoir for single cell transfer is feasible". The text is obtained from the article (22).
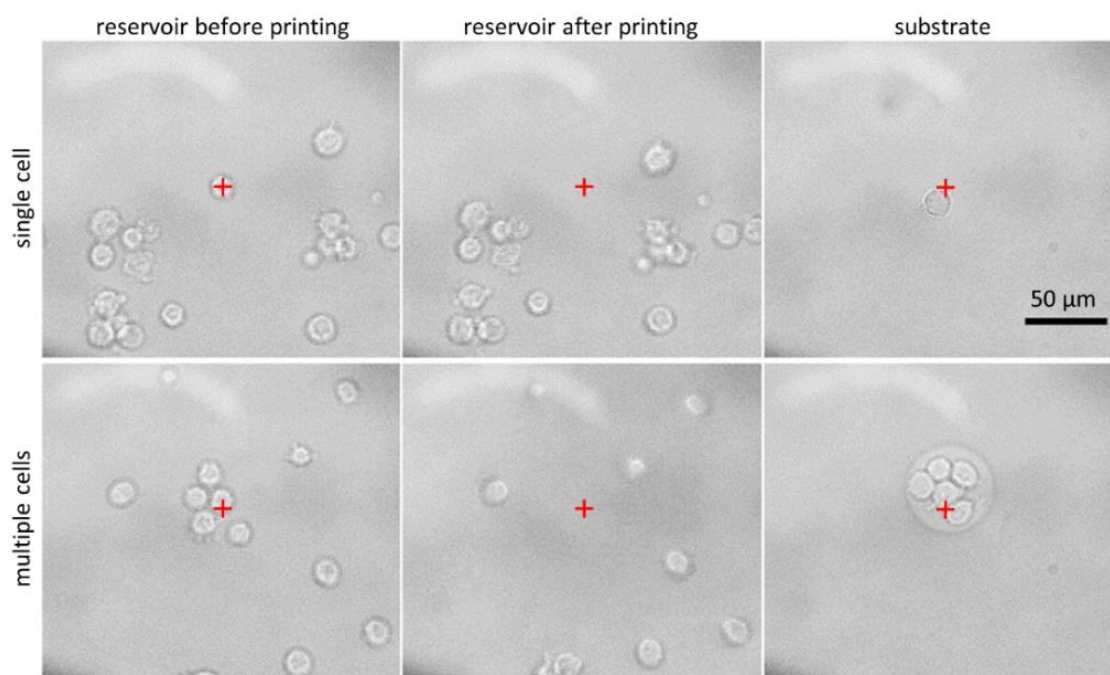

Figure 3.5 Representative microscope images of single (upper row) (at least 500 independent transfers) and multiple cells (lower row) transfer (at least 50 independent transfers), B16F1 cells are identified with an optical microscope (bright field, 32× objective, NA = 0.6), selected and transferred from a hydrogel reservoir to a target substrate. Red crosses mark the center of the bright field images which corresponds to the laser focus position in the reservoir (left column). The laser pulse energy is 3 μJ, the focus depth 70 μm. After laser triggering the selected cells disappeared from the reservoir (middle column). Pre-selected single and multiple cells were detected at the target substrate (right column). The figure has been published in article (22).

3.1.4 Investigation of transfer parameters in cell-free conditions

3.1.4.1 Overview over the cell-free jet behavior

To investigate the transfer process, and further optimize the transfer parameters, a visualization of the transfer process with a temporal resolution of nanosecond precision, as described in depicted in Figure 3.1 was carried out. Figure 3.6a presents a time-resolved image series of the cell-free jets at a pulse energy of 2 µJ and a focus depth of 52 µm. The lower part of each image shows the hydrogel reservoir surface, the top shows the acceptor slide: The distance between the hydrogel and the acceptor surface is 1 mm. At a delay time of 1 µs, a protrusion of the surface is generated, which forms a needle-like structure at the pole called, "first jet" (70,71) and which grows straight up while progressively thinning. The first jet develops with a velocity of 17.5±0.5 m/s and a small droplet, so-called, "primary droplet" (79) with a diameter of 28±2 µm (indicated by red arrows in Figure 3.6a) is formed and separates from the tip of the first jet after delay time of 30 µs and then reaches the acceptor slide at 60 µs. A much thicker jet with a width about 90 µm, so-called, "second jet (70,71)" can be found at the base of the first at a delay time of 20 µs (Figure 3.6a), which has an initial velocity of 5.2±0.1 m/s. After 70 µs, the first jet starts to breakup from the second jet at a height about 300 µm above the hydrogel surface resulting in an abrupt decrease of the second jet velocity to 1.5±0.1 m/s. A large droplet is created at 100 µs and then separates from the second jet after 220 µs and finally reaches to the acceptor slide at 500 µs. After 1 ms the propelled hydrogel has completely arrived at the acceptor and subsequently the hydrogel surface recovers to its plane surface again. The jet fronts of the first and second jet versus the delay time is plotted in Figure 3.6b and the slopes of the fits correspond to the jet velocities. It is important to note that in this study each time-resolved image was acquired from a separate experiment as a consequence from the pump-and-probe principle.
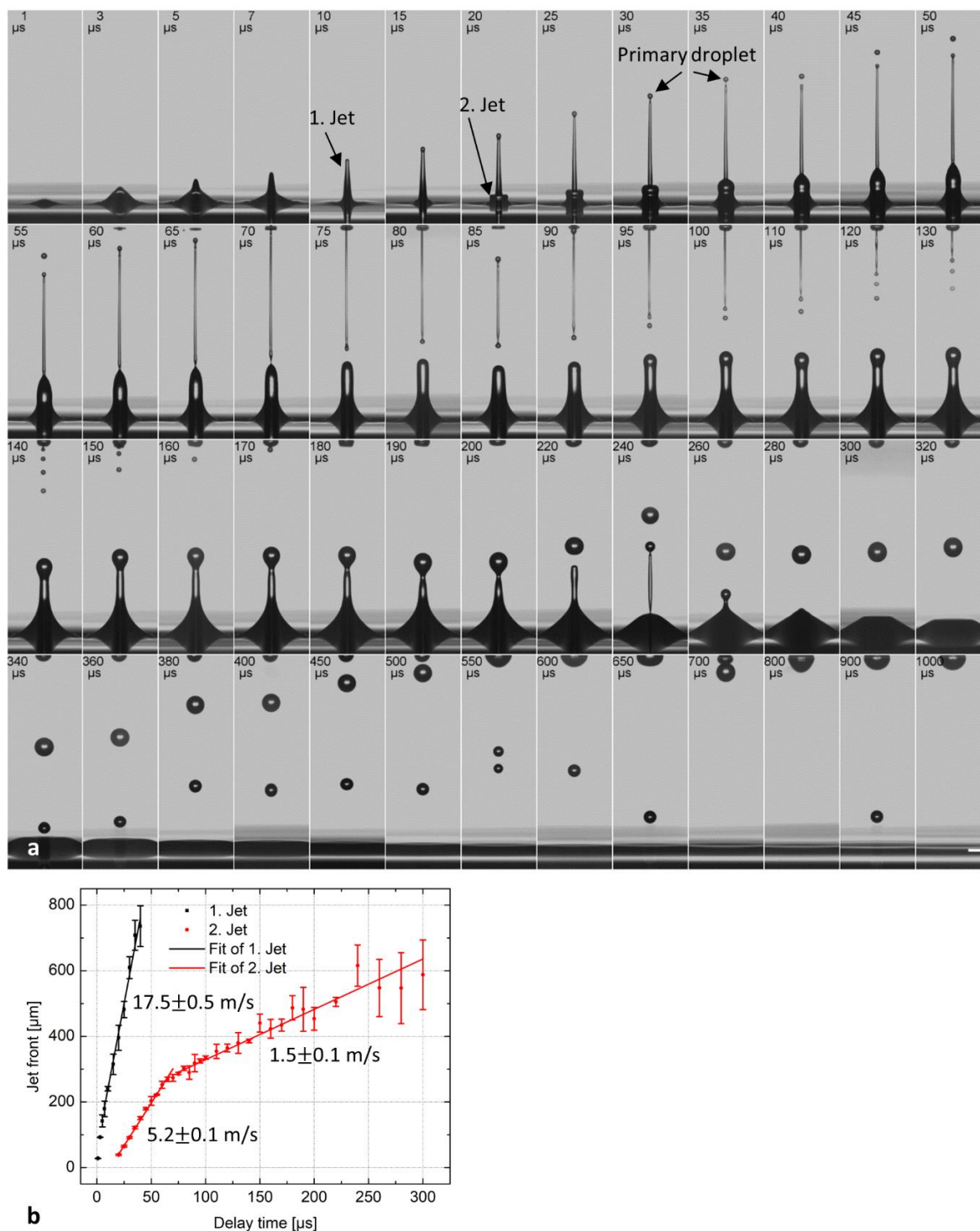
Figure 3.6 (a) Representative time-resolved images of the transfer process of pure histopaque 1083 hydrogel (3 independent jets) from 1 µs to 1 ms visualizing the time-evolution of the first and the second jet. The lower part of each image shows the hydrogel reservoir surface, the top shows the acceptor slide. The laser pulse energy is 2 µJ, the focus depth is 52 µm. Scale bar = 100 µm. (b) Jet front propagation of the first and second jet versus the delay time after the transfer laser pulse. The solid lines represent linear fits to the data, which represent average values ± standard deviations of 3 independent jets. When the first jet separates from the second, the jet velocity of the second jet drops from 5 to 1.5 m/s. The figure has been published in article (22).

3.1.4.2 Effect of laser pulse energy on cell-free jet dynamics

To investigate the effect of laser pulse energy on the jet dynamics of the cell-free transfer, we repeated the above-mentioned time-resolved study in variation of laser pulse energy, while keeping the focus depth fixed at 52 µm. The time lapse series for pulse energies from 0.4 to 7 µJ are shown in Figure 3.7. By using a pulse energy of 0.4 µJ a protrusion can be observed above the free liquid surface which is then "pulled back" to the surface after 10 µs. At a pulse energy of 1 µJ, the primary droplet with a diameter of about 33±2 µm separates from the first jet at a delay time of 40 µs and reaches the acceptor slide at 140 µs. The following second jet has not enough energy to evolve further and is attracted back to the reservoir (see Figure 3.7, 1 µJ). Above 2 µJ, both, the first and the second jet are able to reach at the acceptor slide, resulting in an abrupt increase of the transferred hydrogel spot diameter on the acceptor slide from 71±6 µm at 1 µJ to 144±9 µm at 2 µJ (Figure 3.8c). At 3 and 4 µJ both, the first and second jet, develop with higher velocity and then arrive at the acceptor slide. The first jet reaches the acceptor slide before the breakup of the primary droplet occurs. As the laser pulse energy further increases to 5 and 7 µJ, the first jet develops with a velocity above 100 m/s and tends to become splashing and unstable entering a turbulent regime, which is undesired for the transfer (see Figure 3.7). By increasing laser pulse energies, a larger and faster expanding protrusion can be found above the hydrogel surface and the jet velocity increases from 7.3±0.2 m/s at 1 µJ to 38±1 m/s at 4 µJ (see Figure 3.8a). The aspect ratio is the ratio of the jet height to width (FWHM: full width at half maximum). As the first jet is progressively thinning, the aspect ratio is calculated at a constant delay time of 10 µs. As shown in Figure 3.8b, by increasing the laser pulse energy, the aspect ratio of the first jet increases from 3.8±0.7 at 1 µJ to 17±2.4 at 4 µJ, and the width of the first jet decreases slightly from 35±3 to 24±3 µm. At 1 µJ, the transferred hydrogel spot on the acceptor slide can only be obtained from the first jet (Figure 3.8d, red area), however above this laser pulse energy both, the first and second jet, can be transferred to the acceptor slide and result in a large hydrogel spot (Figure 3.8d, green area). As a conclusion, a narrower and faster jet can be observed by increasing laser pulse energy, resulting in larger hydrogel spot at acceptor surface.
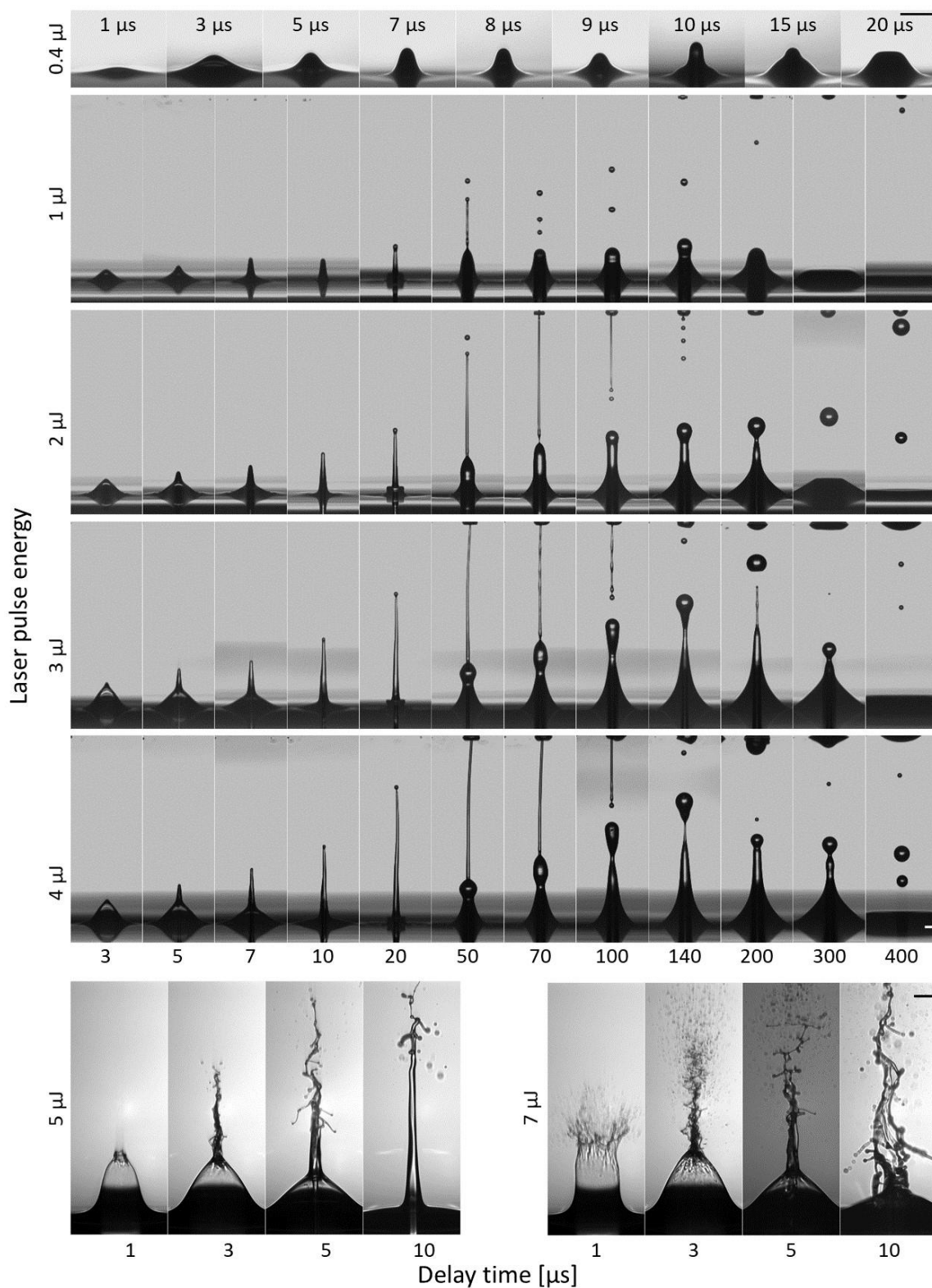
Figure 3.7 Representative time-resolved images of laser-induced transfer of cell-free hydrogel (3 independent jets) versus laser pulse energy, while keeping the focus depth fixed at 52 µm. By using higher laser pulse energy, jet behavior can change from no material transfer (0.4 µJ) to well-defined jetting (1-4 µJ) and to undesirable jetting in pluming/splashing form (5 and 7 µJ). All scale bars are 50 µm.

34
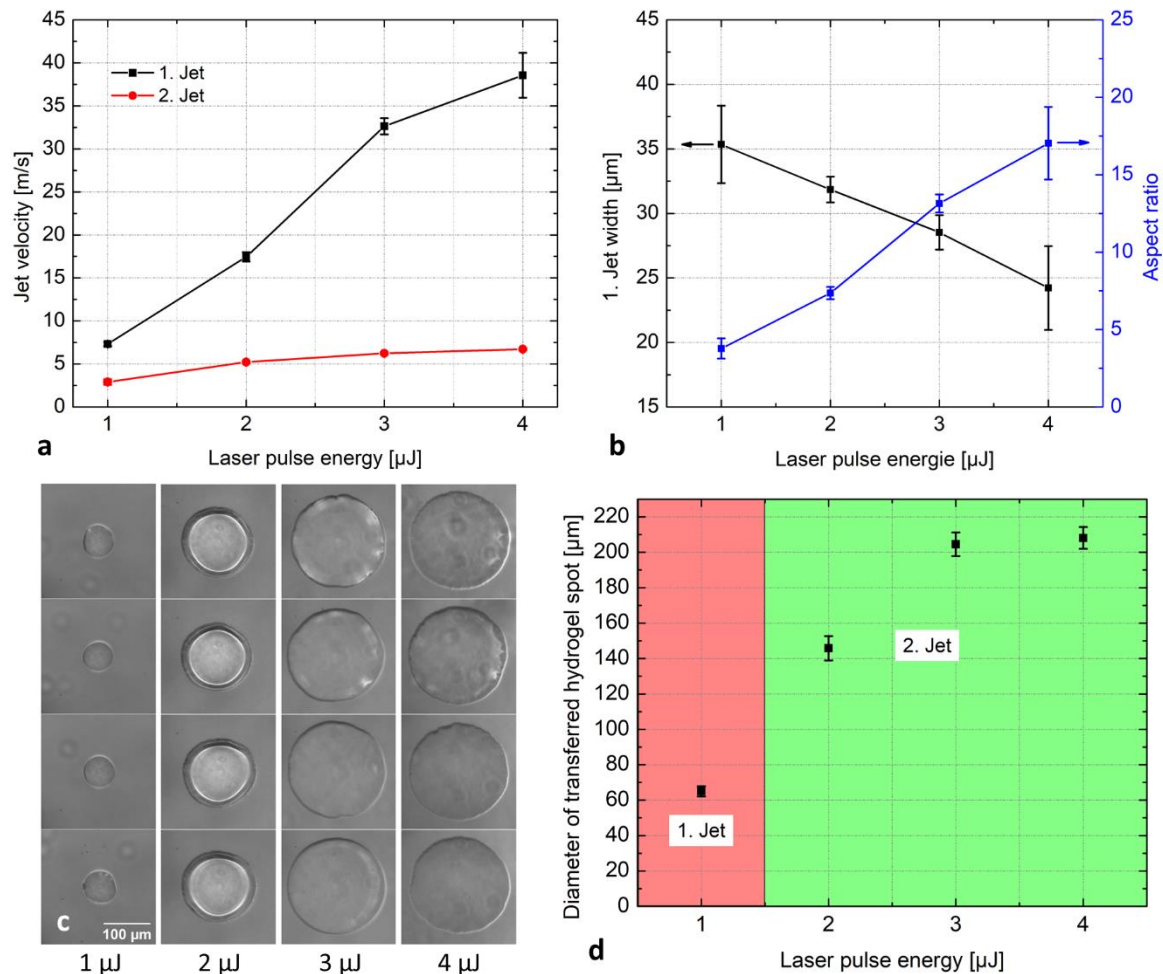
Figure 3.8 (a) Plot of the first jet and second jet velocity and (b) the first jet width and aspect ratio at constant delay time of 10 μs versus laser pulse energy. All data points in (a) and (b) represent average values ± standard deviations of 3 independent jets. (c) Bright field microscope images of the printed hydrogel spots on the acceptor slide and (d) the corresponding hydrogel spot diameters with varying laser pulse energies. In the red area the small hydrogel spots origin only from the first jet, in the green area larger hydrogel spots origin from first and second jet. The data points in (d) represent average spot diameters ± standard deviations of at least 30 independent hydrogel spots.

As mentioned above, at low jet velocities there is no material transport, while increasing velocities lead to a laminar jet until an undesirable jet in a splashing form occurs at too high velocities. Besides the change of jet behavior, an abrupt increase of the hydrogel spots size on the acceptor slide can be observed due to the transfer of the second jet. Because the spatial printing resolution is defined by the spot size, minimizing this value is of high interest, when aiming at maximal printing resolution. Figure 3.9a and b show the transfer process and corresponding transferred hydrogel spots on the acceptor slide when slightly increasing the laser pulse energy, while keeping the focus depth fixed at 52 μm. At 0.75 μJ, the first jet reaches its maximum height about 150 μm at 15 μs and then is pulled back to the reservoir without the transfer of hydrogel. Figure 3.9d shows the complete jet process by

using a pulse energy of 0.8 µJ, the first jet propagates straight up with a velocity of 5.6±0.8 m/s. A primary droplet with a diameter of 32±3 µm separates from the 15±2 µm wide jet at a delay time of 60 µs. Subsequently, the primary droplet propagates with a final velocity of 1.7±0.3 m/s, reaches the acceptor slide and finally spreads on the acceptor slide to a spot diameter of 55±3 µm. As the laser pulse energy slightly increases up to 1.2 µJ, the first jet breaks up into multiple droplets, propagating on the same trajectory (Figure 3.9a) and also reach the acceptor slide and where they generate a slightly larger hydrogel spot (Figure 3.9c). However, an abrupt transition of the transferred spot diameter from 67±4 µm at 1.2 µJ to 134±9 µm at 1.4 µJ can be observed due to the additional generation of the second jet as shown in Figure 3.9a. The smallest hydrogel spot on the acceptor slide can be obtained by using an energy of 0.8 µJ, which can be defined as the threshold energy for the transfer of the first jet.
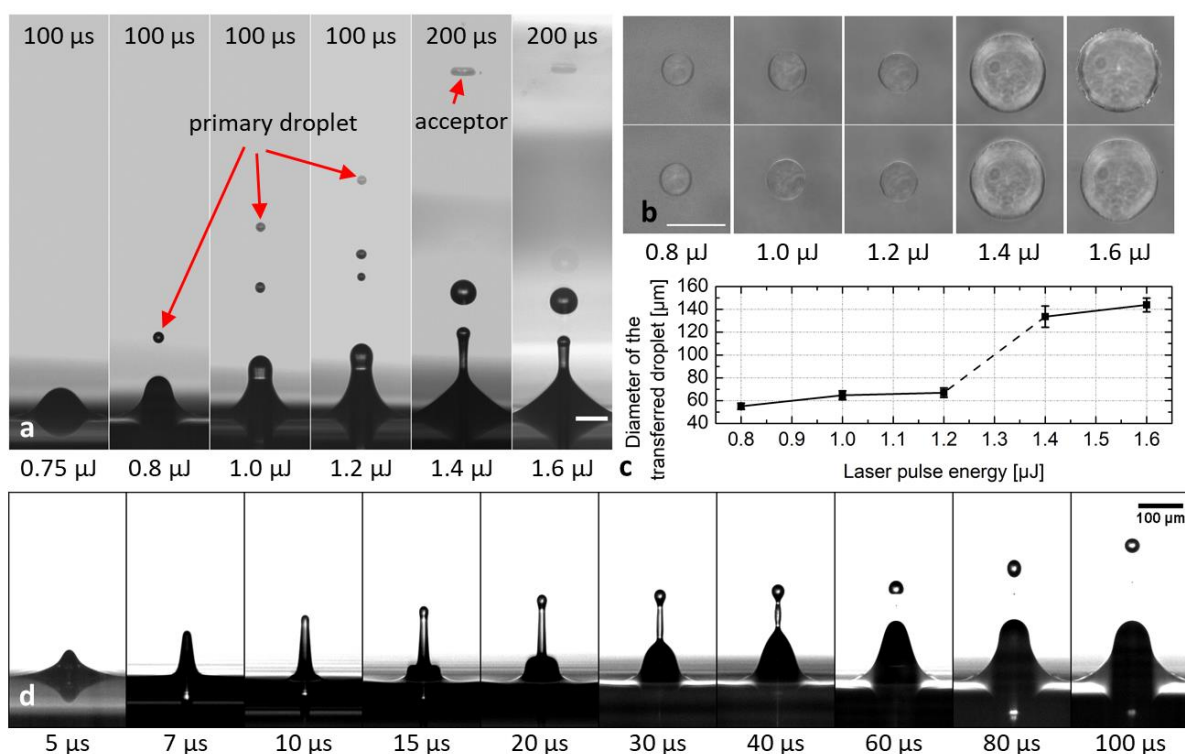

Figure 3.9 (a) Representative images of the jet process (3 independent experiments) at slightly different pulse energies around first jet threshold at a fixed focus depth of 52 µm. (b) Microscope image of the corresponding transferred hydrogel spots on the acceptor slide and (c) their diameters (mean ± standard deviation) versus pulse energy, which were obtained from at least 40 independent hydrogel spots. (d) Representative time-resolved image of the breakup process of the first jet (3 independent experiments) by using the threshold energy of 0.8 µJ. All scale bars are 100 µm.

3.1.4.3 Effect of laser focus depth on cell-free jet dynamics

Besides the laser pulse energy, the jet behavior is significantly controlled by the laser focus depth (the distance between the bubble centroid to the liquid surface). To investigate the influence of laser focus depth on jet dynamics of the cell-free hydrogel, a series of time-resolved images using variable laser focus depths was carried out, while the laser pulse energy remained fixed at 2 μJ (in Figure 3.10).

At a laser focus depth of 26 μm, the first jet develops with a velocity about 100 m/s and tends to become splashing and unstable entering a turbulent regime, which is undesired for printing. At a laser focus depth of 39 μm the first jet exhibits a width of 18±2 μm and propagates in slightly curved shape with a velocity of 43±1 m/s (Figure 3.11a). The second jet with a width of about 85 μm can be observed behind the first jet at a delay time of 20 μs, which propagates with a velocity of 5.4±0.2 m/s and reaches to the acceptor slide at a delay time of 200 μs. At a focus depth of 65 μm the first jet has a width of 48±2 μm and develops straight up with a much slower velocity of 5.8±0.2 m/s. A primary droplet with a diameter of 43±2 μm separates from the first jet and reaches the acceptor slide later at a delay time of 140 μs. The following second jet reaches its maximum height at delay time of 200 μs and afterwards drops back to the hydrogel surface, resulting in an abrupt decrease of the transferred hydrogel spot diameter on acceptor slide from 144±9 μm at a focus depth of 52 μm to 80±3 μm at a focus depth of 65 μm (Figure 3.11c). As the focus depth is further increased to 78 μm, only a weak protrusion can be observed at the surface and no hydrogel can be transferred. The width of the first jet increases with the focus depth resulting in a lower aspect ratio as shown in (Figure 3.11b). For low focus depths of 39 and 52 μm, large hydrogel spots can be obtained on the acceptor slide from the both jets (Figure 3.11d, green area). However, at a focus depth of 65 μm only the first jet can be transferred to the acceptor slide, resulting in a much small hydrogel spot with a diameter of 80±2 μm (Figure 3.11d, red area).
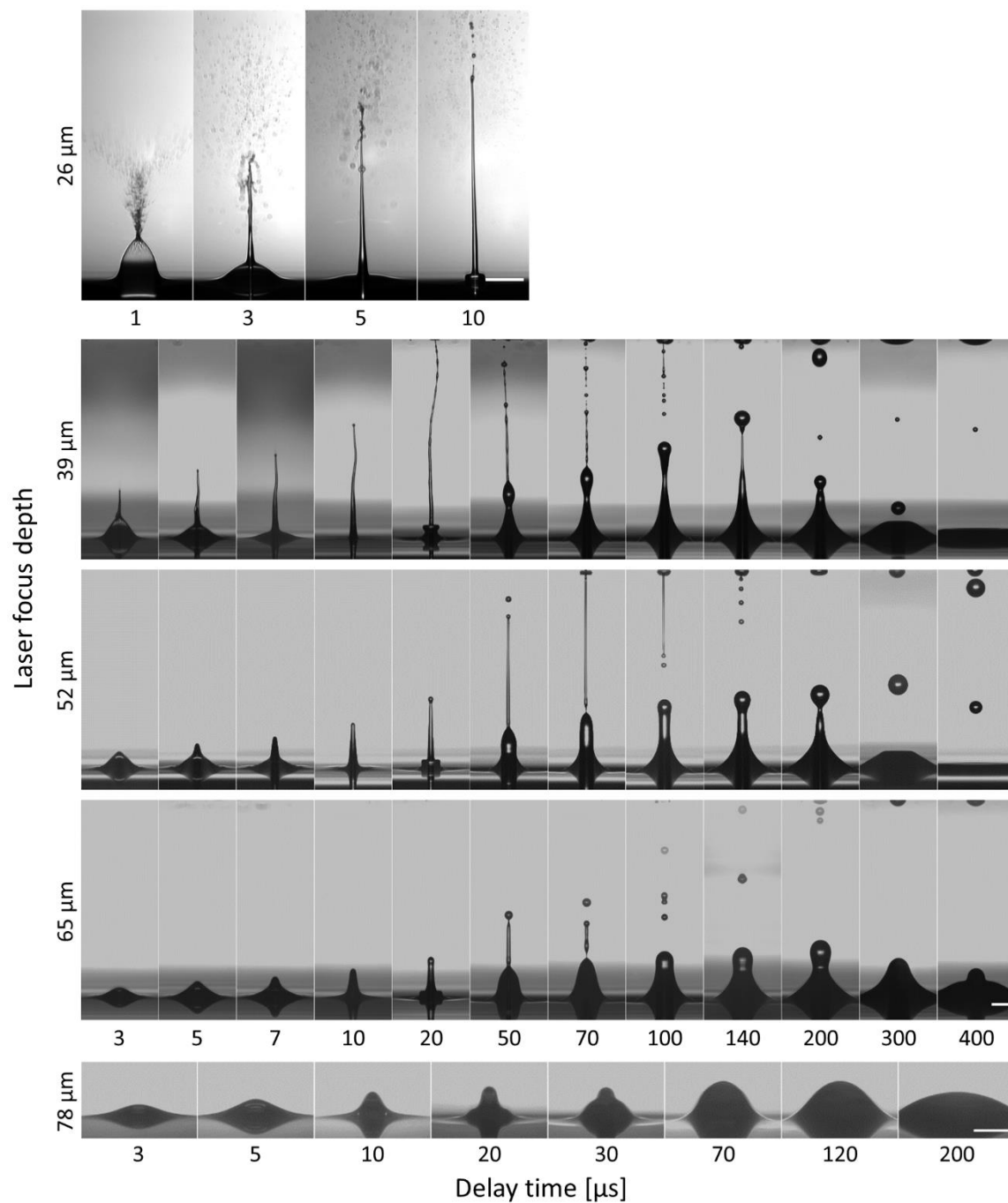
Figure 3.10 Representative time-resolved image series of laser-induced transfer of cell-free hydrogel (3 independent experiments) in variation of the laser focus depth at a constant pulse energy of 2 µJ. By increasing focus depth, the jet behavior can change from undesirable curved (39 µm) to well-defined jetting (52 and 65 µm) and to no material transferring (78 µm). Scale bar is 100 µm.
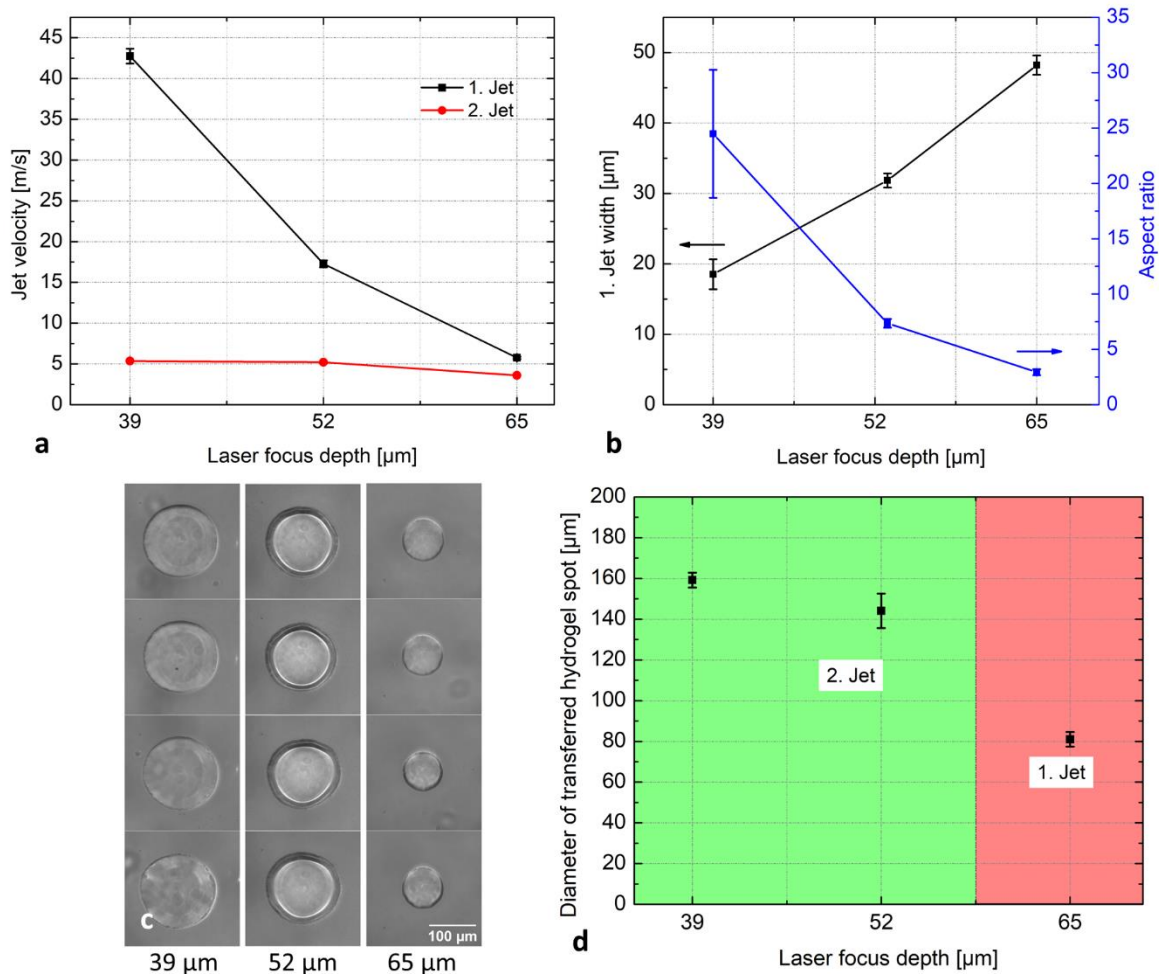
Figure 3.11 (a) Plot of the first jet and second jet velocity versus the laser focus depth. (b) and the first jet width and aspect ratio at constant delay time of 10 µs. All data points in (a) and (b) represent average values ± standard deviations of 3 independent jets. (c) Bright field microscope images of the printed hydrogel spot arrays on acceptor slide and (d) the corresponding diameter with varying laser focus depth. In the red area the small hydrogel spots come from the first jet, the larger hydrogel spots in the green area come from first and second jet at lower focus depths. The data points in (d) represent average spot diameters ± standard deviations of at least 30 independent hydrogel spots.

Figure 3.12a presents the jet process for using this threshold energy for varied focus depths from 39 to 78 µm. As expected, the threshold energy for the transfer of hydrogel increases from 0.4 µJ at focus depth F_d=39 µm to 0.8 µJ at F_d=52 µm to 1.4 µJ at F_d=65 µm and to 2.3 µJ at F_d =78 µm. The corresponding minimal hydrogel spot, which printing resolution, increases from 42±3 µm to 55±3 µm to 68±4 µm and to 78±4 µm (see Figure 3.12b), respectively. Figure 3.12c displays a plot of the spot diameter on the acceptor slide versus the laser energy, where each data point was calculated from at least 50 hydrogel spots.
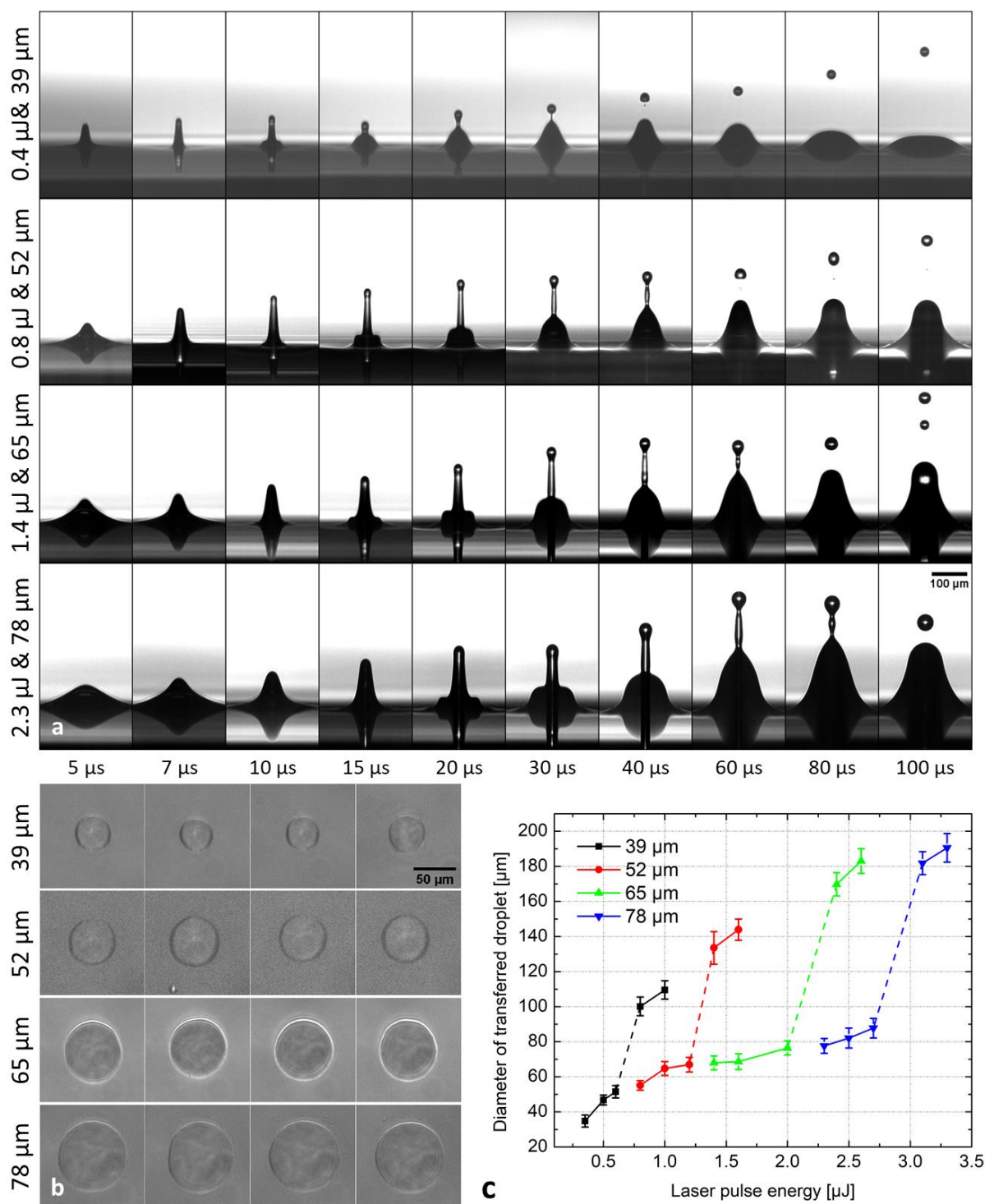
Figure 3.12 (a) Representative time-resolved images of the breakup process of the first jet (3 independent jets) by applying the threshold energy to the corresponding focus depth of 39 to 78 μm. (b) Microscope image of these transferred hydrogel spots on the acceptor slide and (c) plot of the transferred spot diameter versus pulse energy. The data points in (c) represent average spot diameters ± standard deviations of at least 50 independent hydrogel spots.

3.1.4.4 Effect of hydrogel viscosity on cell-free jet dynamics

"To investigate whether our approach can also be used for the 3D printing of higher viscos hydrogels, we investigated how the transfer kinetics are affected by the viscosity of the

gels. Figure 3.13 shows the kinetics of the hydrogel jet for pure histopaque and for three different alginate concentrations (0.5%, 1% and 1.5% alginate dissolved in histopaque) with viscosities of 13, 48, 140, and 450 mPas, respectively, using 2, 3, and 4.2 μJ pulse energy. As expected, for 2 μJ pulse energy, the final jet velocity decreases from 18.8 ± 0.6 m/s for pure histopaque to 14 ± 0.6 m/s for 0.5% alginate and to 4.1 ± 0.3 m7s for the 1% alginate hydrogel (see Figure 3.14a). For 1.5% alginate and 2 μJ pulse energy, the kinetic energy of the hydrogel jet is insufficient to overcome the surface tension of the air–hydrogel interface and the jet collapses without leaving the hydrogel reservoir. A pulse energy of 3 μJ is still not sufficient for a successful transfer. However, if the laser pulse energy is increased to 4.2 μJ, even at 1.5% alginate concentration and a viscosity of 450 mPas, the jet overcomes the surface tension of the air–hydrogel interface, escaping from the hydrogel reservoir with a velocity of 4.9 ± 0.4 m/s (see Figure 3.14b). Alginate is a frequently used hydrogel for bioprinting applications, where it is usually cross-linked with calcium, immediately after printing. At 1.5%, the alginate concentration is just high enough for 3D printing, if the alginate is cross-linked with calcium, for example, through a calcium containing hydrogel on the acceptor side (96)*".*
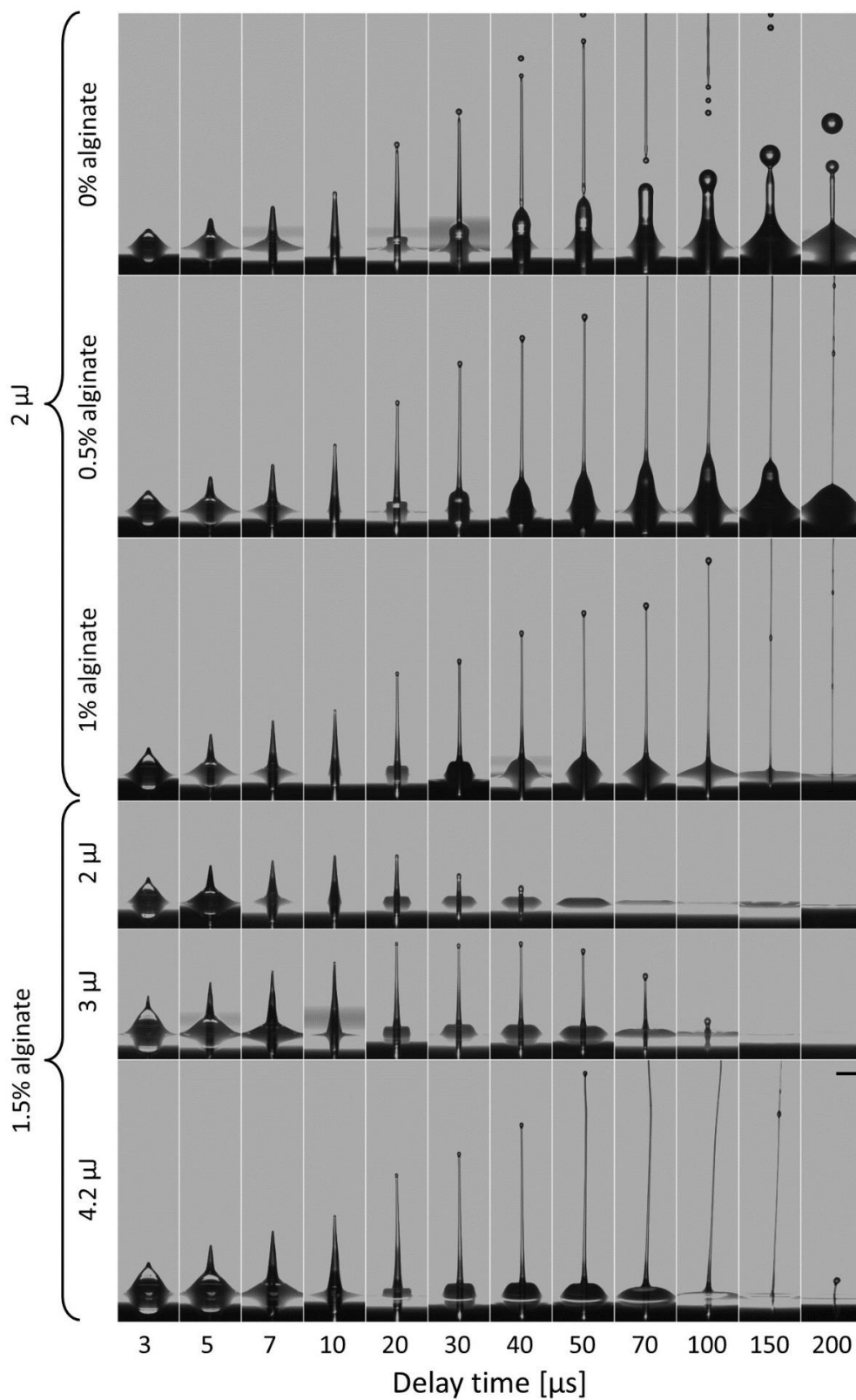The text is obtained from the article (22).

Figure 3.13 Representative time-resolved images of laser-induced transfer (5 independent jets) of hydrogel (histopaque 1083) supplemented with different concentrations of alginate. Scale bar = 100 µm (22). The figure has been published in article (22).
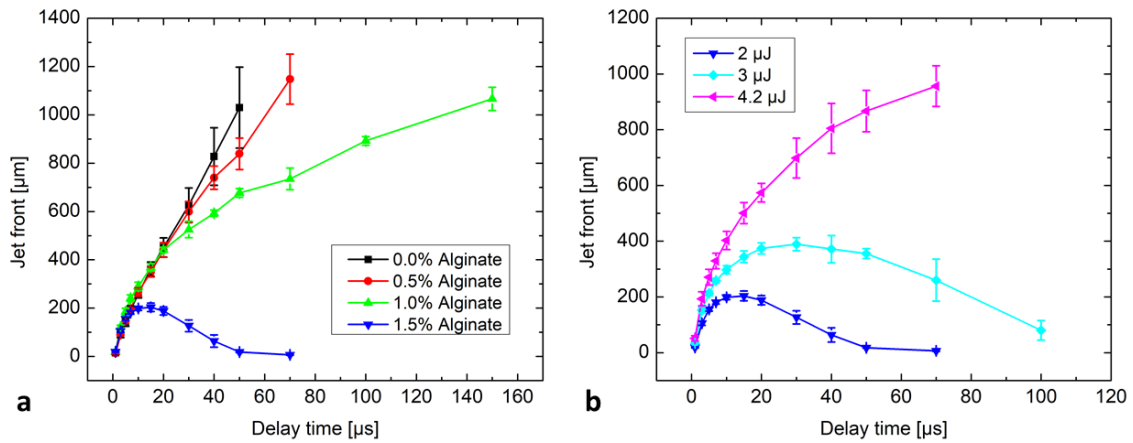
Figure 3.14 (a) Kinetics of the first jets with a laser pulse energy of 2 μJ are plotted versus the delay time. The jet velocities decrease with increasing viscosity. (b) Kinetics of the first jets of 1.5% alginate hydrogel are plotted versus the delay time, for 2, 3 and 4.2 μJ pulse energies. All data points in (a) and (b) represent average values ± standard deviations of 5 independent jets. The figure has been published in article (22).

3.1.4.5 Hydrodynamic analysis of cell-free transfer

In addition to the transfer parameters and a quantitative analysis of the jet geometry and kinetics, as it was presented for the cell-free transfer, now also the hydrodynamic properties are investigated by calculating Weber and Reynolds numbers of the jet at different laser pulse energies and focus depths (see Table 3.2). The Weber number is often useful in analyzing the mechanics of the fluid jet and describes the ratio of kinetic energy of the propagating jet relative to surface energy. The Reynolds number describes the relationship of inertial forces to viscous forces indicated by the internal movements within the fluid (see **chapter** 2.3 for details). As the first jet is progressively thinning during propagation, for calculation of the Weber and Reynolds numbers we determined the width d and velocity v of the first jet at a constant delay time of 10 μs, which is before the second jet appeared and noticeably affected the development of the first jet. We assumed that the rheological properties of the hydrogel (density ρ, surface tension σ and dynamic viscosity μ) remain constant during the printing process.

As mentioned above, only a weak protrusion can be observed at the surface and no hydrogel can be transferred in Figure 3.7 (E_p=0.4 μJ) and Figure 3.10 (F_d=78 μm) with a Weber number less than 4 and Reynolds number less than 10, which is indicated in gray in Table 3.2. In this case, the kinetic energy for jet propagation is insufficient overcomes the surface energy. By increasing laser pulse energies or decreasing focus depths, a larger and faster expanding protrusion can be observed at the hydrogel surface leading to faster and narrower jets. The

first jet develops in laminar form (green in Table 3.2) with a low velocity below 20 m/s ($4 < W_e < 200$ and $10 < R_e < 50$) by using low laser pulse energy (E_p=1-2 µJ) or high focus depth (F_d=52-65 µm). A primary droplet is formed and separates from the tip of the first jet and the breakup length (see Figure 2.6) increases with jet velocity. By future increasing the laser pulse energy or decreasing the focus depth, slightly curved jets (yellow in Table 3.2) can be observed in Figure 3.7 (E_p=3-4 µJ) and Figure 3.10 (F_d=39 µm) with a jet velocity $30 < v < 50$ m/s ($400 < W_e < 1000$ and $50 < R_e < 100$). As the jet velocity future increases above 100 m/s and the corresponding $W_e > 1000$ and $R_e > 100$ (red in Table 3.2), the jet develops in splashy form and the breaks up into lots small droplets as shown in Figure 3.7 (E_p=5-7 µJ) and Figure 3.10 (F_d=26 µm). We therefore assume that more kinetic energy can be converted for the jet propagation by increasing pulse energies or decreasing focus depths.

Table 3.2 the first jet width, velocity and the corresponding Weber number as well as Reynolds number versus (a) pulse energies and (b) focus depths. As the Weber or Reynolds number increases, the jet behavior can change from no material transfer (gray), to a laminar jet (green), to curved jet (yellow) and to an undesired splashing jet (red). All data represent average values ± standard deviations of 3 independent jets.

a)	Focus depth fixed at 52 µm				b)	Pulse energy fixed at 2 µJ			
E_p [µJ]	d [µm]	v [m/s]	W_e	R_e	F_d [µJ]	d [µm]	v [m/s]	W_e	R_e
0.4	99±7	1.4±0.4	2.9±1.7	3±0.9	26	~10	>100	>1500	>100
1	35±3	7.3±0.2	28±3	22±2	39	17±3	43±1	458±91	60±12
2	32±1	17.5±0.5	144±10	46±2	52	32±1	17.5±0.5	144±10	46±2
3	29±1	33±1	453±35	78±4	65	48±2	5.8±0.2	24±1	23±1
4	24±3	38±1	536±72	78±11	78	55±5	1.4±0.2	1.6±0.5	6±1
5	18±2	>100	>2700	>150					
7	- -	>150	>3000	>200					

Table 3.3 displays the jet velocity width as well as the calculated Weber and Reynolds numbers, which is similar to the effect of pulse energy on jet behavior in Table 3.2, both the Weber and Reynolds numbers increase with pulse energy. However, by increasing the alginate concentration from 0% to 1.5%, the Weber and Reynolds numbers sudden drop, resulting the jet behavior change from laminar jets to no material transfer. This jet behavior depending on the hydrogel viscosities can be explained by the Ohnesorge number, which characterizes the importance of hydrogel viscosity in flows. The Ohnesorge number increases from about 0.3 to 10 by increasing the hydrogel viscosity from 13 to 450 mPas (Table 3.4). Higher viscosity induces more resistance (i.e. shear force) for the deformation of the hydrogel in relative motion, such as the bubble expansion and jet propagation. Thus, more kinetic energy as well

as higher Weber and Reynolds numbers are required for transfer of higher viscos hydrogel due to higher dissipation effect. The relationship between these three dimensionless numbers will be discussed in **capital** 4 in more detail.

Table 3.3 Jet width, velocity and the dimensionless numbers of jets with the variation of the hydrogel viscosity. All data represent average values ± standard deviations of 3 independent jets.

Alginate %	E_p [µJ]	d [µm]	v [m/s]	W_e	R_e	O_h
0	2	21.2±0.4	26.0±1.0	173±10	46±2	0.29±0.01
0.5	2	19.5±1.5	26.3±2.1	149±26	43±5	1.05±0.04
1	2	16.0±0.2	20.4±2.1	78±8	27±3	3.49±0.2
1.5	2	3.7±1.7	23.9±1.0	5±4	7±4	10.4±0.2
1.5	3	11.0±1.1	22.8±2.4	41±9	21±3	10.6±0.6
1.5	4.2	22±1.1	16.9±2.0	117±20	30±4	12.3±0.7

3.1.5 Investigation of laser-based parameter under cell-laden conditions

3.1.5.1 Determining the location of the transferred cells within the jet

To investigate the effect of the embedded cells on the jetting process, and to analyze potential cell-damage sources and further optimize the printing quality, a time-resolved study of the cell-laden jet was carried out. Here the pulse energy of the femtosecond transfer laser was set to 2 µJ and the focus depth to 52 µm. Figure 3.15a presents bright field images of the groups of cells at the surface of the hydrogel before (top) and after printing (middle), and transferred cells at acceptor slide (bottom). Eight cells lie within a radius of about 100 µm (red dashed line) around the laser focus (red cross). After the laser pulse has induced jet formation, they have disappeared from the reservoir and transferred to the acceptor slide, indicated by black arrows. More distant cells were pulled closer to the laser focus (cyan arrows). A corresponding time-resolved image from the propagating jet at a delay time of 20 µs was captured and displayed in Figure 3.15b. Four cells can be found within the base of the first jet (green arrows). They most likely correspond to the cells within the green dashed circle before printing (Figure 3.15a, top). One or two other cells are located in the second jet indicated by the red arrow in Figure 3.15b, which could correspond to the cells between the green and the red dashed circles before printing. Due to a random cell distribution, the amount of cells per transfer can hardly be controlled.
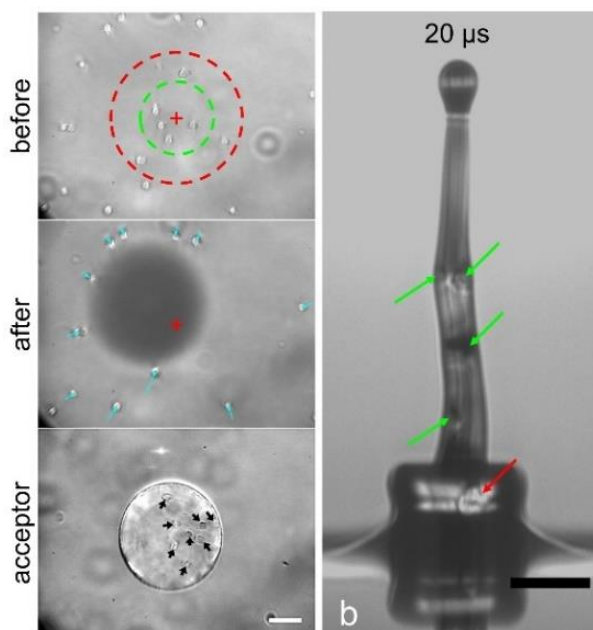
Figure 3.15 (a) Bright field images of the B16F1 cell suspension at hydrogel surface before (top) and after (middle) printing, and transferred cells (bottom) at the acceptor slide. (b) Time-resolved representative images at a delay time of 20 µs. Scale bar is 50 µm. Representative figure from 3 independent experiments.

To determine the location of one single transferred cell within the laser-induced jet, the time-resolved fluorescence visualization was carried out by using the green frequency-doubled q-switched ns laser instead of white spark flash-lamp (see Figure 3.1 for details). "*Figure 3.16 displays three time series of the transfer process recorded with a 5 ns time resolution. The top row highlights an Alexa Flour 532 labeled B16F1 cell, 1, 3, 5, 7, 10, 15, and 20 µs after the arrival of the NIR transfer pulse. The middle row shows the transfer of a B16F1 cell, which is not fluorescently labeled. The bottom row shows the plain hydrogel jet without the presence of any cells. Both images on the right are close-ups of the images at 3 and 10 µs. To visualize the hydrogel jet in the fluorescence images, Alexa 532 was added to the hydrogel, obtaining a concentration of 0.02mM for all three time series (see materials and methods section 2.4.2 for details of the cell and hydrogel staining). Here, the pulse energy of the fs transfer laser was set to 2 µJ and the focus depth to 52 µm. In the top row, the labeled cell can be clearly identified by the bright circular fluorescence signal at the tip of the hydrogel jet. The cell's fluorescence intensity at 10 µs corresponds to ~4900 counts, using a 14-bit CCD camera, with a full well capacity of 16,000 e⁻ and a gain of one. In the time series with the unstained cells (middle row), a black circle at the tip of the jet (~900 counts @ 10 µs) indicates a lack of fluorescent molecules at the position where the (unstained) cell is located. If no cell is present (bottom row), only the fluorescence signal from the hydrogel (~1500 counts @ 10 µs) can be*

observed. The horizontal stripes, which are present in all images, are most likely interference patterns caused by the ns illumination laser. Note again, that each time point shown corresponds to a new cell transfer, recorded with different delay time between NIR fs transfer pulse (as pump-pulse) and a 5 ns pulse of the green illumination laser pulse (as probe-pulse) in the observation path. The fact that almost no jitter is observed within the three time series, demonstrates the high reproducibility and robustness of the transfer process. The subtle differences in jet shape between labeled und unlabeled cells observed at 3 µs (see close-up in Figure 3.16) could be caused e.g. by slight differences in the initial z-position of the cells". The text is obtained from the article (22).
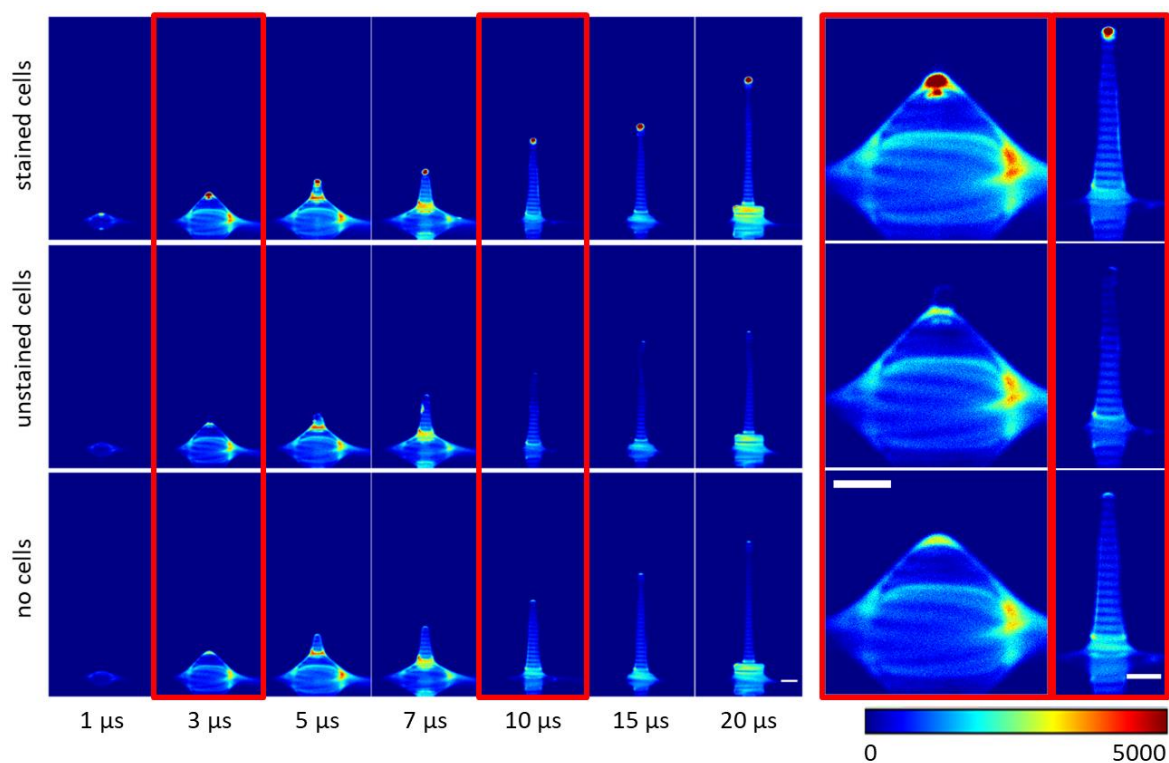

Figure 3.16 Color-coded fluorescence intensities of the time resolved fluorescence images of the transfer of an Alexa 532 labeled B16F1 cell (top row), an unstained B16F1 cell (middle row) and pure hydrogel (bottom row). In all cases Alexa 532 was added to the hydrogel, in order to also visualize the hydrogel jet. Scale bar: 50 µm. The figure has been published in article (22). Representative figure from 3 independent experiments.

"To explore the stability of the transfer process with respect to the focusing precision we introduced a lateral offset Δx between the cell to be transferred and the focus position of the NIR fs transfer laser. Figure 3.17a shows three human tendon stem/progenitor cells (hTSPC) before and after the transfer process, with an offset Δx of 0 µm, 25 and 50 µm between the x-y position of the laser focus (indicated by red cross) and the cell. In all three cases, the cell was successfully transferred to the target substrate using the same laser parameters as in Figure

3.16 (pulse energy 2 μJ, focus depth 52 μm). For a more detailed investigation of the transfer process with different offsets, we again used the optical inspection path perpendicular to the transfer direction. Instead of using the frequency-doubled q-switched ns laser, which we used for fluorescence illumination, we now used the white nanosecond spark flash-lamp for bright field illumination, rendering 28 ns time resolution. Figure 3.17b shows the time-resolved images of the transfer process for all three offsets. While for Δx = 0 μm the cell seems to be located at the very tip of the hydrogel jet, for Δx = 25 μm a small bump, indicated by red arrows, can be identified at the upper right side of the jet, which seems to correspond to the transferred cell. The close-up at 20 μs reveals a Δ15 μm circular object at Δ80% jet height (red arrow), which again seems to be the transferred cell. For Δx = 50 μm, a small bump, comparable to the one seen for 25 μm offset, can be observed at the lower right side of the hydrogel jet (again indicated by red arrows at 3 to 20 μs delay time). However, in this case, the cell is far away from the tip of the (thin) initial hydrogel jet and is not transferred with the first jet. Instead, the cell is now transferred to the target substrate with a much thicker hydrogel jet, following the first jet about 20 μs. Thus, cells are transferred efficiently with a large tolerance range". The text is obtained from the article (22).
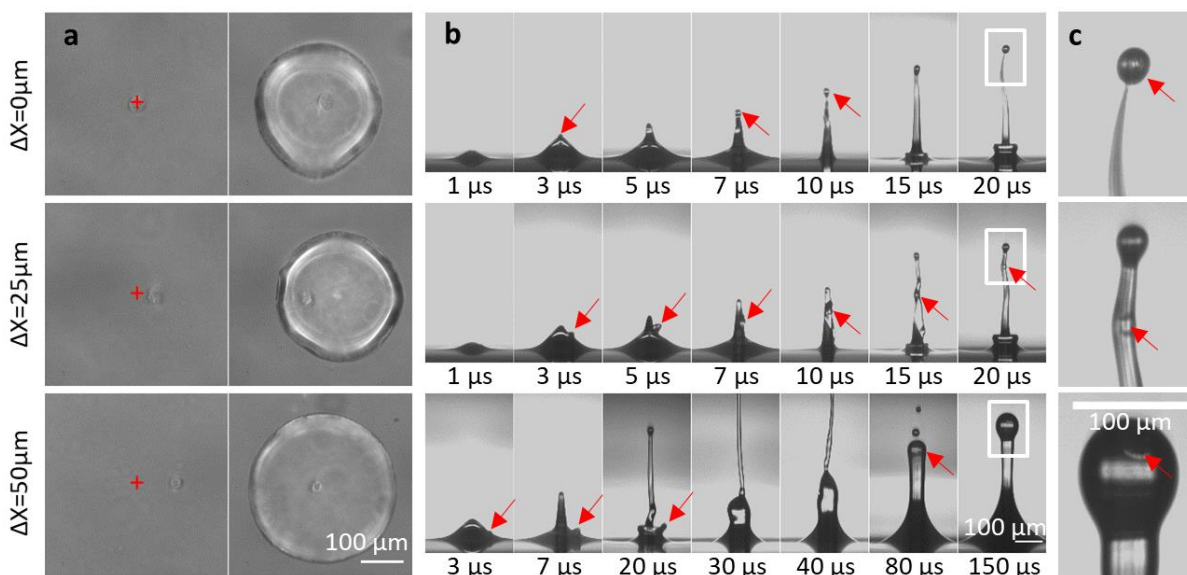

Figure 3.17 (a) Representative bright field of at least 20 human tendon progenitor cells (hTSPC) with different lateral offsets Δx between the cell and the focus position of the transfer laser, before (left) and after transfer (right). (b) Representative time-resolved images of the transfer process (3 independent jets) of single hTSPCs with different lateral offsets Δx between cell and transfer laser red circle mark cell position in the emerging jet, red arrow points at the transferred cell and (c) close-up images of the jet tip, transferred cells indicated by red arrow. Scale bars in all columns are 100 μm. The figure has been published in article (22).

3.1.5.2   Cell-laden jet dynamics versus laser pulse energy

To analyze the effect of the transferred single cell on the jet behavior, a fs pulse was focused underneath an individual selected cell ($\Delta x = 0$) with varying laser pulse energies. A cell-free transfer experiment was carried out as a control by focusing the fs-laser pulse at a position in the same reservoir, where no cells were located around the laser focus. To prove that the selected single cells were indeed transferred, the hydrogel spots on the acceptor slide were observed for each experiment. As described above (Figure 3.7), no material transfer or transfer in splashing form are undesired for the printing. Thus, for the investigation of the cell-laden jet dynamics, the pulse energy of the fs transfer laser was varied from 1 to 4 µJ.

Figure 3.18a shows the time-resolved images of cell-laden jets and the corresponding hydrogel spots on the acceptor slide. Below 2 µJ, the jet behavior of cell-free and cell-laden printing shows no significant difference: both develop straight up with a comparable velocity < 20 m/s, as shown in Figure 3.19a. With 33±2 µm, the primary droplet containing the cell exhibits a comparable diameter to the cell-free primary droplet. Above 2 µJ, however, an obviously smaller droplet with a diameter about 15±3 µm at the tip of first jet (red rectangle marked 3x zoom-in image) is formed during the early stages of the transfer process, which does not arise in cell-free jets (Figure 3.18c). The location of the single cell is similar to the observation in Figure 3.16 and Figure 3.17. Such small droplets with a diameter of about 15 µm represent the printed cells. These cells-containing droplets subsequently separate from the first jet and are transferred with a much higher velocities of 45±2 m/s at 3 µJ and 77±3 m/s at 4 µJ (see Figure 3.18a, 3 and 4 µJ, indicated by red arrows) and then impact at the acceptor slide at a delay time of 50 µs.
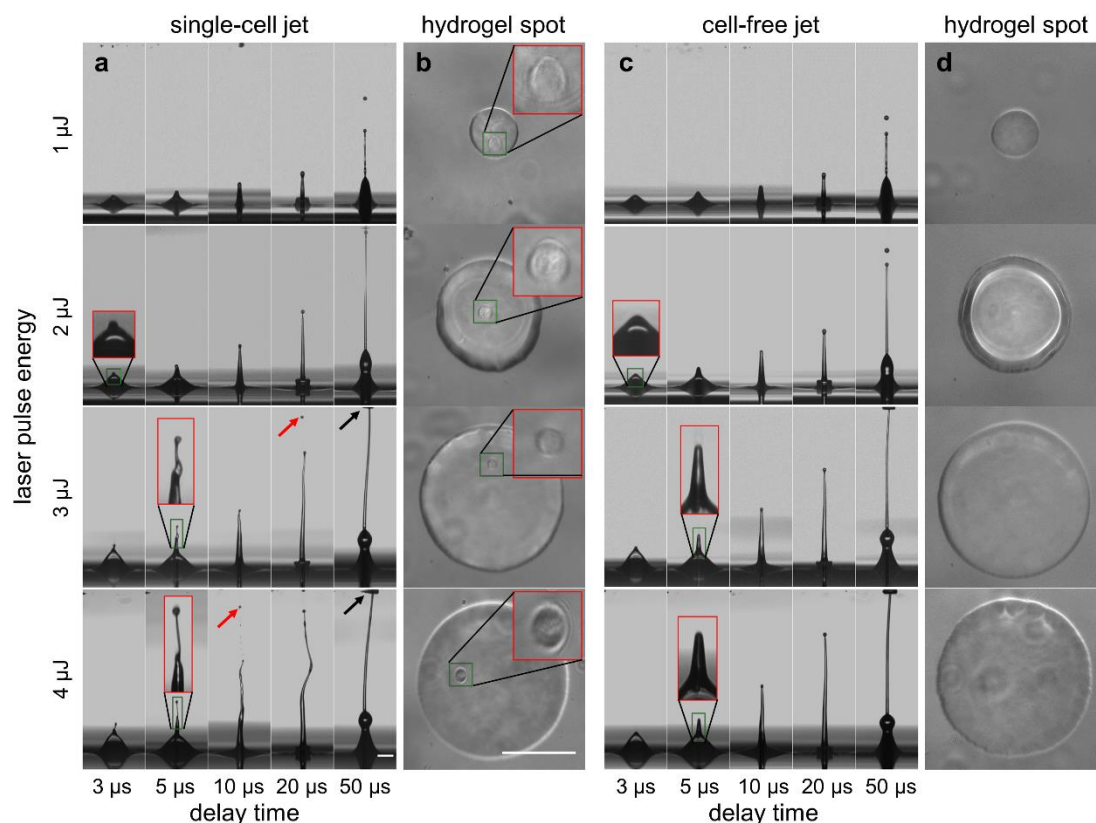
Figure 3.18 (a) Representative time-resolved images of cell-laden (single B16F1 cell) and (c) cell-free jets (3 independent jets) and (b and d) the corresponding at least 30 transferred hydrogel spots on the acceptor slide in variation of laser pulse energy from 1 µJ to 4 µJ at a constant focus depth of 52 µm. The jet process is highlighted in time steps from 3 µs to 50 µs. The lower part of the time series images shows an angled view onto the reservoir's hydrogel surface. The upper margin of the images gives an angled view onto the acceptor slide (indicated with black arrows). The red rectangles display a 3-fold magnification of the green rectangles in the respective columns. Red arrows indicate single cells separated from the jet. Scale bar is 100 µm.

By increasing laser pulse energies from 1 to 4 µJ, the first jet width of cell-laden transfer decreases from 35±5 µm to 23±4 µm (see Table 3.4) and exhibits a comparable width to the cell-free jet. For hydrodynamic analysis, above 2 µJ, as the cells separate from the jet, the first jet propagates in an obviously more curved and with an approximately 10 m/s faster velocity than the cell-free jet (Figure 3.19a). The corresponding Weber and Reynolds number of cell-laden transfer is about 250 and 15 larger than that for the cell-free jets, respectively (see Table 3.4). The transferred hydrogel spots containing the printed single cell are similar to the hydrogel spots obtained from cell-free transfer, both increase with laser pulse energies from about 67±5 µm at 1 µJ to 202±7 µm at 4 µJ (Figure 3.19b). As mentioned above, the stable second jet can also be transferred to the acceptor slide, when the pulse energy is high enough.
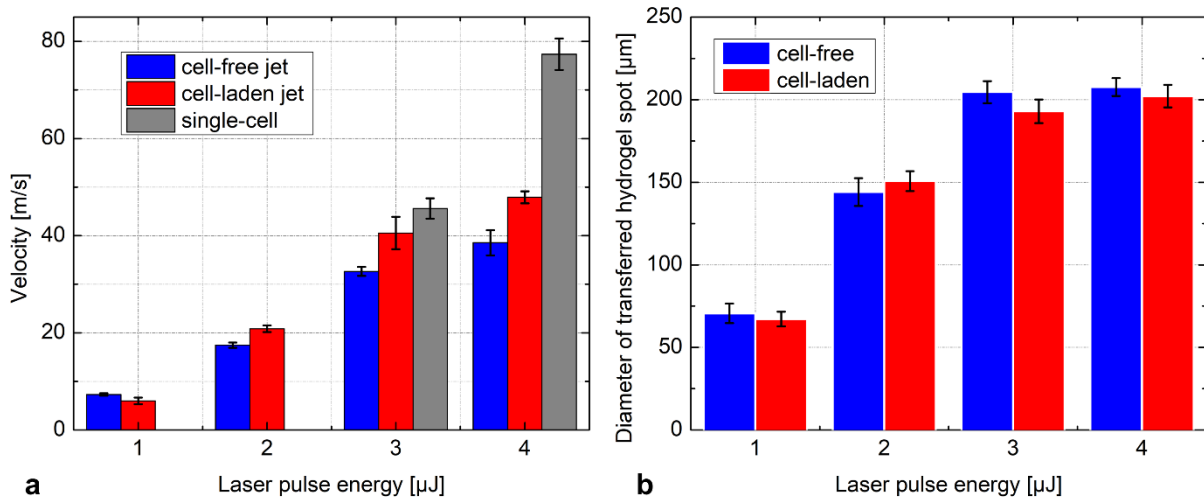
50

Figure 3.19 (a) Velocities of the cell-free, cell-laden jet and the separated single cell and (b) the diameter of the transferred hydrogel spots on the acceptor slide in variation of the laser pulse energy. The jet velocity and the obtained spot diameter are at minimum for the low energy of 1 µJ. At 3 and 4 µJ the transferred single cell separates from the first jet and shows a much higher velocity. All data points represent average values ± standard deviations of (a) 3 independent jets and (b) at least 30 independent hydrogel spots.

Table 3.4 Jet width, velocity and the dimensionless numbers of cell-free and cell-laden jets in variation of the laser pulse energy. The data represent average values ± standard deviations of 3 independent jets.

E_p [µJ]	Cell-free jet					Cell-laden jet			
	d [µm]	v [m/s]	W_e	R_e		d [µm]	v [m/s]	W_e	R_e
1	35±3	7.3±0.2	28±3	22±2		35±5	6.0±0.7	18±5	17±3
2	32±1	17.5±0.5	144±10	46±2		32±5	21±0.7	195±35	52±9
3	29±1	33±1	453±35	78±4		28±2	41±3	690±122	95±10
4	24±3	38±1	536±72	78±11		23±4	48±2	800±130	93±15

3.1.5.3 Cell-laden jet dynamics versus laser focus depth

To investigate the effect of laser focus depth on cell-laden jet dynamics, a time-resolved images of the jet process under variation of laser focus depth was carried out, while the laser pulse energy was fixed at 2 µJ. As described above, a smaller and slower expanding protrusion is generated by increasing the laser focus depth resulting in a reduced velocity of the first jet. Figure 3.20a presents the jet dynamics for different focus depths. At a focus depth of 39 µm, the printed single cell is located at the tip of a curved jet (red rectangle marked 3x zoom-in image) at a delay time of 5 µs (Figure 3.20a). Subsequently, this single cell (indicated by red arrows) separates from the first jet with a much higher velocity of 65±5 m/s, leading to an obviously tilted and curved jet compared to the cell-free jets, similar to the observation in Figure 3.18, which shows the jet dynamics in variation of laser pulse energy. The first jet propagates following an obviously more curved path with a velocity about 10 m/s faster than

the cell-free jet (see Table 3.5). The corresponding Weber and Reynolds number from the cell-laden jets is about 200 and 20 larger than that obtained from cell-free jets (Table 3.5). By increasing laser focus depth, a smaller and slower expanding protrusion can be observed at the hydrogel surface and leads to slower jets with less Weber and Reynold numbers. At a focus depth of 65 μm, the single cell was transferred within the primary droplet and its behavior is similar to the cell-free transfer. In this case, both, the cell-free and the cell-laden jets, develop with identical velocities of about 6±0.5 m/s, resulting in circular spots with identical diameters of 75±5 μm. The transferred hydrogel spots containing the single cell are similar to the transferred cell-free spots, the diameter of both decreases with laser focus depth from about 150±5 μm at 39 μm to 77±4 μm at 65 μm (Figure 3.21b), which is similar to the observation in Figure 3.19b.
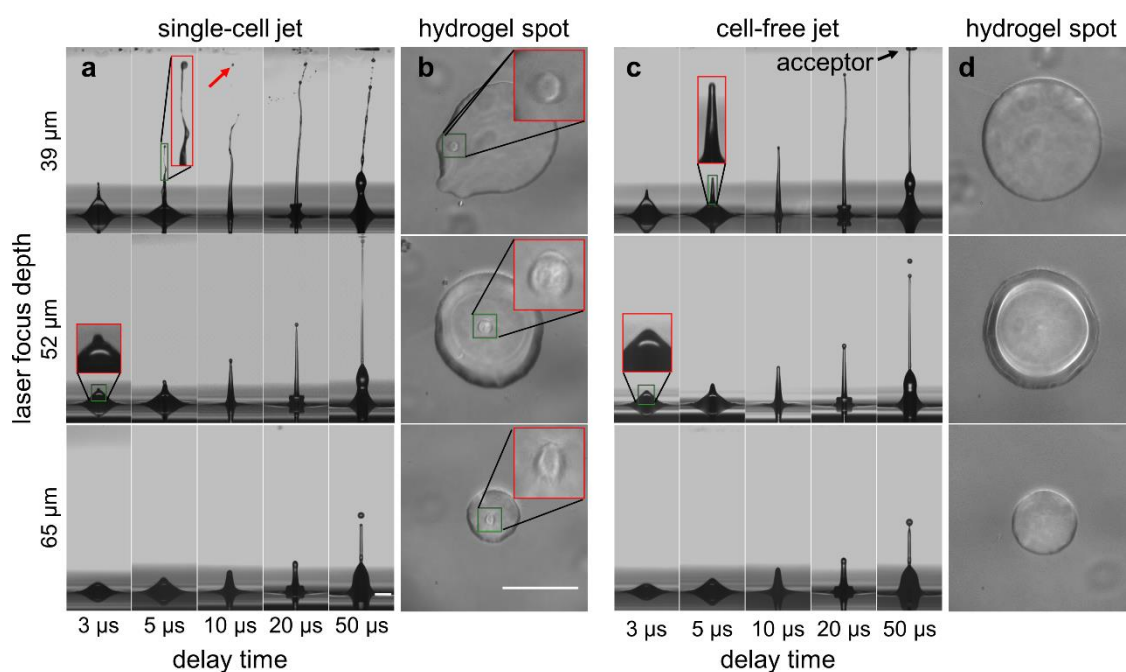
Figure 3.20 Representative time-resolved images of (a) cell-laden (single B16F1 cell) and (c) cell-free jets (3 independent jets) and (b and d) the corresponding at least 30 transferred hydrogel spots on the acceptor slide in variation of the laser focus depth, while the laser pulse energy was fixed at 2 μJ. The lower part of the time series images shows an angled view onto the reservoir surface; the upper margin is defined by the acceptor slide (indicated with black arrows). The red rectangles display a 3x magnified image of the green marked region. Red arrows indicate the separated single cell during jet propagation. Scale bar is 100 μm.

Figure 3.21 (a) Velocities of the cell-free, cell-laden jet and the separated single cell and (b) the diameter of the transferred hydrogel spots on the acceptor slide with the variation of the laser focus depth. The jet velocity and the spot diameter are minimal for the high focus depth of 65 µm. At 39 µm the transferred cell can be separated from the first jet and develops with a much higher velocity. All data points represent average values ± standard deviations of (a) 3 independent jets and (b) at least 30 independent hydrogel spots.
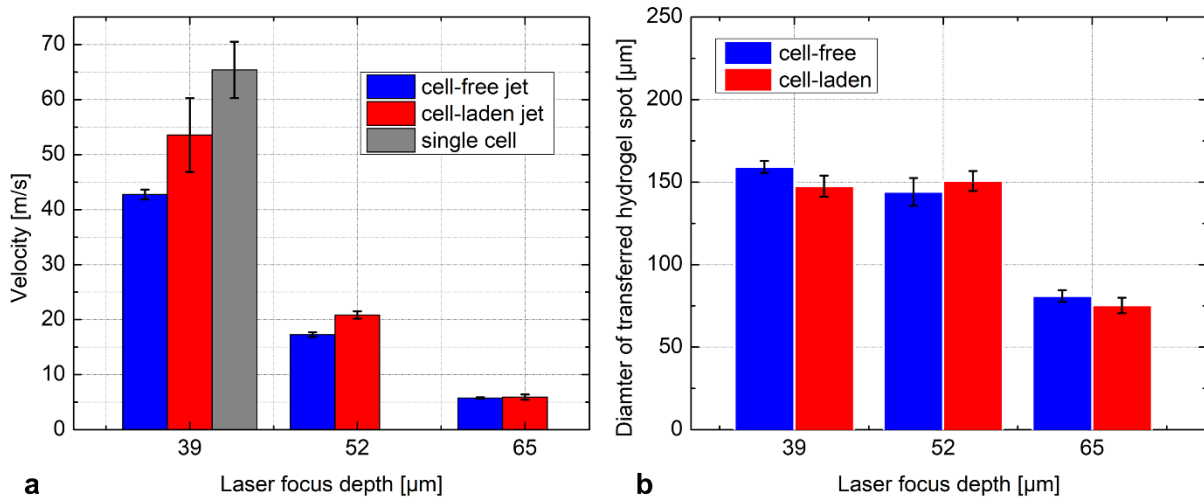
Table 3.5 Jet width, velocity and the dimensionless numbers of cell-free and cell-laden jets in variation of the laser focus depths. The data represent average values ± standard deviations of 3 independent jets.

F_d [µm]	Cell-free jet					Cell-laden jet			
	d [µm]	v [m/s]	W_e	R_e		d [µm]	v [m/s]	W_e	R_e
39	17±3	43±1	458±91	60±12		17±4	54±7	745±260	78±22
52	32±1	17.5±0.5	144±10	46±2		32±5	21±0.7	195±35	52±9
65	48±2	5.8±0.2	24±1	23±1		48±1	5.9±0.5	25±4	24±2

As a conclusion, cells can significantly affect the first jet dynamics. When the cell-laden jet develops with a velocity below 20 m/s, $W_e < 200$ or $R_e < 50$, the jet dynamics has no significant differences to the cell-free jet: both develop in a laminar form. The single cell does not separate from the first jet and is transferred within the primary droplet, which is similar to the cell-free transfer (1 µJ in Figure 3.18 or (65 µm in Figure 3.20). However, by using higher laser pulse energies (3 and 4 µJ in Figure 3.18) or lower focus depths (39 µm in Figure 3.20), the printed single cell propagates with a higher velocity than the surrounding hydrogel and even can become separated from the first jet. As the cells separate from the jet, there is almost no hydrogel surrounding the printed cells and the impact at the acceptor slide takes place with a velocity above 40 m/s. In this case, the cell-laden jet propagates in a much more curved jet form with higher Weber and Reynolds numbers.

3.1.6 Positioning accuracy of transferred cells

The spatial position accuracy of the transferred cells on the acceptor slide is a crucial parameter for future applications generating cell niches and artificial tissues. Figure 3.22a presents the hydrogel spots on the acceptor slide, each containing one single B16F1 cell, transferred by using the above-mentioned threshold energy at each corresponding focus depth. The diameter of the obtained hydrogel spots increases linearly from 48±6 µm at 39 µm focus depth to 99±5 µm at 78 µm focus depth, as shown in Figure 3.22d. To visualize deviations from the nominal target position, the location of the transferred cell is plotted into a polar coordinate system (Figure 3.22b). The average center of cell-free spots is set as the pre-designated target position (0,0) at the acceptor slide. The histogram in Figure 3.22c displays the deviation frequencies. More than 80% of the transferred cells can be positioned precisely within a 20 µm radius from the desired target position at a focus depth of 39 µm. At a focus depth of 78 µm, the cells are distributed uniformly within a 70 µm radius. A detailed analysis of the printing accuracy gives an overall positioning accuracy in our experiments (Figure 3.22e) from ±15.5 µm for 39 µm focus depth (root mean square deviation from the target position of n = 79 independent transfers) to ±26.7 µm for 52 µm focus depth (n = 33), ±31.0 µm for 65 µm focus depth (n = 38) up to ±44.2 µm for 78 µm focus depth (n = 61).

In summary, our results show that the accuracy of cell positioning is determined mainly by the variation of the cell position within the transferred hydrogel spot, which depends on the spot size. The lateral position of the cell within in a hydrogel spot cannot be controlled. Thus, the strategy to increase the printing resolution is to minimize the spot size in the transfer process. In addition, the positioning accuracy can be influenced by the focusing error, non-uniformity of the cell morphology, movement of cells at the hydrogel surface before the transfer or asymmetric distribution of the cell's center of mass.
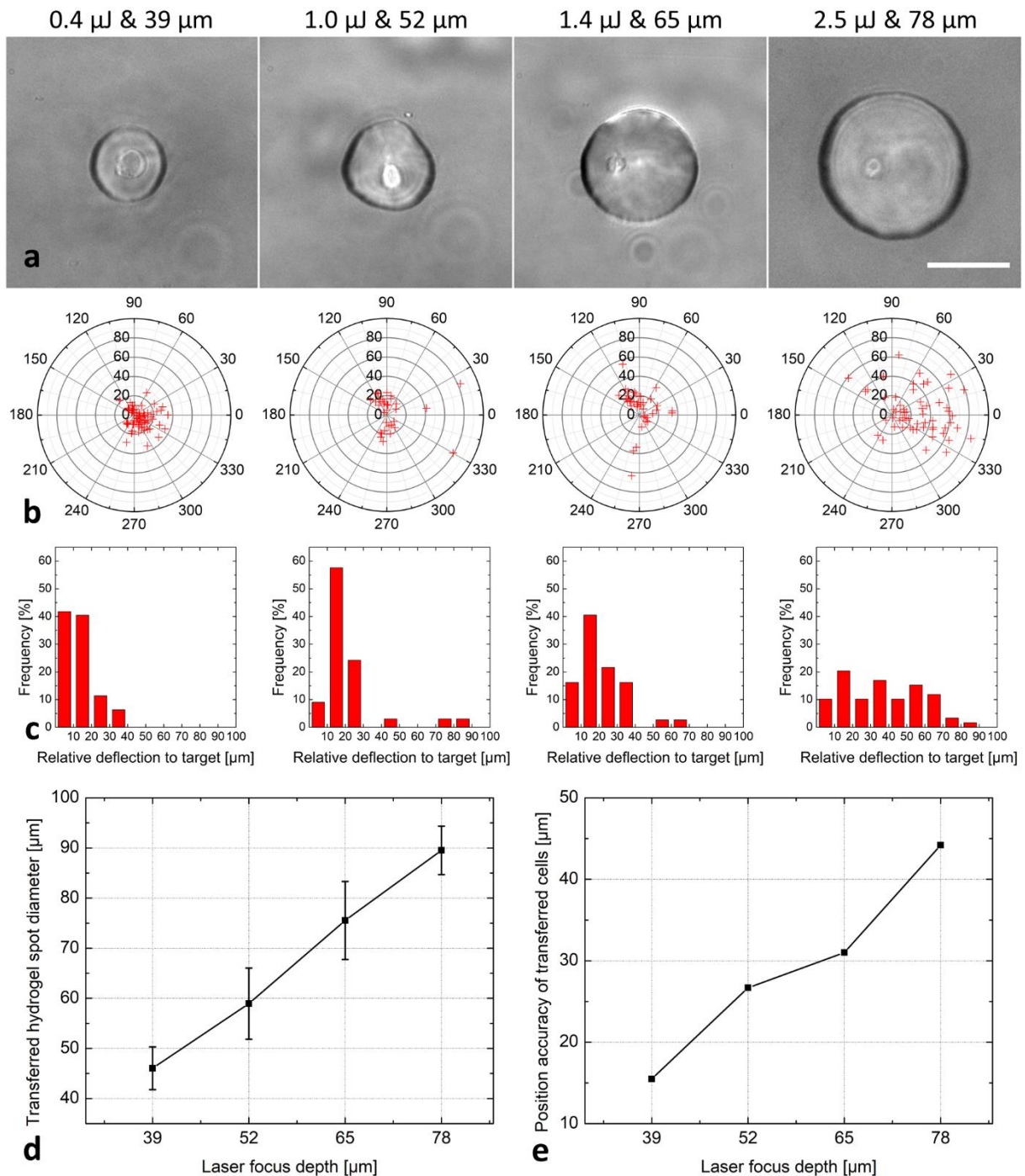
Figure 3.22 Position accuracy of the cell transfer. (a) Representative bright field microscopy images of at least 30 transferred hydrogel spots each containing one single B16F1 cell on the acceptor slide by using the threshold energy at each focus depth. Scale bar = 50 μm. (b) Deviation of the actual cell positions on the acceptor from the target position (0,0). (c) The histogram displays the frequencies of the deviations of the cell positions from the desired target point, which is obtained by dividing the number of transferred cells within the deviations from the target position to the total transferred cells. (d) The diameter of transferred hydrogel spots and (e) resulting position accuracy versus focus depth. All data points in (d) represent average values and standard deviations of at least 30 independent hydrogel spots. The data in points in (e) can be calculated by the formula 12.

3.2 Inverted configuration for fs laser-induced cell transfer

3.2.1 Laser based sorting of single cells

The laser-induced cell transfer approach was integrated into an inverted configuration based on the possibility of combining it with optical and fluorescence microscopy, which has been usually used for life science applications. "*For fs laser-induced single cell sorting and transfer, the fs laser beam was coupled into an inverted epifluorescence microscope (Nikon Ti-E) by using a dichroic mirror (Figure 3.23a), which is reflective in the NIR but transmitted in visible light. The laser beam was focused through an inverted objective, mounted in a motorized objective revolver for vertical positioning. A motorized microscope-stage was used for scanning the suspended cells in the reservoir in x-y-direction. Both, the reservoir and the acceptor surface were kept at 37°C and 90% humidity to ensure cell viability. Cell shape and size were recorded using bright field illumination. Additionally, a fluorescent light source (X-Cite 120 Q, EXFO) was installed for monitoring fluorescent-labeled cells and hydrogels. For image acquisition, a CCD camera (MMI CellCamera 1.4, MMI GmbH, Eching, Germany) was used. By switching the fluorescence filter cubes, various fluorescence markers can be identified. Figure 3.23b-c shows an example where GFP-labeled hMSCs and orange-labeled human papillary thyroid carcinoma cells (TPC1) are selected from a heterogeneous cell population (Figure 3.23b) and sorted on the target substrate based on their fluorescence. Therefore, in addition to precisely positioning individual cells on a target substrate, this technique allows for selecting individual cells prior to the transfer process based on size, morphology or fluorescence signals*". The text is obtained from the article (22).
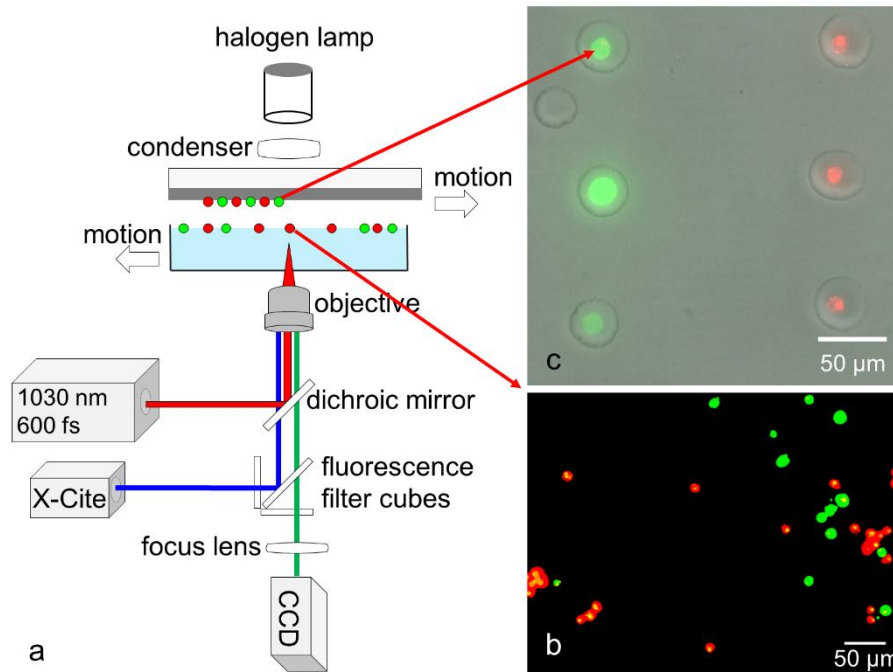
Figure 3.23 *(a) Inverted setup for femtosecond laser-induced printing and sorting of single living cells based on cell morphology and phenotype. (b) Fluorescence images of GFP-labeled SCP1 cells and orange-labeled TPC1 cells randomly suspended at the top of hydrogel in the reservoir before printing and (c) Representative bright field and fluorescence merged image of printed hydrogel spot containing a single cell (5 independent experiments) at acceptor slide. Scale bar is 50 µm. The figure has been published in article (22).*

3.2.2 Comparison of the upright and inverted configuration

For the upright configuration presented in **chapter** 3, the acceptor slide must be transparent for the laser beam. Additionally, the acceptor surface is usually coated with a hydrogel, such as alginate, collagen or fibrinogen to soften the impact of the transferred cells and prevent them from drying. The laser focus quality through the upright configuration may be influenced by optical properties of the acceptor slide including coating, such as the transmission, thickness, absorption and scattering from a thick film or 3D scaffold. It needs to be noted that the rheological properties of the coating may be varied due to evaporation of water, which can further affect the laser focus quality resulting in a low reproducibility (52). To avoid such limitations, the laser beam was integrated into an inverted configuration for fs laser-based cell transfer (see Figure 2.4b and c) and the corresponding specifications of the applied three microscope objectives (Table 2.1).

In order to integrate the time-resolved imaging system to an inverted configuration, two objectives were used for focusing the fs-laser beam through the reservoir bottom (Figure 2.4b and c): a 40× dry objective (Nikon40×/0.6) with a numerical aperture of 0.6 and a 25× water immersion objective (Leica 25×/0.95) with a numerical aperture of 0.95. The cell

distribution at the hydrogel surface can be monitored with the confocal camera CCD2. The transfer process is illuminated with a pulsed 28 ns white-light lamp. Shadowgraph images of the transfer process are obtained with an imaging system comprising a camera (CCD1), a tube lens and a microscope objective (5×/10×). The delay time is triggered by a photodiode and synchronized by a delay generator (see Figure 3.24). To analyze the jet behavior and the cavitation bubble development in the hydrogel, the time-resolved imaging approach, which was described in **chapter** 3.1 for the upright configuration, needs to be carried out again for the inverted setup (see Figure 3.24). The operating scheme is similar to the upright configuration (see Figure 3.1 for details).
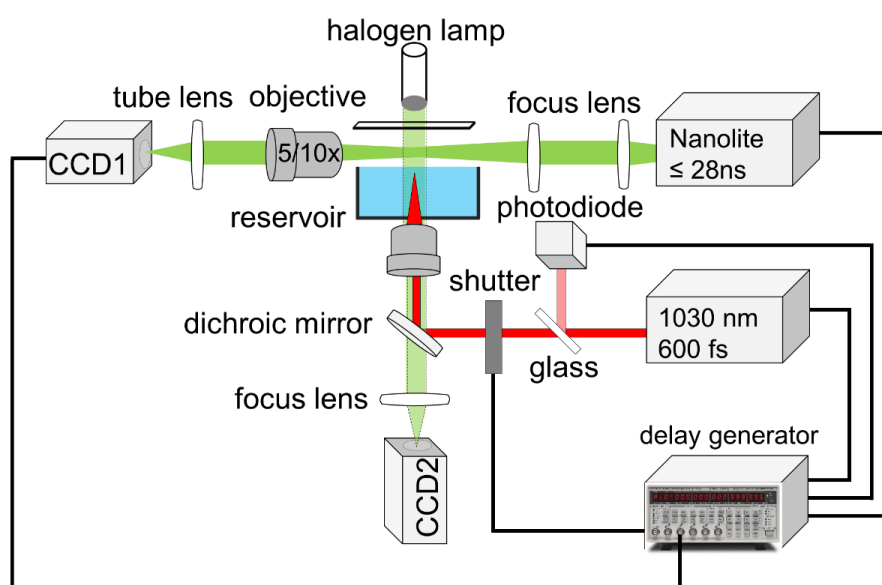

Figure 3.24 Inverted setup for fs laser-based printing of mammalian cells. An fs-laser pulse is focused through a water immersion microscope objective into the reservoir. The cell distribution at the hydrogel surface can be monitored with the confocal CCD2 camera. The transfer process is illuminated with a pulsed 28 ns white-light lamp. Shadowgraph images of the transfer process are obtained with an imaging system comprising a CCD1 camera, a tube lens and a microscope objective (5×/10×). The delay time is triggered by photodiode and synchronized by a delay generator.

3.2.2.1 Pressure wave and cavitation bubble kinetics

The optical breakdown initiated by the fs-pulse in the transparent liquid leads to two mechanical effects: one is the emission of a shock/pressure wave and the other is the creation of a rapidly expanding cavitation bubble (72). To visualize the laser-induced shock/pressure wave and cavitation bubble inside the hydrogel, the white nanosecond spark flash-lamp was used for a time-resolve investigation (see Figure 3.1 and Figure 3.24 for details). However, near to the surface, the cavitation bubble can hardly be detected, due to the reflection of the illumination light by the liquid surface. Thus, the investigation of the laser-induced

shock/pressure wave and cavitation bubble was carried out by focusing the fs-pulse about 1 mm underneath the hydrogel surface. The laser pulse energy was fixed at 2 μJ. Figure 3.25a presents time-resolved images of the pressure wave and cavitation bubble (indicated by red arrows) in the hydrogel by using three different objectives. The pressure wave front can be detected optically due to the change of material density and the optical refractive index and is observed 350 ns after the fs laser pulse has arrived. For the Leica 32× and Nikon 40× microscopy objective the cavitation bubbles are elongated along the optical axis (z-axis) and the corresponding pressure wave fronts are elliptical, due to the spherical aberration caused by the thick hydrogel layer between donor slide and focus (see **chapter** 2.2). For the Leica 25× water immersion objective, on the other hand, the focus seems to be more confined in along the z-axis and both cavitation bubble and pressure wave front are almost circular.

The velocities of pressure waves were determined from the slopes of the pressure wave front versus delay time (see Figure 3.25b). The pressure waves generated by the 32×, 40× and 25× objectives have velocities of 1.52±0.04 km/s, 1.58±0.08 km/s and 1.50±0.02 km/s, respectively, which is similar to the speed of sound in water of 1.489 km/s (72).

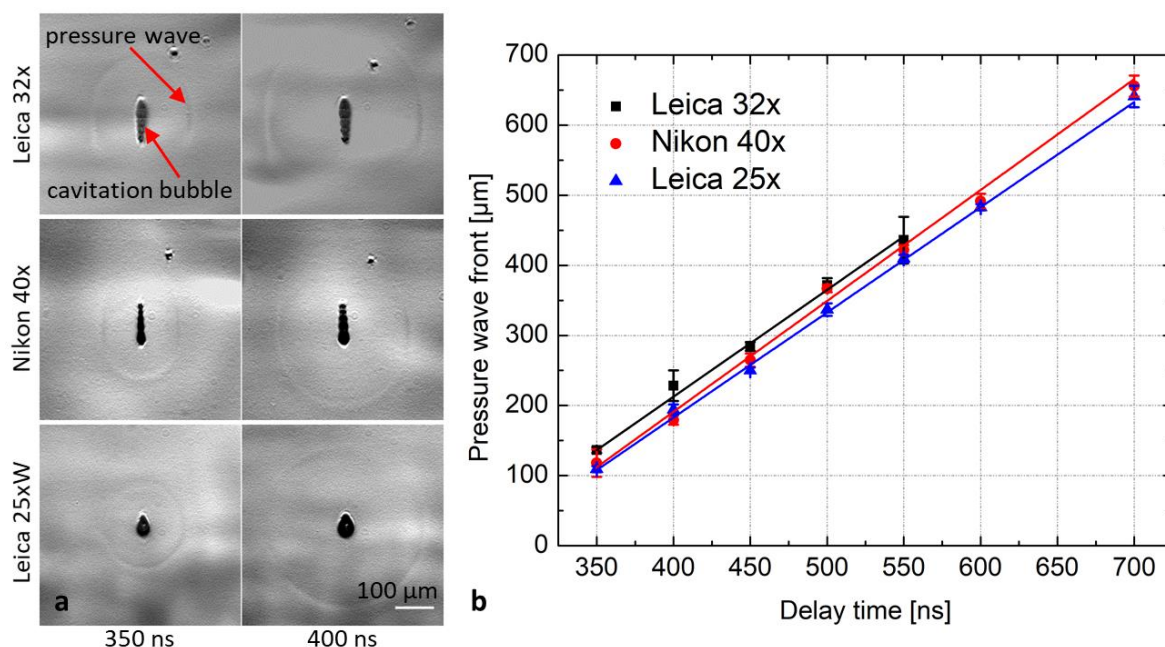Figure 3.25 (a) Representative time-resolved images of the pressure wave and cavitation bubble (3 independent experiments) initiated by focusing 2 μJ fs-pulse with three different objectives in the hydrogel. (b) Plot of the pressure wave front versus delay time. The solid lines are linear fit to the experimental data, which represent average values ± standard deviations of 3 independent experiments.

In this study the focused fs laser pulse provides a high photon density, which leads to a spatially confined optical breakdown with an initial pressure about few GPa (72) and leads to generation of a rapidly expanding cavitation bubble. As the bubble expands against the hydrostatic pressure of the surrounding liquid, the initial pressure rapidly decreases and the energy is eventually dissipated by the displaced hydrogel. Juhasz et al. indicated that the shock wave decays within 10 ns after the fs laser pulse to a harmless sound/pressure wave (72). It should be noted that, a spark flash-lamp with an illumination time of 28 ns was used for the time-resolved study. Thus, the time resolution in this work is not sufficient to record the decay process of the pressure wave.

The cavitation bubble immediately after the transfer laser pulse (300-350 ns) was served as "initial cavitation bubble" in the hydrogel. As mentioned above, for both optical configurations, the fs laser beam was focused into the hydrogel about 1 mm from the surface and the pulse energy was fixed at 2 µJ, in order to instigate the cavitation bubble and pressure wave formation. An elongated initial cavitation bubble with a height of about 100 µm and a width of about 15 µm can be observed in Figure 3.25 when using the Leica 32× for the upright setup and the Nikon 40× for inverted setup, which is in good agreement with the longitudinal spherical aberration LA in Figure 2.5b. When using the Leica 25× water immersion objective, a much more confined initial cavitation bubble can be found with a height of 50 µm and a width of 25 µm. There can be no doubt that these elongated cavitation bubbles generated through the Leica 32× and Nikon 40× objectives occur due to the onset of spherical aberration.

To investigate the effect of microscope objectives on the cavitation bubble expansion in more detail, we conducted a time-resolved study of the cavitation bubble in a delay time range from 300 ns to 30 µs (see Figure 3.26a). The laser pulse energy was fixed at 2 µJ. The cavitation bubbles emerge at a delay time of 300 ns and then start to expand. The plots of the bubble height and width as a function of delay time generated by these objectives can be found in Figure 3.26b-d. The more elongated cavitation bubbles generated by using the Leica 32× and Nikon 40× objectives expand faster in horizontal than in vertical direction and tend to extend to a maximum bubble radius with a nearly spherical shape at a delay time of 5 µs. The "pear"-like shaped cavitation bubble generated by the Leica 25× objective expands almost isotropically and reaches a maximum cavitation bubble radius R_{max} of 85±1 µm at a delay

time of 10 µs (see Figure 3.26c). The cavitation bubbles then start to collapse. A similar behavior has been observed in previous works (71).
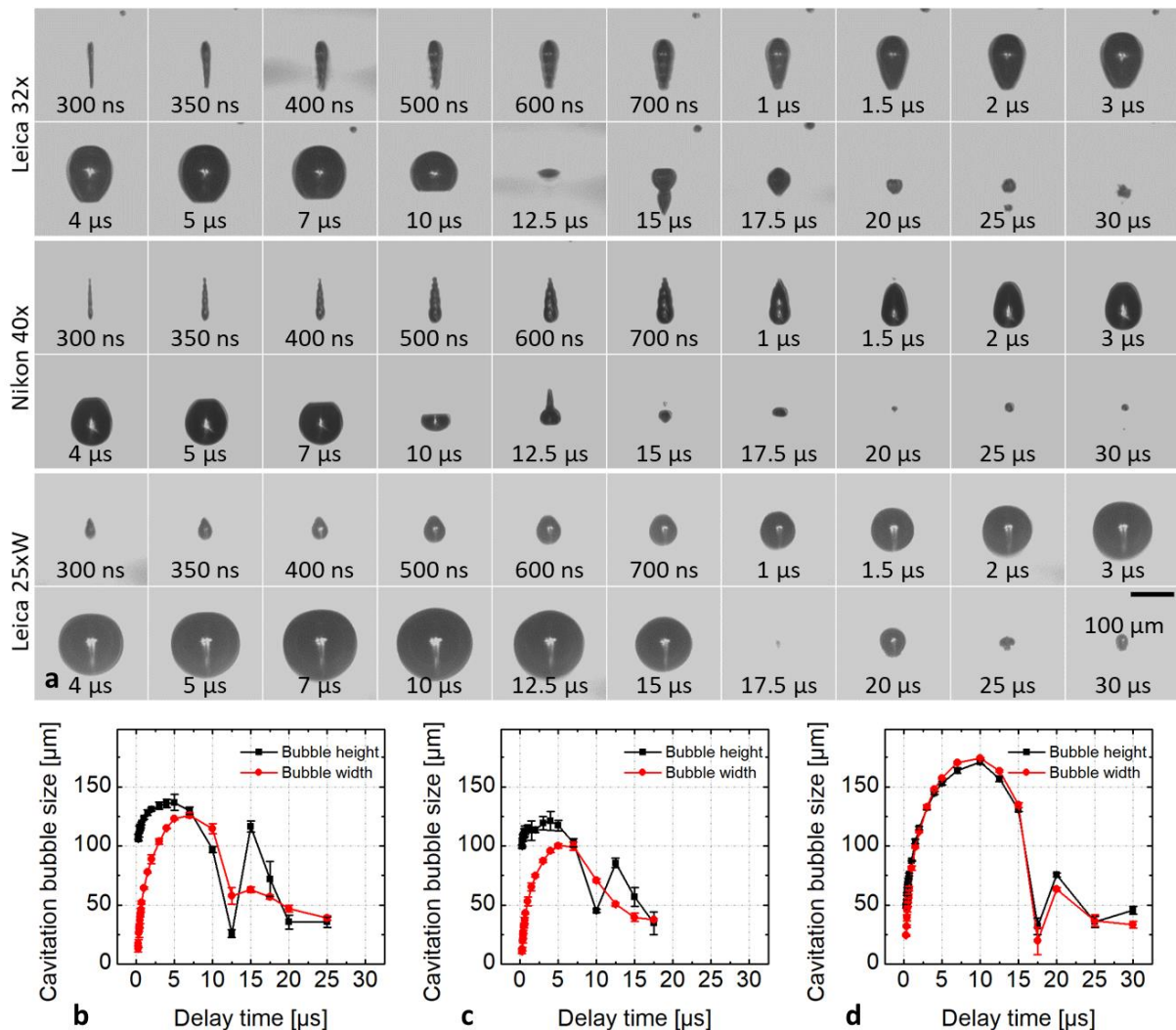
Figure 3.26 (a) Representative time-resolved images of the cavitation bubble (3 independent experiments) initiated by focusing a 2 µJ laser pulse in the hydrogel. Plots of the cavitation bubble height and width generated by the (b) Leica 32× for upright and (b) Nikon 40× as well as (d) Leica 25× for inverted configuration versus delay time. All data points in (b) to (d) represent average values ± standard deviations of 3 independent experiments.

As shown in Figure 2.5b, LA increases linearly with the laser focus length in the hydrogel S_0 (see **chapter** 2.2). For the printing of cell-free hydrogel spots, the spherical aberration for the upright configuration could be ignored when focusing the laser beam 30-80 µm underneath the hydrogel surface. However, as mentioned above, the cavitation bubble near to the surface can hardly be detected. The thickness of the hydrogel in the reservoir is usually about 1 mm, leading to a spherical aberration when using Nikon 40× objective of $LA \approx$ 80 µm. This leads to an elongated laser focus, which may penetrate the suspended cells, leading to cell damage. This objective is therefore not suitable for printing living cells (see

section 3.3.2 for details). Thus, only the cavitation bubble generated through the Leica 25× water immersion objective will be further analyzed.

Figure 3.27a presents images of the obtained maximum cavitation bubbles in the hydrogel at varying laser pulse energies. The corresponding bubble radii in variation of delay time are plotted in Figure 3.27b. The maximum cavitation bubble radius increases with pulse energy as shown in Figure 3.27c. The deposited bubble energy E_B for the mechanical expansion as well as the energy efficiency can be determined by the obtained R_{max} (see equation (6)).
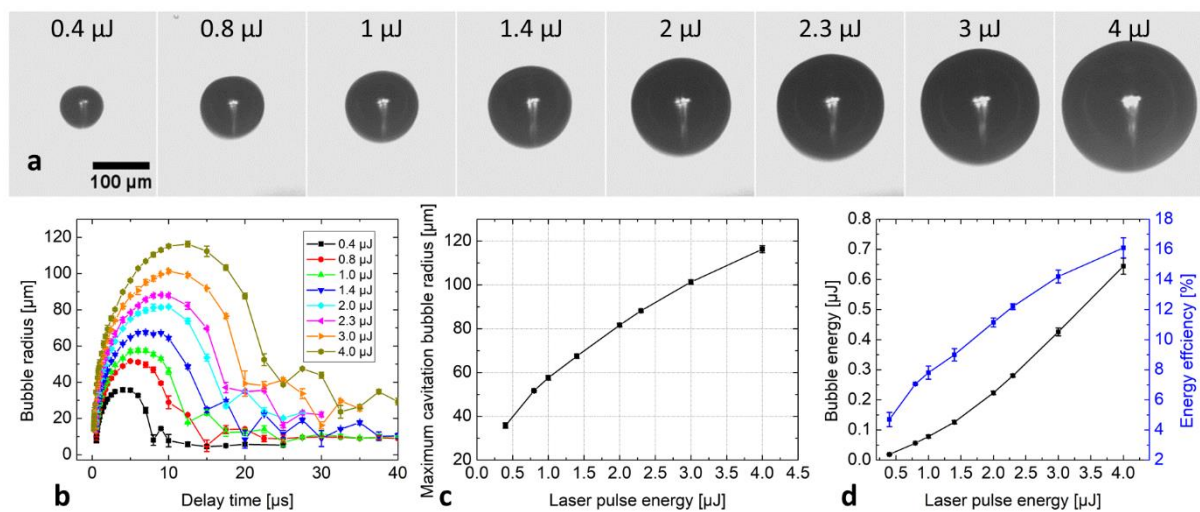
Figure 3.27 (a) Representative time-resolved images of maximum cavitation bubbles (three independent experiments) in the hydrogel generated by the two different objectives and corresponding (b) plots of the maximum cavitation bubble radius (R_{max}) and (c) the calculated bubble energy with varying laser pulse energy from 0.4 to 4 µJ. Scale bar is 100 µm. All data points in (b) to (d) represent average values ± standard deviations of 3 independent experiments.

3.2.2.2 Comparison of jet kinetics

In order to compare the fs laser-induced transfer process through upright and inverted configuration, the time-resolved image of the jet process is presented in Figure 3.28. Here the pulse energy of the fs transfer laser was set to 1.2 µJ and the focus depth to 52 µm. A similar jet development as in the upright setup can be identified, with only one slight difference: At a constant delay time of 10 µs, the first jet has a width of 35±3 µm in the upright configuration and 37±1 µm in the inverted configuration, respectively. Both jets develop straight up with a velocity of about 10 ±1m/s and break up into a primary droplet with a diameter of 32±2 µm for the upright setup and 37±2 µm for the inverted setup at a delay time

62

of 60 μs. Subsequently, both jets propagate at a constant velocity of about 6±1 m/s and reach the acceptor after 120 μs.
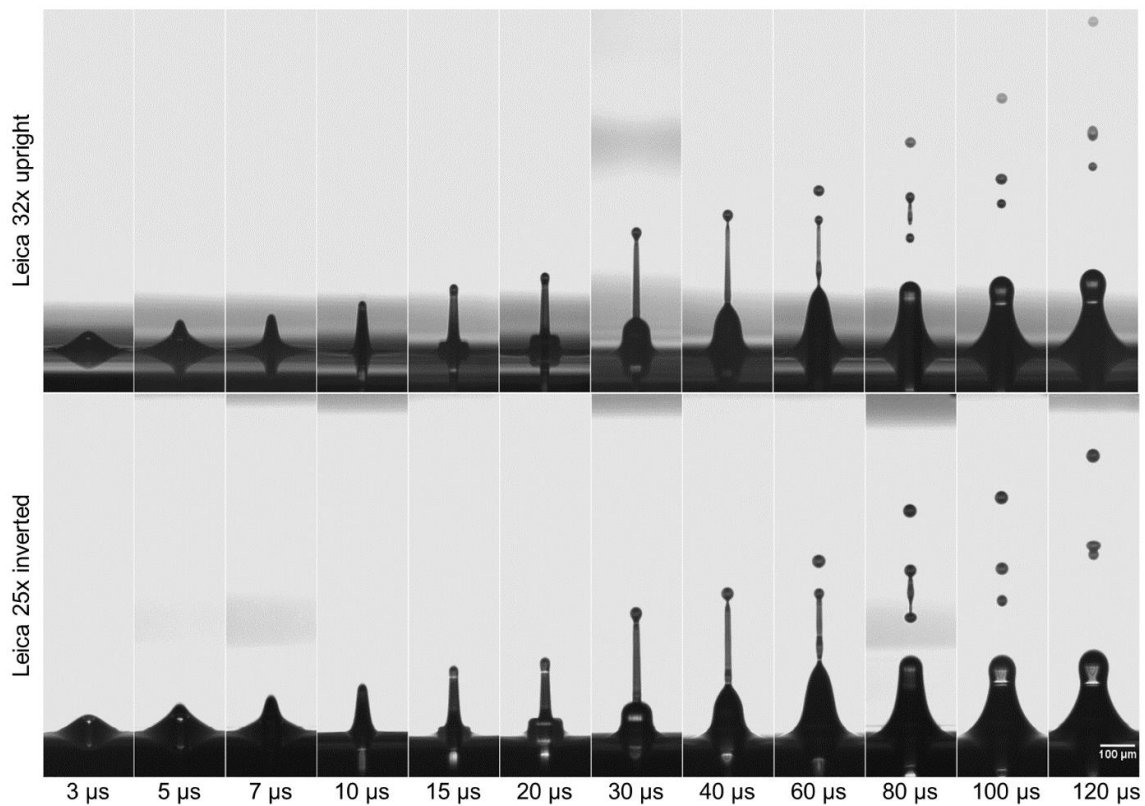
Figure 3.28 Representative time-resolved images of jets by using the Leica 32× for upright setup and the Leica 25× for inverted setup (3 independent jets). The pulse energy of the fs transfer laser was set to 1.2 μJ and the focus depth to 52 μm. Scale bar is 100 μm.

As mentioned above, the best lateral resolution can be obtained by using a minimal pulse energy. Figure 3.29 presents the laser-induced jet process using threshold energies at varied focus depth (objectives for laser focus: Leica 32× for upright configuration, Leica 25× for inverted configuration). In this case, only the primary droplet detaches from the first jet and reaches the acceptor slide. Compared to the transfer process with the upright configuration, an identical threshold pulse energy was used for the transfer with the inverted configuration. As can be seen in Figure 3.28, the primary droplets generated by the inverted configuration are slightly (a few micrometers) larger than the ones generated by the upright configuration. The results are summarized in Table 3.6. The primary droplets develop with similar velocities of about 1.5±0.2 m/s, regardless of the configuration, pulse energies and focus depths. This means that only 4±2 × 10^{-5} of the laser pulse energy are converted into the kinetic energy for the jet propagation.

Figure 3.29 Representative time-resolved image series of jets (3 independent jets) by using threshold pulse energies through the upright and inverted configurations. Scale bar is 100 μm.
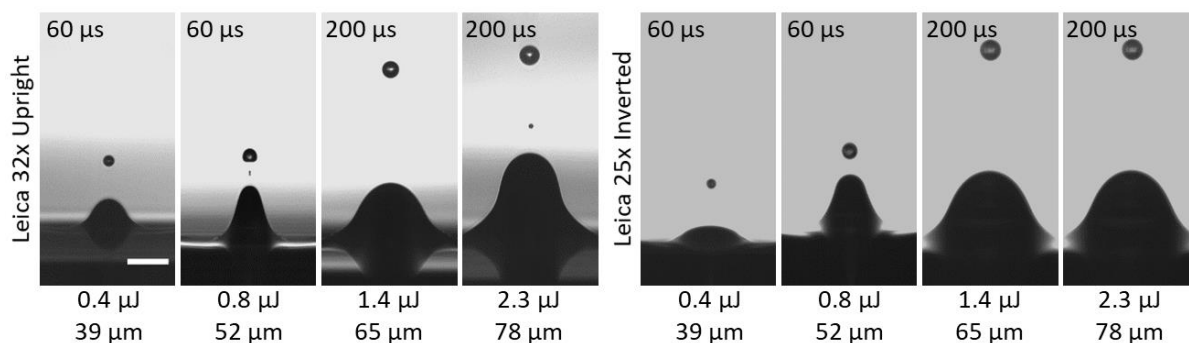
Table 3.6 Summary of the fs laser-induced printing process by using the threshold pulse energies through the upright and inverted configurations and resulting kinetic energies of the primary droplets. All data points represent average values of 3 independent experiments.

Configuration	Leica 32x Upright				Leica 25x Inverted			
Focus depth [μm]	39	52	65	78	39	52	65	78
Threshold energy [μJ]	0.4	0.8	1.4	2.3	0.4	0.8	1.4	2.3
Primary droplet diameter [μm]	28.7	35.4	41.1	48.4	28.7	42.6	51.3	53.3
Primary droplet velocity [m/s]	1.5	1.7	1.3	1.5	1.2	1.5	1.3	1.6
Primary droplet kinetic energy [pJ]	15.9	38.5	34.6	75.6	10.1	49.3	69.1	117
Kinetic energy conversion [10^{-5}]	4.0	4.8	2.5	3.3	2.5	6.2	4.9	5.1

For the cell-free transfer in the upright configuration, where a 32× air objective was used, the spherical aberration caused by diffraction at the air-hydrogel interface could be neglected, because the laser beam was focused only 30-80 μm underneath the hydrogel surface. Compared to the transfer process with the inverted configuration using the Leica 25× water immersion objective, an identical jet behavior and threshold pulse energy for the hydrogel transfer was observed.

3.2.3 Jet dynamics versus pulse duration

As mentioned above, no significant difference between the upright and inverted configuration can be observed. To evaluate the effects of higher pulse durations on the bioprinting process, we investigated jet and cavitation bubble dynamics in the femto- and picosecond regime. A time-resolved study of the jet propagation was carried out by varying the pulse duration from 600 fs to 14.1 ps (see Figure 3.30a). The laser pulse energy was kept constant at 2.0 μJ and the focus depth at 52 μm. These settings allow a stable laminar ejection of hydrogel without splashing for all pulse durations up to 14.1 ps. The jet fronts of the first jet versus the delay time are plotted in Figure 3.30b and the slopes of the fits correspond to the jet velocities, which were obtained from three independent experiments. As the jet

velocity decreases slightly during the propagation, we determined the linear slope v_1 and v_2 as the initial and final velocity before and after 15 µs (see Table 3.7). The initial jet velocity v_1 decreases from 25.6±0.6 m/s for 0.6 ps to 24.0±0.8 m/s for 1.8 ps to 17.5±1.0 m/s for 9.7 ps and to 14.3±1.0 m/s for 14.1 ps. As expected, the jet velocity and the aspect ratio as well as the Weber number decrease with pulse duration (see Table 3.7). As mentioned above, the Weber number describes the ratio of kinetic energy for the propagating jet relative to surface energy. We therefore assume that less kinetic energy can be converted for the jet propagation by using longer pulse duration.
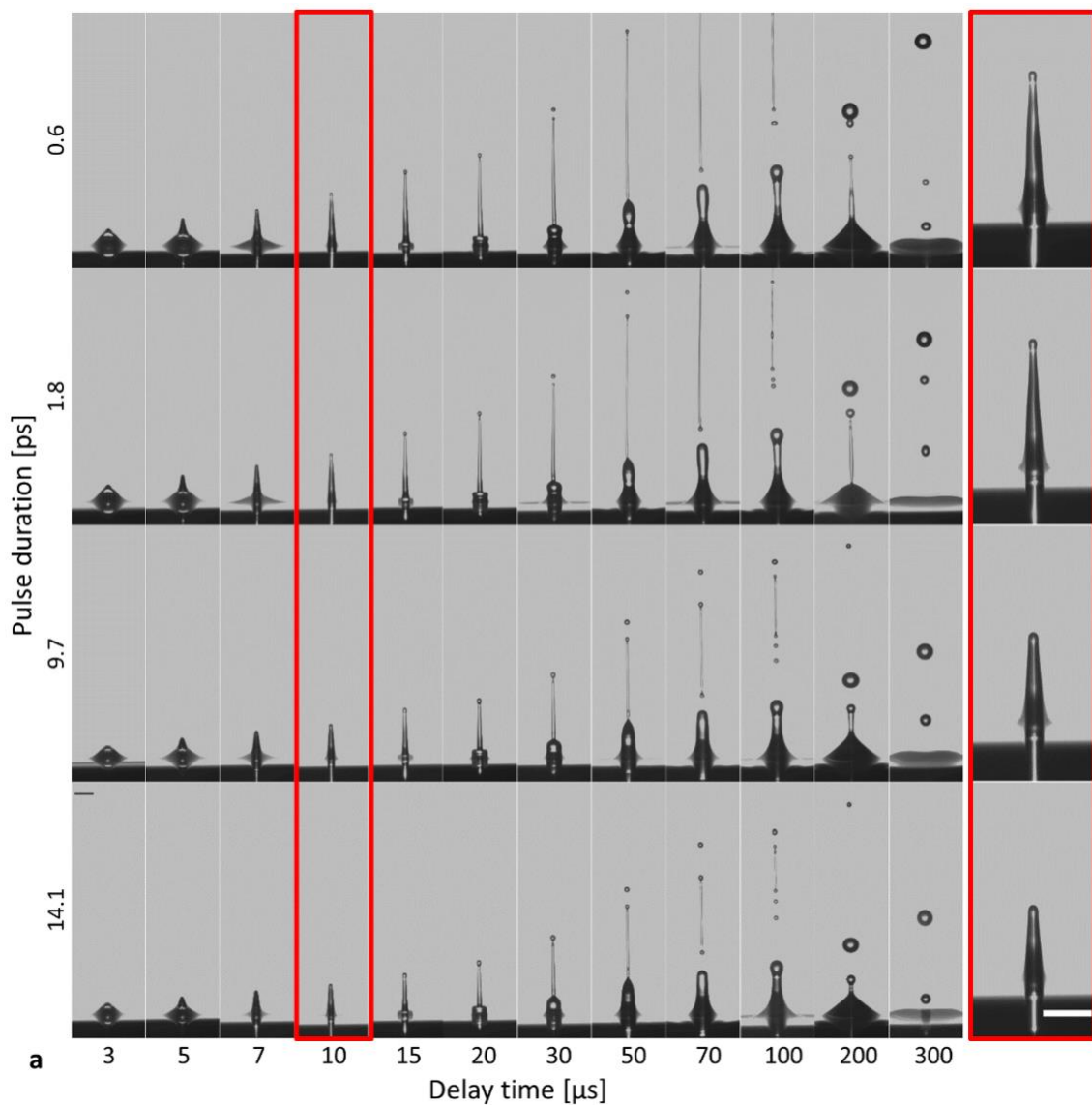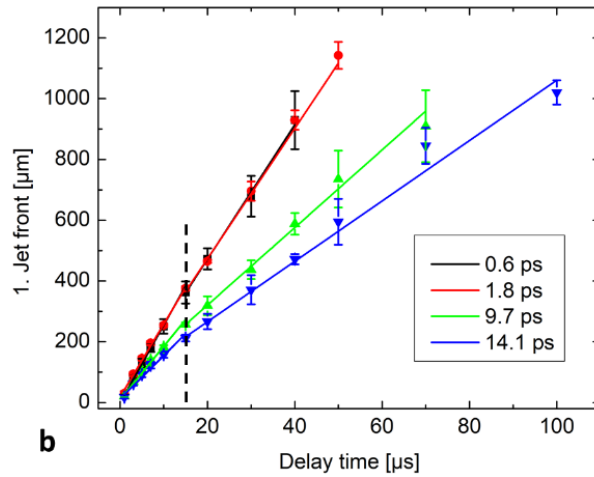
Figure 3.30 Representative time-resolved images of jet process (3 independent jets) indicated with varied laser pulse duration. The laser pulse energy was fixed at 2 µJ and the focus depth at 52 µm. Scale bar is 100 µm. (b) Jet front of the first jet (average value ± standard deviation) versus the delay time at varying laser pulse durations, which were obtained from three independent jets.

Table 3.7 Jet width, aspect ratio, velocity and the Weber number of the first jets in dependency of the laser pulse duration. All data points represent average values ±standard deviations of 3 independent jets.

τ [ps]	d [µm]	Aspect ratio	v_1 [m/s]	v_2 [m/s]	W_e
0.6	29.6±0.4	9.1±0.7	25.6±0.6	22.1±0.7	291±22
1.8	28.4±0.3	8.9±0.1	24.0±0.8	21.5±1.1	230±21
9.7	28.5±0.5	6.5±0.4	17.5±1.0	12.8±0.4	131±16
14.1	29.5±1.1	5.4±0.2	14.3±1.0	10.8±0.3	90±13

To determine the bubble energy conversion depending on the pulse durations, a time-resolved cavitation bubble study was carried out by focusing a 2 µJ pulse at a focus depth of about 1 mm (see Figure 3.31a @ 600 fs). The cavitation bubble expands isotropically and achieves its maximum radius R_{max} of 85±1 µm at a delay time of about 10 µs. Subsequently, the bubble collapses and expands again. The developments of the cavitation bubbles generated by the 1.8, 9.7 and 14.1 ps laser pulses are similar to that generated by the 0.6 ps pulse (data not shown). The plots of the bubble radius in variation of delay time for the different laser pulse durations can be found in Figure 3.31b-e. The maximum cavitation bubble radius R_{max} in the hydrogel decreases slightly from 84.2±1.2 µm for 0.6 ps to 81.1±2.3 µm for 1.8 ps, to 75.3±2.3 µm for 9.7 ps and to 71.3±2.2 µm for 14.1 ps pulse duration, respectively (see Figure 3.31f). The bubble energy decreases with pulse duration as shown in Figure 3.31g. By dividing the bubble energy by the incident laser pulse energy the conversion efficiency can be determined, which drops from about 12.5% at 600 fs to 7.5% at 14.1 ps pulse duration.
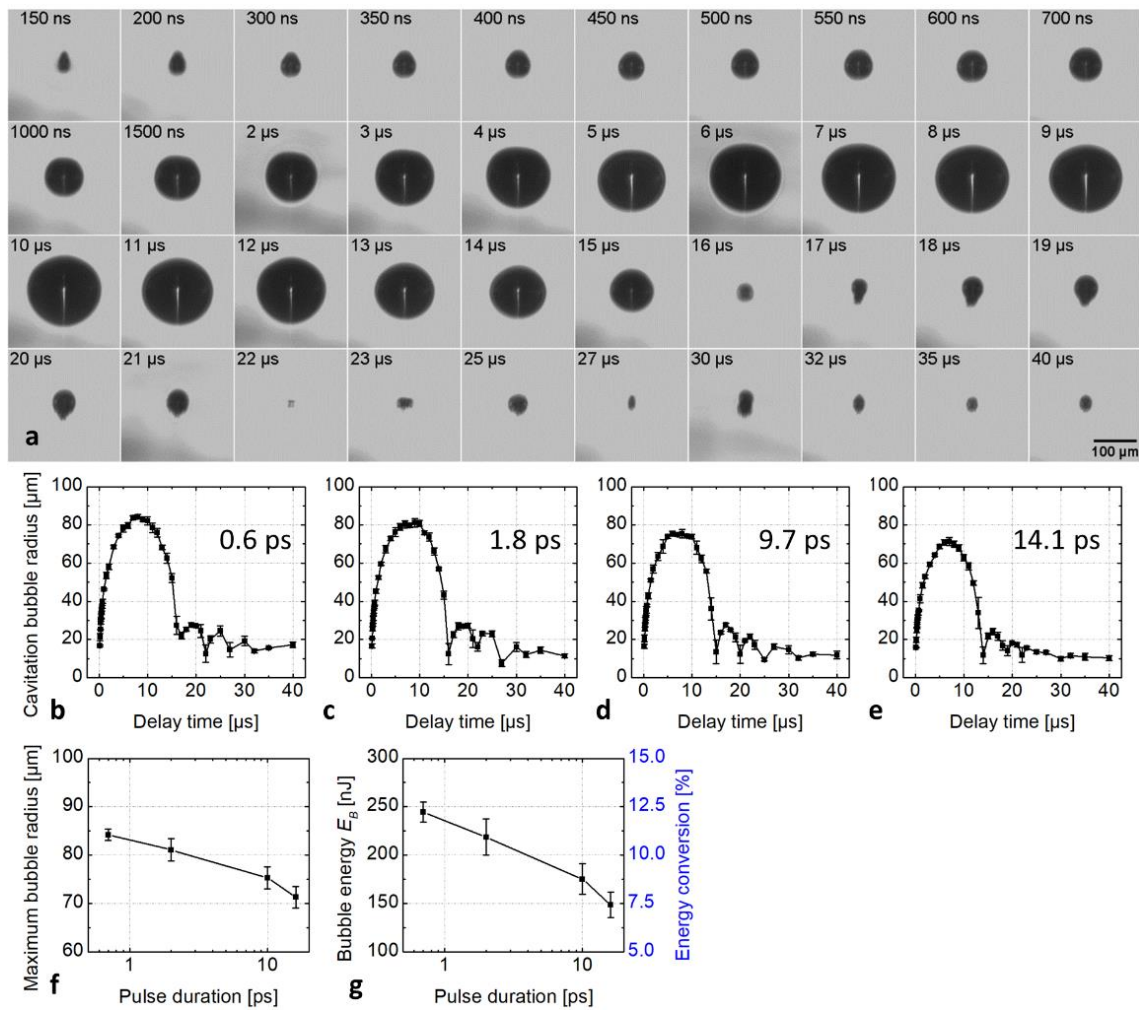
Figure 3.31 (a) Representative time-resolved images of the cavitation bubble (3 independent experiments) initiated by using a laser pulse with a pulse duration of 0.6 ps. The laser pulse energy was fixed at 2.0 μJ and the focus depth at 1 mm. (b-e) Plots of the cavitation bubble radius, (f) the obtained maximum cavitation bubble radius R_{max} and (g) the bubble energy and the corresponding energy conversion efficiency in a variation of pulse duration. All data points in (b) to (g) represent average values ± standard deviations of 3 independent experiments.

3.3 Investigation of cell viability after laser-induced transfer

The transfer process including the generation of the optical breakdown, pressure wave and cavitation bubble expansion in the hydrogel and the resulting the jet propagation have been systematically analyzed. High survival rates and good cell viability after transfer are key parameters for biofabrication techniques in tissue engineering. Therefore, in this section a systematic analysis of how the cell viability and how it is affected by the applied parameters including the jet kinetics, the laser focus shape, the pulse energy, the focus depth, the pulse duration is performed. Details of the live-dead assays based on propidium iodide staining of transferred cells as well as negative and positive controls can be found in the **chapter** 2.4.5 and Statistical Methods in **chapter** 2.5.

3.3.1 Effect of the jet propagation on cell viability

As mentioned above, by increasing the laser pulse energies or decreasing focus depths, an abrupt increase of the transferred hydrogel spot diameter on the acceptor slide can be observed due to the transfer of the second jet (refer to section 3.1.3). We therefore assume that ~80 μm spots are indeed the result of the first fast-moving jet, while the larger ~200 μm spots result from both, the first and second jet. The second jet ejects droplets at a velocity which is 15 - 20 times smaller than the first jet. In the large spots, the cell survival rate is about 91%, while in the small irregular spots the survival rate is only about 50% (Table 3.1). If the impact at the acceptor surface is indeed the main source of cell damage, this could explain the higher viability observed in the larger hydrogel spots (see Figure 3.2). In addition to the reduced deceleration forces because of the lower droplet velocities, the larger droplets can also cushion the impact more effectively than smaller droplets. Furthermore, acceleration and shear forces during jet generation and expansion would be reduced for the wider and more slowly moving second jet.

3.3.2 Effect of the focus shape on cell viability

To investigate the effect of the focus shape (i.e. spherical aberration) on the cell viability, three different objectives were used for printing living cells. The specifications of all three objectives can be found in Table 2.1. Figure 3.32 presents the initial cavitation bubble generated through the three different microscope objectives. Here the pulse energy was fixed at 2 μJ. The position of the maximum bubble width can be assumed as the laser focus. For

printing living cells, the cells were usually suspended above the laser focus, at a distance of 40-80 μm (in Figure 3.32 a distance of 50 μm is indicated by greed dots). It needs to be pointed out, that at a delay time of 300 ns, the surrounding hydrogel shows almost no displacement, thus cells should remain stationary at the surface. When using the Leica 32× for the upright optical configuration and the Nikon 40× for the inverted optical configuration, the laser focus is located at the upper and bottom of the elongated initial cavitation bubble, respectively. This elongation of the cavitation bubble can be significantly reduced by using a water immersion objective, such as the Leica 25×. The initial cavitation bubble generated by the Nikon 40× objective has a much greater height and penetrates the suspended cells above the focus, leading to cell damage (survival rate less than 40% regardless of pulse energy and focus depth, data not shown). In contrast, the initial cavitation bubbles generated by the Leica 32× objective in the upright setup and the Leica 25× water immersion objective in the inverted setup have no direct overlap with the suspended cells, resulting above 95% cell viability (**chapter** 3.3.5). Our results demonstrate that only the Leica 25× water immersion objective can be integrated in an inverted microscope setup for printing of living cells.

Leica 32x upright   Leica 25x inverted   Nikon 40x inverted
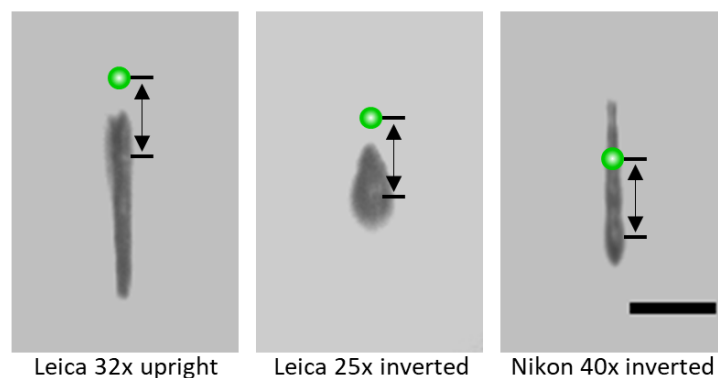
Figure 3.32 Representative images of initial cavitation bubbles from 3 independent experiments in the hydrogel generated by three different microscope objectives (see Table 2.1) by focusing a fs-pulse with 2 μJ. Green dots indicate the suspended living cells is a distance of 50 μm. Scale bar is 50 μm.

3.3.3 Effect of laser pulse energy and focus depth on cell viability

To investigate the effect of laser pulse energy and focus depth on cell viability, living cells were printed through the Leica 25× water immersion objective in an inverted microscope setup in the variation of the laser pulse energies and focus depths. After the transfer, the acceptor surface was incubated for 15 min to allow PI staining. Figure 3.33 shows suspended TCP1 cells in reservoir before printing (upper panel) and the transferred cells on the gelatin coated acceptor slide after printing (middle and bottom panel). "*To determine the cell viability, cells were stained with PI in the cell reservoir prior to the laser transfer and on the acceptor*

slide after the laser transfer. Dead cells appear in red. In the cell reservoir, only living cells were selected and transferred to the acceptor slide and all cells survived the printing process (middle panel). PI staining prior to transfer thus served as a built-in negative control for the cell viability analysis. In the middle panel, the focus of the transfer laser (2 µJ) was set 52 µm below the cells, resulting in 100% viable cells after transfer in this example (no red cells after transfer). To ensure the effectiveness of PI staining, cells were also deliberately killed during the transfer process, by setting the laser focus to only 35 µm below the cells in a positive control experiment (lower panel). Thirteen out of fifteen cells showed red fluorescence indicating cell death after the laser transfer (bottom, right)". The text is obtained from the article (22). As shown in Figure 3.32, the height of the initial cavitation bubble above the laser focus is about 37 µm, which is larger than the distance of 35 µm between the cells and laser focus. Thus, in this case the living cells are too close to the generated cavitation bubble, which induces cell damage. Interestingly, by using a slightly higher focus depth of 39 µm, while keeping the laser pulse energy fixed at 2 µJ, 83% of the transferred cells were surviving on the acceptor.

To systematically analyze the effect of the initial cavitation bubble on the cell viability, these experiments for cell viability with serval pulse energies and focus depths were repeated. The results are displayed together with the height of the initial cavitation bubble in Figure 3.34. The jet velocities and cell survival rates are summarized in Table 3.8. The black solid line in Figure 3.34 indicates the height of the initial cavitation bubble above the laser focus. When living cells are located away from the cavitation bubble, almost all of the transferred cells survived after transfer. These results provide complete evidence that cells can easily be damaged when they are close to the cavitation bubble or even are in contact with the initial bubble (red area in Figure 3.34 can be regarded as deadly zone).
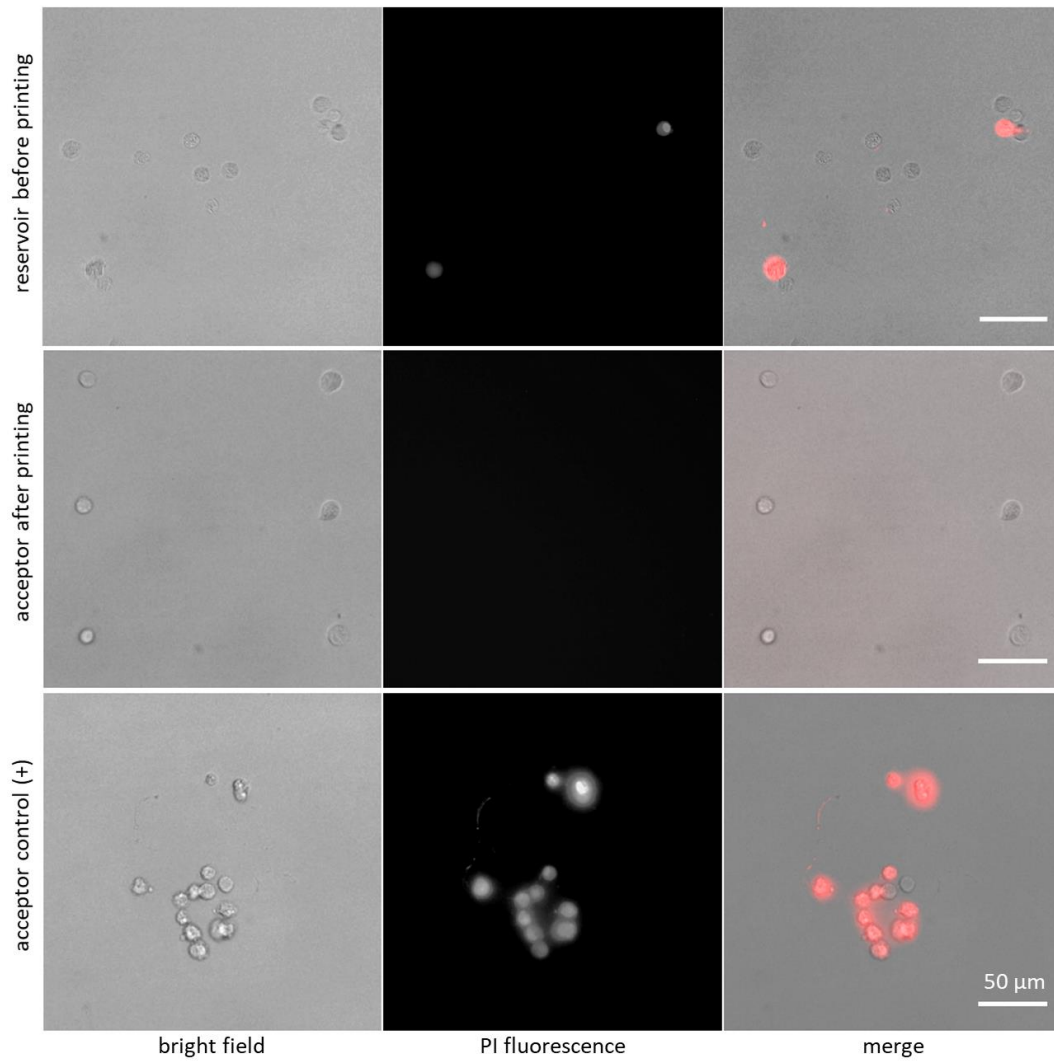
Figure 3.33 Representative microscopy images of suspended TPC1 cells within the reservoir before printing (upper panel) and of the transferred cells on the gelatin coated acceptor slide after printing (middle and bottom panel). Dead cells are displayed in red, living cells stay unstained. In the middle panel, the focus of the transfer laser was set 52 µm below the cells, resulting in 100% viable cells after transfer in this example (no red cells after transfer). To ensure the effectiveness of PI staining, cells were deliberately killed during the transfer process, by setting the laser focus to only 35 µm below the cells in a positive control experiment (lower panel). The figure has been published in article (22). Representative figure from at least 10 independent experiments.
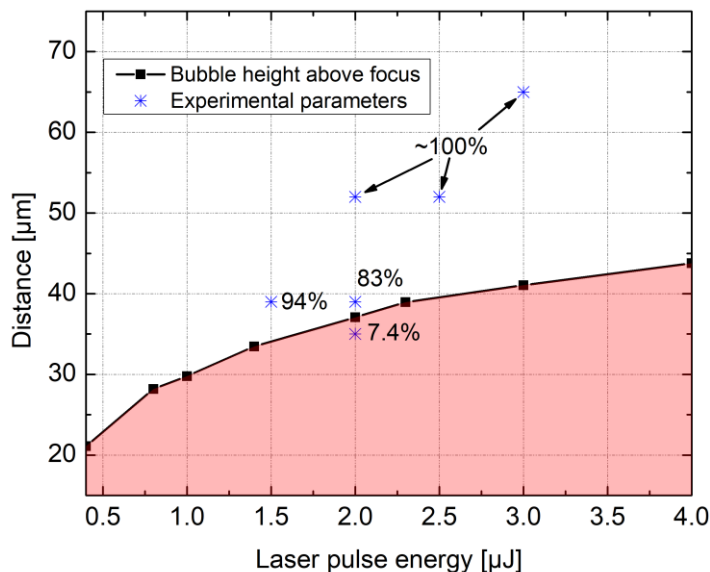
Figure 3.34 correlation between the initial cavitation bubble and the cell survival rate with serval printing parameters resulting in different cell survival rates (*). The number of transferred cells is presented in Table 3.8. Solid line indicates the initial cavitation bubble above laser focus.

Table 3.8 Cell survival rate by using our laser-based bio-printing method with serval printing parameters including pulse energy and focus depth. The jet velocity (average values ± standard deviations) was obtained from 3 independent jets.

Pulse energy [μJ]	Focus depth [μm]	Velocity [m/s]	Transferred cells	Live cells	Survival rate
1.5	39	42±1	18	17	94%
2	35	> 50	27	2	7.4%
2	39	45±1	18	15	83%
2	52	24±1	81	80	99%
2.5	52	21±1	18	18	100%
3	65	19±1	18	19	100%

3.3.4 Effect of laser pulse duration on cell viability

To prove that it is indeed possible to transfer single cells by varying the laser pulse duration from 0.6 to 14 ps, the pulses were coupled into the inverted setup equipped with an incubation chamber. In order to investigate the cell viability, only living cells were selected and transferred to the gelatin coated acceptor surface. Table 3.9 shows the amount of total transferred and viable hMSCs (SCP1 cell line) after the transfer using the same laser parameters as in Figure 3.30. Almost all printed cells survived after the transfer and a cell survival rate of at least 98.6% can be obtained for all pulse durations in the range from 0.6 to 14.1 ps.

Table 3.9 Cell survival rate of printed hMSCs on Gelatin coating with varying pulse duration

Pulse duration [ps]	0.6	1.8	9.7	14.1
Transferred cells	18	21	17	17
Viable cells	18	20	17	17

3.3.5 Maximizing cell viability by using optimized parameters

The cell viability varied depending on cell type and applied substrate due to the impact during landing on the acceptor. The results of this work provide evidence that a minimal pulse energy (i.e. slightly above the threshold energy) should be used to reduce cell damaging effects when printing living cells. Live-dead assays of transferred cells, as well as many of the time-lapse experiments (cf. Figure 3.40 and Figure 3.41) confirmed, that with film-free fs-laser based bioprinting a cell survival rate of 92.7%±0.9% (mean value and standard error of an experiment with 165 cells from 15 independent experiments) can be obtained for hTSCP cells transferred to a collagen coated target substrate (Table 3.10). For B16F1 cells transferred to a Matrigel coated substrate, a survival rate of 96.5%±0.7% was obtained (134 cells from 13 independent experiments in Table 3.11), and for human papillary thyroid carcinoma cells (TPC1) transferred to a gelatin coated substrate, a survival rate of 98.5%±0.4% was obtained (64 cells from 6 independent experiments in Table 3.12).

Table 3.10 Cell viability of printed single hTSPC cell on Collagen coating

Live	8	8	5	10	10	8	10	11	9	12	6	21	6	20	8
Dead	0	0	0	0	0	2	0	0	5	1	0	0	0	4	1

Table 3.11 Cell viability of printed single B16F1 cell on Matrigel coating

Live	8	9	8	7	9	8	8	7	10	10	15	14	10
Dead	1	0	1	1	0	1	1	3	0	0	0	1	2

Table 3.12 Cell viability of printed single TCP1 cell on Gelatin coating

Live	11	12	6	10	12	13
Dead	1	0	0	0	0	0

3.4 Applications of fs laser-based printing

3.4.1 Bioprinting of different cell sizes and non-biological particles

To prove the ability to transfer single cells with different cell size were used, murine 3T3 fibroblast cells have an average diameter of 24±5 µm and murine B16F1 cells have an average diameter of 15±3 µm were used. The pulse energy was fixed at 2 µJ and the focus depth at 52 µm. Transfer of pure hydrogel was used as a control (Figure 3.35a first row, indicated with red crosses). The middle column shows the respective reservoir position after laser transfer and proves that the selected cell was removed from the reservoir. Pure hydrogel and cell-laden hydrogel containing a single cell can be found on the acceptor slide in the last column. Compared to the irregular shapes of the cell-containing spots on the acceptor, the cell-free spot is circular and uniform with a diameter 100±5 µm. Figure 3.35b presents the corresponding time-resolved images of the transfer process. Compared to the straight cell-free jet, clearly visible droplets occur at each tip of the cell-containing jet after 3 µs (indicated with red arrows) with a diameter of about 23±6 µm for the smaller B16F1 and of 32±4 µm for the larger 3T3 fibroblasts cells, respectively. The droplet diameters on the jet tips are slightly larger (30%) than the size of the printed single cells.
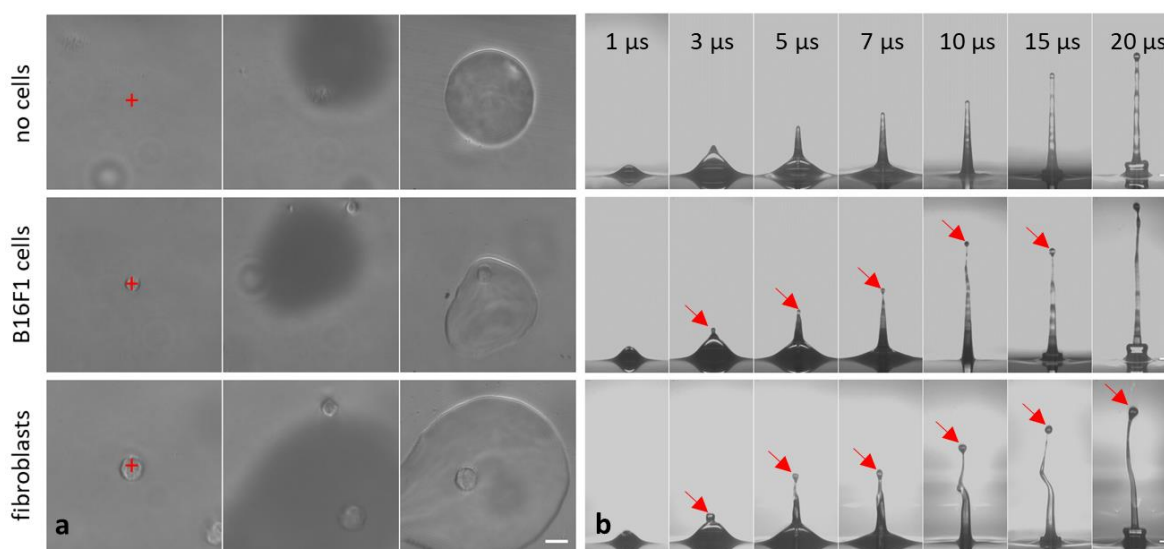
Figure 3.35 (a) Representative bright field images of the cell suspended at the hydrogel surface before and after printing, and the transferred cells on the acceptor slide (21 independent transfers). Parameters were 2 µJ pulse energy and 52 µm focus depth. Pure hydrogel, smaller B16F1 cells (diameter 15±3 µm) and larger 3T3 fibroblast cells (diameter 24±5 µm) were transferred. (b) The representative corresponding time-resolved images of the transfer process from 3 independent jets. Scale bar is 50 µm.

To analyze the effect of the non-biological particles on the jet behavior: polystyrene beads (microspheres made from monodisperse polystyrene, Polysciences, Inc.), with a diameter of 10 and 20 μm were used. These beads have a similar mass density as living cells and float at the hydrogel surface. The pulse energy of the fs-laser was set to 2 μJ and the focus depth to 52 μm. In Figure 3.36, the left four columns, presents time-resolved images of the transfer process with single beads being transferred. The microspheres are recognizable at the tip of the first jet at each delay time. The microspheres propagate faster than the first jet, breaking up from the jet after 5 μs. The small microspheres resulting from the transfer of 10 μm-beads have an average diameter of 11.2±1.3 μm (n=21) and the large microspheres (20 μm beads) have an average diameter of 21.4±1.7 μm (n=42), both slightly larger than the corresponding size of the beads. Figure 3.36, large image in the right column, presents a propagating jet containing several beads with 2 different diameters. It must be pointed out that the beads hardly remain stationary at hydrogel surface and have an initial horizontal velocity in the reservoir before printing, which leads to a curved jet.
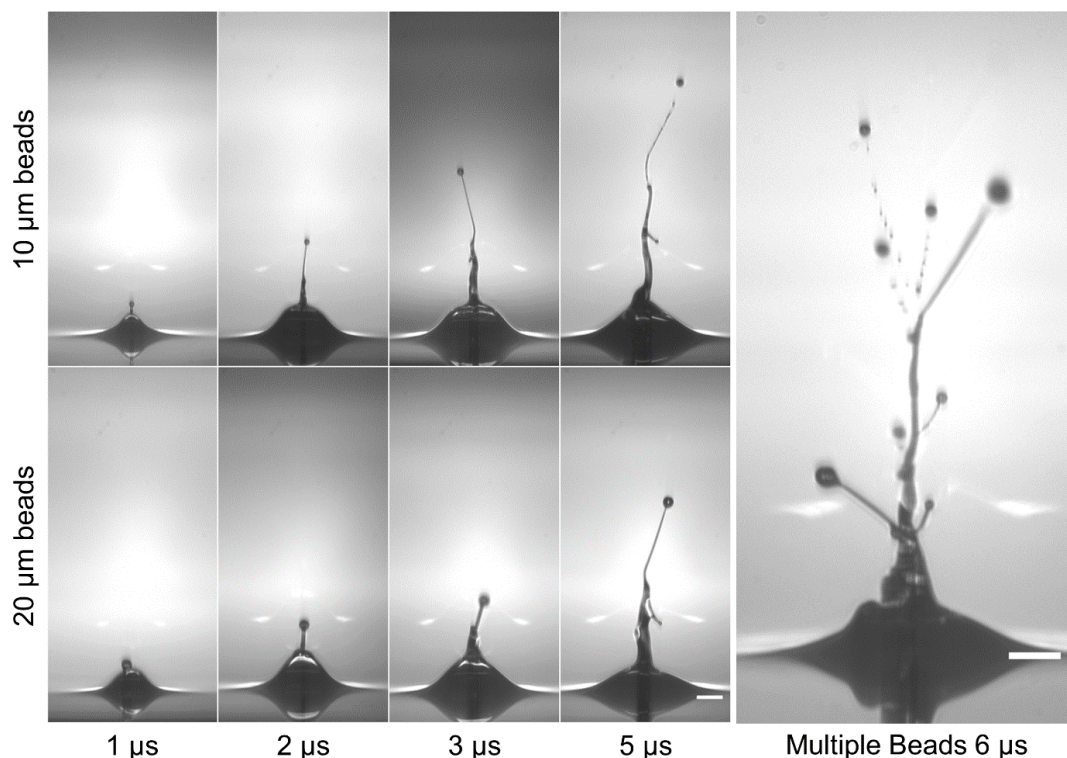
Figure 3.36 Representative time-resolved images of laser-induced transfer of polystyrene beads with a diameter of 10 and 20 μm from 3 independent experiments, respectively. Right column shows the transfer of multiple beads with mixed diameters 10 and 20 μm. Scale bar is 50 μm.

3.4.2 Creating custom-made 2D patterns

By moving the acceptor slide in x-y direction, almost any desired 2D pattern can be realized upon request. Figure 3.37 shows a reproduction of the "Canter"-Logo (bright field microscopy image) produced by the exact, programmable positioning of individual spots (diameter: 70±3 μm). To prove the ability of precisely printing predesigned 2D patterns with livings cells we printed GFP-labeled SCP1 cells with a cell-cell distance of 100 μm drawing the letters of "LHM", which is an abbreviation of "Laserzentrum Hochschule München". As can be seen in Figure 3.38, most of the printed cells are positioned with an accuracy of about 10-20 μm, which is close to the cell diameter of 20 μm.
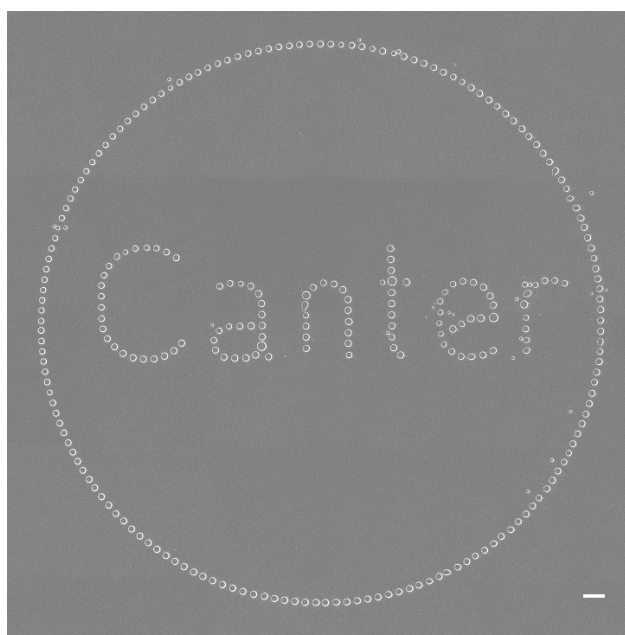
Figure 3.37 Representative bright field image of transferred cell-free hydrogel spots in a 2D pattern at acceptor slide. Scale bar is 200 μm.

Figure 3.38 Representative fluorescence microscope image of a 2D pre-designed pattern of individual GFP-labeled SCP1 cells with a cell-cell distance of 100 μm.

76

"To investigate the single cell positioning accuracy, hMSCs were also printed on a gelatin coated substrate with predefined intercell distances of 50, 100 and 200 µm. As can be seen in Figure 3.39 most cells deviate less than one cell diameter ($\approx$14-32 µm fo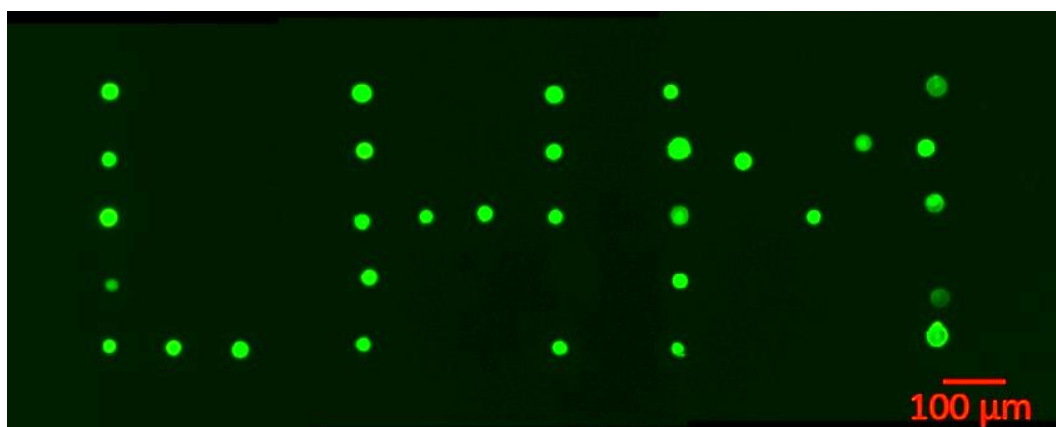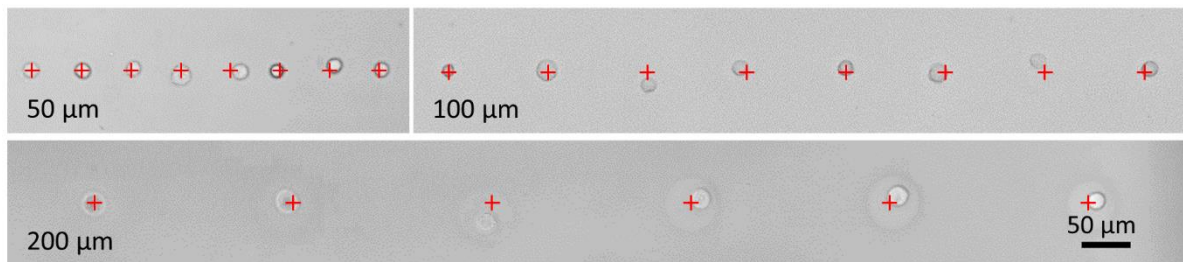r the hMSCS used here) from their target positions, indicated by red crosses (cross size: 15 × 15 µm)". The text is obtained from the article (22).

Figure 3.39 1D positioning of cells (hMSCs) in rows with defined cell-cell distances. Red crossed indicated nominal target positions. The figure has been published in article (22). Representative figure from at least 10 independent experiments.

"To investigate the cell viability of human primary cells after the transfer and as an example of using single cell printing to study cell–cell interactions, we printed hTSPCs on a collagen-coated substrate and carried out time-lapse video microscopy for 66 h after printing. Figure 3.40 shows three rows of hTSPCs printed with intercell spacing of 50, 100, and 200 µm. After 5 and 10 h, the hTSPCs with 50 and 100 µm intercell spacing start to polarize and elongate toward neighboring cells, while the 200 µm separated cells remain isolated and are seemingly unaffected by their neighbors. This indicates paracrine and/or substrate mediated mechanical communication between the cells, stimulating cell elongation at intercell distances of 50 and 100 µm, while at larger intercell spacing, the biochemical and/or mechanical signals do not reach the neighboring cells. After 20 h and more, cells with an initial intercell spacing of 100 and 200 µm start migrating away from each other, while the 50 µm spaced cells still remain in close proximity to each other and partially maintain physical cell–cell contacts, only to disengage at later time points. This is most likely due to the lack of external guidance by the ECM. It should be pointed out, that even 66 h after the cell transfer, all hTSPCs were still migrating, indicating a cell-survival rate of 100% in this experiment". The text is obtained from the article (22).
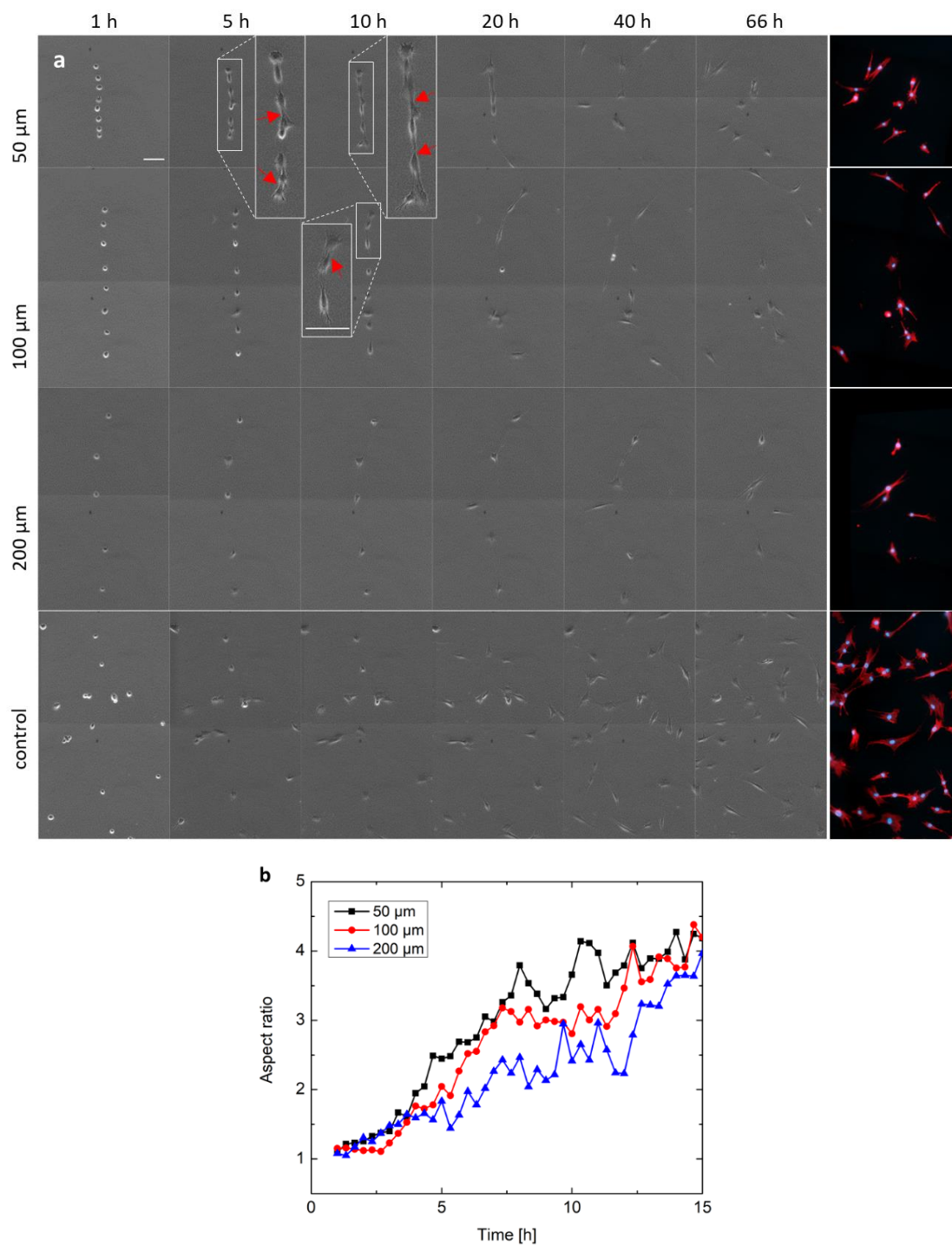
Figure 3.40 (a) Representative time lapse microscopy and fluorescence imaging from 1 experiment to monitor cell spreading and migration of human tendon stem/progenitor cells (hTSPCs) transferred to collagen coated acceptor surfaces. Cells were printed in vertical lines with a defined cell-to-cell distance of 50 µm (upper panel), 100 µm (middle panel) and 200 µm (lower panel). Close-ups highlight the elongated cells after 5h and 10h, cell-cell contacts are indicated with red arrows. As a negative control, hTSPCs were also manually pipetted onto a collagen substrate and cultivated under identical conditions for 66 hours. After phalloidin (red) and DAPI (blue) staining, the actin cytoskeleton of the hTSPCs (66 hours) is displayed in red and the nucleus in blue (right column). Scale bars = 100 µm (images and close-ups). (b) Cell polarization (aspect ratio) versus time for 50, 100, and 200 µm inter-cell spacing. The figure has been published in article (22).

Another example showing how paracrine cell signaling depends on intercellular distances is given in Figure 3.41, the cells were printed in two lines with varying horizontal cell-cell distances, beginning with 24 μm (top row) up to 219 μm (bottom row). The vertical distance was kept constant at ~200 μm. The acceptor surface was coated with Matrigel. After 3 hours, the cells with 24 μm inter cell distance started to migrate towards each other and establish contact. After 19 hours, the cells with 84 μm inter cell distance formed contact with each other and immediately afterwards established contact with the cells with an initial inter cell spacing of 24 μm. Finally, after 35 hours, the cells with 131 μm inter cell spacing established contact, while the cells at 177 and 219 μm inter cell spacing remained separated for more than 40 hours.
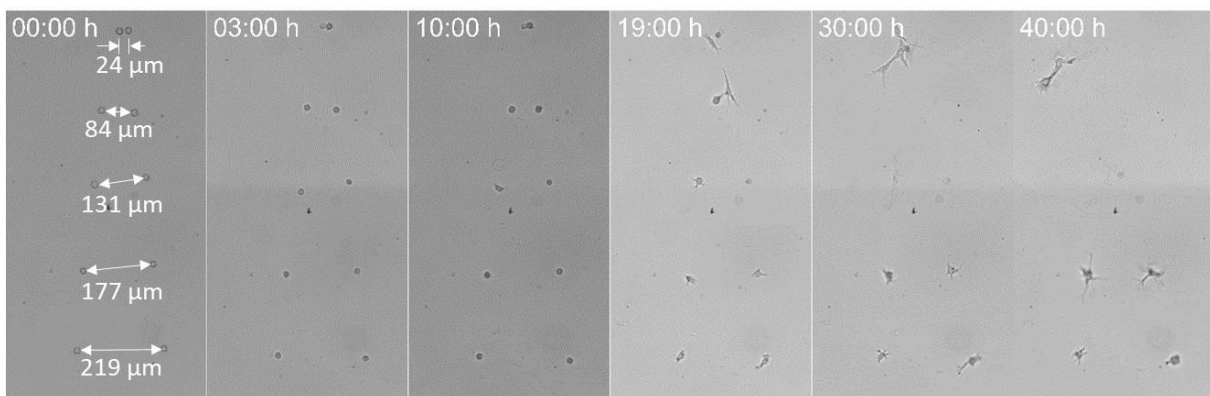
Figure 3.41 Representative time-lapse microscopy images monitoring mouse melanoma (B16F1) cell spreading and migration from 4 independent experiments. Scale bar is 100 μm.

3.4.3 Isolating and sorting genetically modified single cells

"In order to test whether genetically modified cells can be selected based on a fluorescence marker, which is co-expressed with the gene of interest, NHI 3T3 cells were bioprinted. The cells were transfected with the plasmid pCMV-LifeAct-TagRFP (Ibidi, Germany) via lipofection. However, the transfection efficiency was only around 20%. Successfully transfected cells can be identified by red fluorescence as shown in Figure 3.42a. In the reservoir, transfected (fluorescent) and non-transfected (non-fluorescent) cells were distributed randomly. By using the inverted laser based single cell transfer set up, fluorescent cells can be separated from non-fluorescent cells and lined up separately on the acceptor slide (see Figure 3.42b). Transfected cells can be arranged according to their fluorescence intensities (Figure 3.42c). Cells with bright fluorescence were positioned in the top row, those with only weak fluorescence in the middle row and non-fluorescent cells in the bottom row". The text is obtained from the article (22).
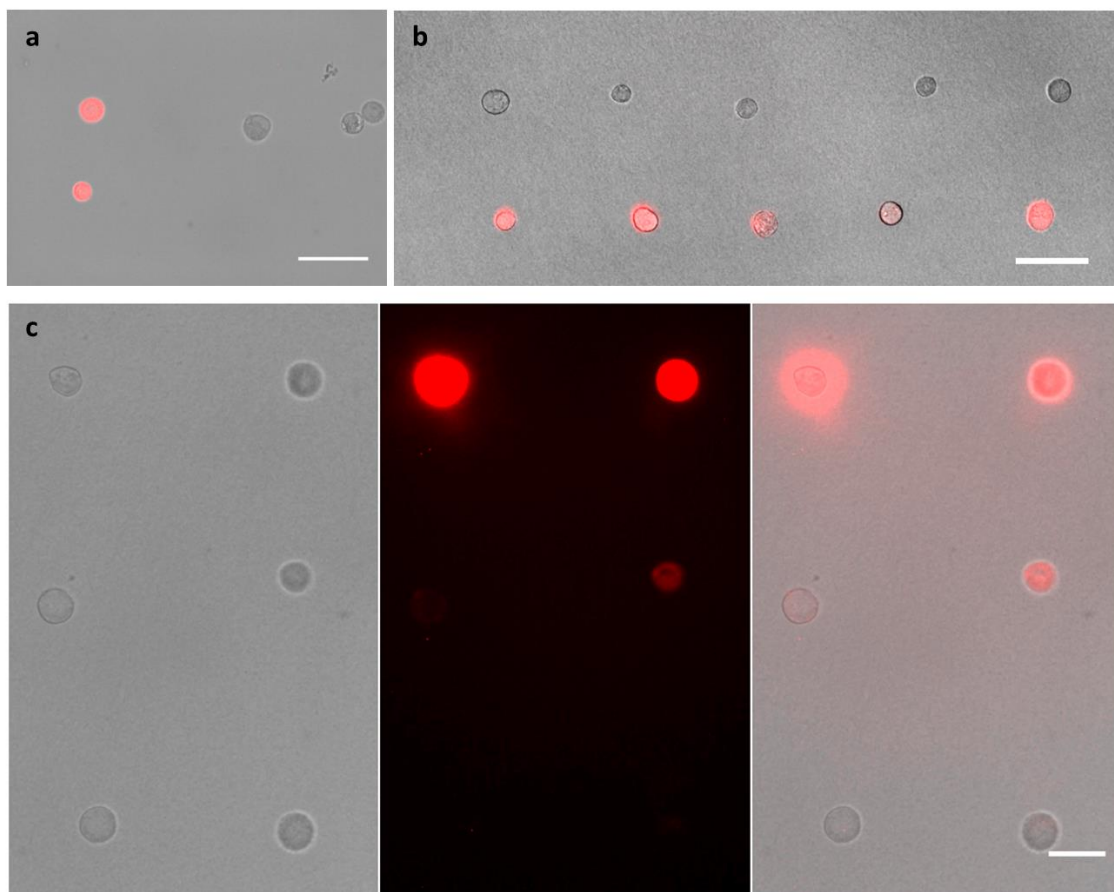
Figure 3.42 (a) Microscopy images of suspended fluorescent and non-fluorescent NHI 3T3 cells within the reservoir before printing. (b) Fluorescent cells can be sorted from non-fluorescent cells and lined up separately on the acceptor slide. (c) Transfected cells can be arranged depending on their fluorescence intensities. (a), (b) and (c, right column): merged bright field and fluorescence images; (c, left column): bright field microscopy image; (c, middle column): fluorescence illumination. Acceptor slides were coated with collagen. Scale bar = 50 μm. The figure has been published in article (22). Representative figure from 3 independent experiments.

3.4.4 Printing hydrogel in 3D

"As shown in Figure 3.14, this approach can also be used for transfer of higher viscos hydrogels. To demonstrate, that our setup can not only be used to select, place, and print individual cells and hydrogels in 2D, but also to extend the printing process into 3D, we printed five layers of the biocompatible thermo-reversible hydrogel pluronic F-127 on the acceptor substrate (Figure 3.43a). Here, the hydrogel pluronic F-127 was diluted to 15 wt% and cooled to 4°C. At this temperature, the pluronic solution has a viscosity of ≈40 mPas (89). Upon arrival at the acceptor substrate, which was kept at room temperature (22°C), the temperature of the pluronic hydrogel increased to room temperature, driving the pluronic hydrogel through its gel–sol transition and to a higher final viscosity, which is sufficient for stable 3D constructs. As can be seen in Figure 3.43b, the result is a well-defined 600 μm long, 120 μm wide line, which increases in height from about 37 μm at 1 layer to 140 μm at 5 layers (Figure 3.43c).

Therefore, simple 3D hydrogel structure can be established by using the fs laser-based bioprinting technique developed and investigated in this work". The text is obtained from the article (22).
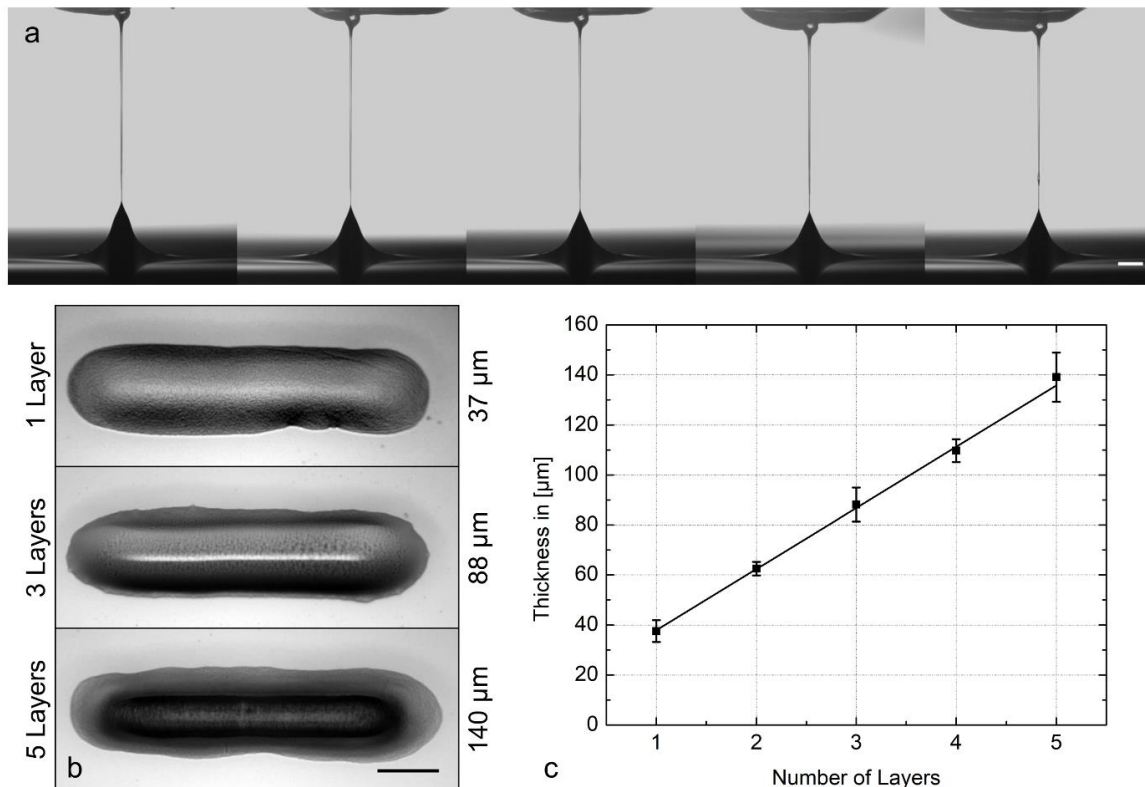
Figure 3.43 (a) Representative side view showing the 3D printing of Pluronic F-127 on the acceptor substrate (5 independent experiments) at a constant delay time of 200 μs. Hydrogel is transferred onto the acceptor slide. The distance between the hydrogel surface and the acceptor slide was 1 mm. A 3D hydrogel structure can be created layer-by-layer. (b) Microscope top view of the printed 3D lines at the acceptor slide. 5 layers of Pluronic results in 140 μm thickness. (c) Corresponding thickness versus number of layers. All data points in (c) represent average values ± standard deviations of 3 independent experiments. Scale bar is 100 μm. The figure has been published in article (22).

3.4.5 Positioning single cells on a protein-based 3D micro scaffold

"For the fabrication of functional tissue substitutes, it is often necessary to precisely position mammalian cells within pre-manufactured scaffolds or guiding rails. This is highlighted in Figure 3.44, where individual hMSCs were placed one by one on a pre-manufactured cross-linked bovine serum albumin (BSA) scaffold (97,98). Note that after the third cell was transferred to the BSA scaffold and placed in close proximity to the first and the second transferred cell, the second cell was slightly shifted. This was most likely driven by a hydrodynamic flow on the scaffold's surface, caused by the hydrogel carrying the third cell. Here, the test scaffold was pre-manufactured by 2-photon stereolithography. In future setups, one might even envision using the NIR fs laser for both the cell transfer and 2-photon

stereolithography within the same setup or integrating an additional laser for 2-photon stereolithography into the inverted microscope setup". The text is obtained from the article (22).

Figure 3.44 Representative bright field microscope images of post-printed single cell in a 3D scaffold (L×B×H=80×40×100 μm³) from 3 independent experiments. Scale bar is 20 μm. The figure has been published in article (22)*.*

4 Discussion

In this thesis, a novel laser-induced bioprinting approach for precise printing of living mammalian cells has been thoroughly investigated and successfully established, which avoids both, the use of inorganic absorbing layers and of UV laser sources. As the use of UV-lasers can induce DNA damage in the cells to be transferred and the insert of a sacrificial layer for laser energy absorption might be a source for contamination in the printed product. In addition, the approach presented in this thesis allows printing single living cells for the first time. Furthermore, it can select individual cells from heterogeneous cell populations based on cell morphology or fluorescence markers and then transfer them onto a 2D target substrate or a pre-processed 3D scaffold with single cell precision and high cell viability (93 - 99% cell survival, depending on cell type and substrate).

This laser-based transfer was investigated in detail as cell-free process, to optimize the experimental parameters including laser energy, focus depth, pulse duration, and laser focus shape. It could be shown that cells embedded within the hydrogel impair jet behavior requiring an adaptation of the transfer parameters. All of our results provide evidence that the threshold energy for cell transfer should be selected for printing of living cells, ensuring precise positioning of individual cells on the target substrate and high cell-survival rates.

4.1 Hydrodynamic analysis of cell-free transfer

4.1.1 Effect of laser pulse energies and focus depths on the hydrodynamic

By focusing an ultrashort laser pulse into the hydrogel, the laser intensity is well above the threshold for optical breakdown leading to a spatially confined optical breakdown with an initial pressure of few GPa (72). During the optical breakdown, a substantial part of the input energy can be absorbed and converted into mechanical energy expanding the cavitation bubble: Most of this energy is eventually dissipated by viscous damping, and some is concerted to elastic and surface energies (72,76,79). When the expanding bubble is near to the symmetry breaking liquid-air interface, the bubble generates a hydrogel jet and its energy is partially converted into kinetic driving the jet towards the acceptor surface (see Figure 2.2 for details) (60,70,74,99).

The liquid jet and cavitation bubble behavior can be described by a standoff parameter γ: the ratio of the distance of the bubble centroid from the free surface Z (here laser focus depth) and the maximum radius of the cavitation bubble in the liquid R_{max} (see Figure 2.1) (71,75).

As shown in Figure 3.7, faster jets can be observed by increasing the laser pulse energy. Trivially, as the incident laser pulse energy increases, more energy can convert into mechanical energy for the cavitation bubble expansion, resulting in a larger bubble size (i.e. R_{max}) (70,76). If the focus depth Z is constant, the dissipation effect can be estimated to be nearly constant during the bubble expansion. Therefore, more energy remains for the jet propagation, resulting in a faster jet with larger kinetic energy. However, the jet velocity decreases when increasing the laser focus depth as shown in Figure 3.10, because more energy is required for the displacement of the surrounding hydrogel. Consequently, less kinetic energy remains for the jet propagation, with less jet velocity. A similar jet behavior has been found previously in laser-based bio-printing with a donor-film made of hydrogel. The reduction of the donor-film thickness allows more energy conversion efficient between the bubble expansion and the hydrogel displacement (44). The standoff parameter γ decreases by increasing laser pulse energy with larger R_{max} or by decreasing the focus depth ($|z|$), leading to narrower jets, which is similar to previous numerical and experimental studies (74,75). By using a low laser pulse energy of 0.4 μJ or a high focus depth of 78 μm, the focus depth Z is higher than the bubble size R_{max} (i.e. $\gamma > 1$). In this case, the initial kinetic energy for jet propagation is not sufficient to overcome the surface energy with a Weber number $W_e < 4$, leading to no material transfer or hydrogel breakup.

If the kinetic energy of the hydrogel jet is sufficient to overcome the surface tension of the air–hydrogel interface, a continuous hydrogel jet can be formed (80,82). However, this jet is not able to develop infinitely, but breaks up into single or even multiple droplets, this phenomenon is attributed to the Rayleigh-Plateau instability (83). The breakup mechanisms can be classified into four different regimes by increasing the jet velocity as well as Weber and Reynolds numbers: Rayleigh breakup, first wind-induced as well as second wind-induced breakup and finally atomization as shown in **chapter** 2.3 Figure 2.6 (84,85).

Figure 4.1 and Figure 4.2 present the schematic images, which summarize the cavitation bubble dynamics and the jet ejection as well as the breakup regimes regarding the

variation of the laser pulse energy and focus depth. Figure 4.3 summarizes the breakup regime in variation of Reynolds and Weber numbers for printing of low viscos hydrogel (pure histopaque has a viscosity of 13 mPa·s).

The first jet develops in a laminar form with a velocity below 20 m/s (4 < W_e < 200 and 10 < R_e < 50) by using a low laser pulse energies of 1 and 2 μJ (see Figure 3.7) or a high focus depth of 52 and 65 μm (see Figure 3.10) and then breaks up into a primary droplet, whose diameter is larger than the jet. These regions are called the Rayleigh breakup and the first wind-induced regime (79,82,84,85). In the Rayleigh breakup regime, the jet velocity is just sufficient to lead to a pinch-off due to capillary forces. In the first wind-induced breakup regime, the jet breakup takes place later and the corresponding breakup length increases with the increasing jet velocity and the aerodynamic force caused by the relative motion between the liquid jet and ambient gas can be ignored. These laminar jets are called as well-defined regime. In this case, hydrogel jets develop in laminar form and creates well-defined circular hydrogel spots on the acceptor.

When further increasing the laser pulse energy or decreasing the focus depth, a change of the jet behavior from laminar to curved and even turbulent jets can be observed in Figure 3.7 (pulse energy of 3 and 4 μJ) and Figure 3.10 (focus depth of 39 μm) with a jet velocity between 30 and 50 m/s, this corresponds for following Weber and Reynolds numbers: 200 < W_e < 1000 and 50 < R_e < 100. In this case the aerodynamic force cannot be ignored any more, resulting in unstable surface tension forces oppose the jet propagation due to the second wind-induced breakup (84,85), resulting in much curved and even turbulent jets. As the jet velocity further increases above 50 m/s (We > 1000 and R_e > 100), the jet develops in a splashy and spray form and breaks up into lots of small droplets as shown in Figure 3.7 (5 μJ and 7 μJ) and Figure 3.10 (focus depth of 26 μm). This region is called atomization regime and is not suitable for the bioprinting. A disruptive force can be affected on the jet due to the unstable growing of instabilities existing in the liquid flow, resulting in the breakup of the hydrogel jet into lots smaller droplets (84,100,101). Similar splashing jets with a Weber number We > 1000 have been presented in previous work (71,79).
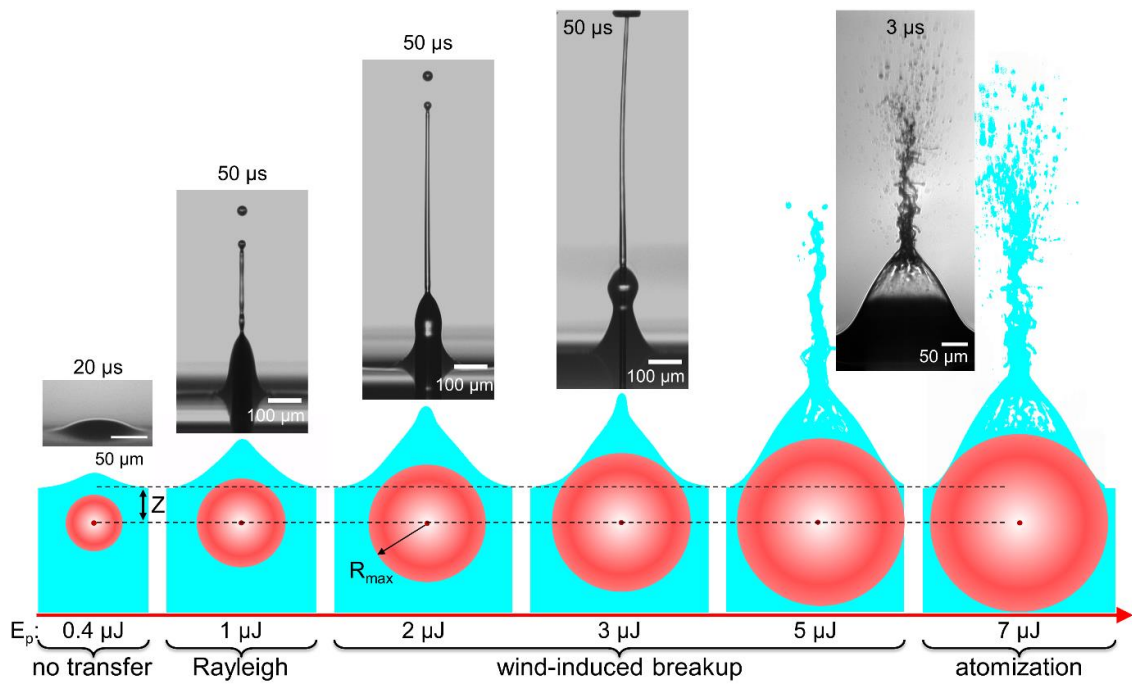
Figure 4.1 Correlation of the cavitation bubble size and the jet behavior in variation of the laser pulse energy, while the focus depth was fixed at 52 μm.
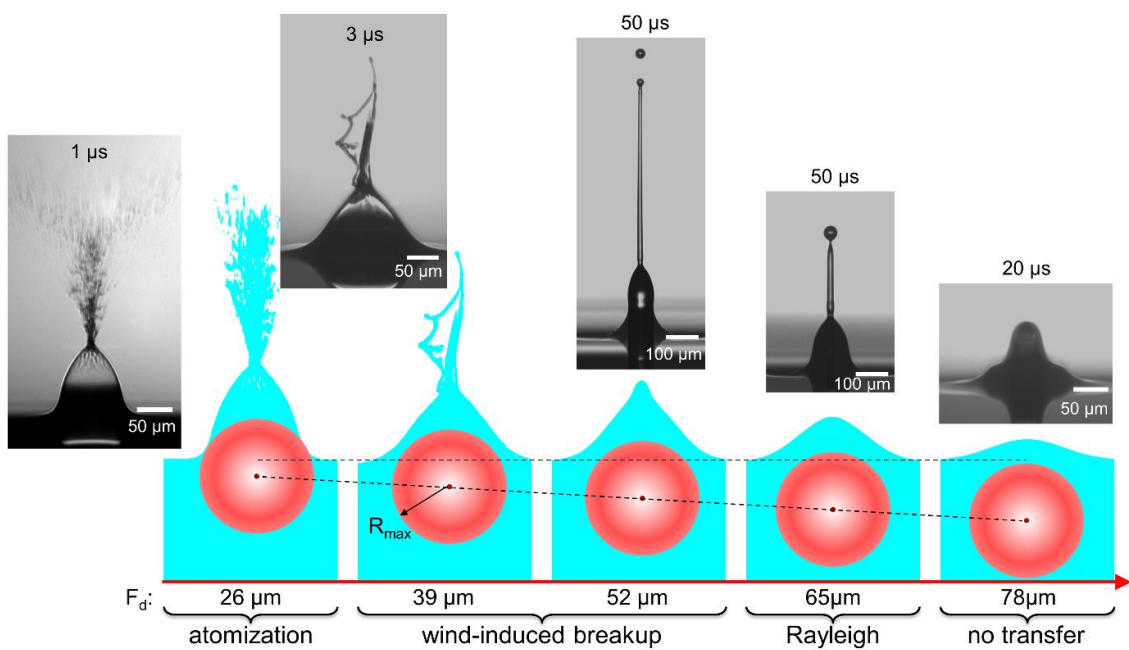
Figure 4.2 Correlation of the cavitation bubble size and the jet behavior in variation of the focus depth, while the laser pulse energy was fixed at 2 μJ.
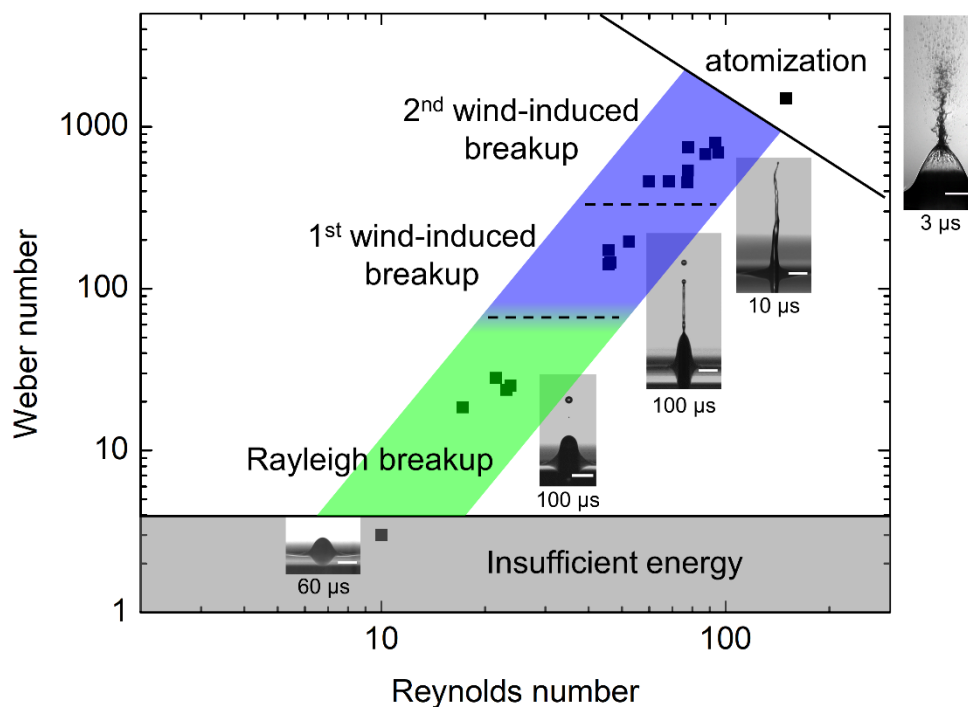
Figure 4.3 Breakup regime as a function of Reynolds and Weber numbers for printing of low viscos hydrogel (0% alginate). As the Weber and Reynolds numbers increase, the jet behavior changes from no material transfer to the laminar jets due to Rayleigh breakup and the first wind-induced breakup regime to a curved or even splashing jet form due to the second wind-induced and atomization breakup. All data points represent average values of 3 independent experiments.

4.1.2 Effect of hydrogel viscosities on the hydrodynamic

The breakup regime in variation of the Ohnesorge and Weber number are summarized in Figure 4.4. As shown in Figure 3.14, for 1.5% alginate and 2 µJ pulse energy, the kinetic energy of the hydrogel jet is insufficient to overcome the surface tension of the air–hydrogel interface and gravitational forces and the jet collapses without leaving the hydrogel reservoir. By increasing the hydrogel viscosity from 13 to 450 mPas, the Ohnesorge number increases from about 0.3 to 10 and thus the effect of viscosity on the jet behavior can no longer be ignored. It is not difficult to understand that, higher viscosity induces more resistance (i.e. shear force) for the deformation of the hydrogel in relative motion, such as the bubble expansion and jet propagation. Thus, more kinetic energy as well as a higher Weber number is required for transfer of higher viscos hydrogel due to higher dissipation effect, which is in good agreement of previous work (102). For details investigating the effect of the viscosity and corresponding breakup regimes, more hydrogel of higher viscosity should be investigated and analyzed in the future.
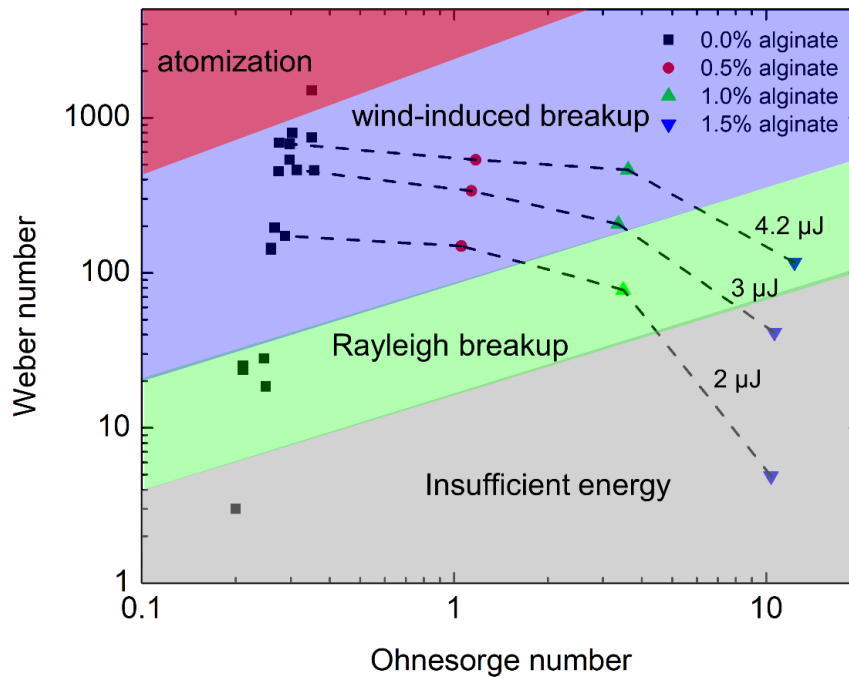
Figure 4.4 Breakup regime in variation of Ohnesorge and Weber numbers in variation of viscosity. As the Weber number increases, the jet behavior can change from no material transfer to a well-defined jet due to Rayleigh breakup to curved jet (first or second wind-induced breakup) to an undesired splashing jet (atomization). All data points represent average values of 3 independent experiments.

4.1.3   Effect of pulse durations on the hydrodynamic

As shown in Figure 3.30, the first jets develop in a stable laminar form without splashing for all pulse durations up to 14.1 ps, while the initial jet velocity v_1 decreases from 25.6±0.6 m/s for 0.6 ps to 24.0±0.8 m/s for 1.8 ps to 17.5±1.0 m/s for 9.7 ps and to 14.3±1.0 m/s for 14.1 ps. Smaller cavitation bubbles can be observed by increasing the laser pulse duration (see Figure 3.31), as a result of a drop of the energy conversion efficiency from about 12.5% at 600 fs to 7.5% at 14.1 ps pulse duration. These decreases are similar to the above-mentioned jet development when using lower pulse energy. According to Kennedy's model, in ultrashort pulse regime < 100 fs, the optical breakdown is dominated by only "pure" multiphoton ionization, as the critical free electron density 10^{21} cm^{-3} can be achieved before the cascade ionization completes (103–105). As the pulse duration increases, the multiphoton process would "jump start" to cascade. The multiphoton absorption depends strongly on the irradiation I^k, which is inversely proportional to pulse duration (106). Additionally, comparing pico- to femtosecond laser pulses the critical electron density can be achieved much later during the laser pulse due to the decreasing role of the multiphoton ionization (76,107), thus more laser pulse energy can be transmitted before the breakdown occurs. Thus, the pulse-duration dependent absorption efficiency decrease may be the key reason for the reduction

of the bubble energy and jet kinetic energy observed by us for comparable laser pulse energies, wavelengths and pulse durations.

4.2 Hydrodynamic analysis of cell-laden transfer

As described above, an identical hydrogel was used in the reservoir for both - cell-free and cell-laden bioprinting. By using the same laser parameters, identical initial forces should act on the hydrogel surface and the suspended cells due to the expanding bubble. This is confirmed by the almost identical protrusions of the cell-free and the cell-laden transfer at the early stages at about 1 and 3 μs as shown in Figure 3.18 and Figure 3.20. Below a laser pulse energy of 2 μJ or a focus depth above 52 μm, the jet behavior of cell-free and cell-laden printing has no significant difference: both develop straight up with a similar velocity < 20 m/s ($4 < W_e < 200$ and $10 < R_e < 50$). By using a higher laser pulse energy, however, (3 and 4 μJ in Figure 3.18) or a lower focus depth (39 μm in Figure 3.20), the printed single cell develops a much higher velocity and then separates from the first jet. As the living cells separate from the jet, there is almost no hydrogel surrounding the printed cells and the impact on the acceptor slide occurs with a high velocity above 40 m/s.

Cells can be easily accelerated due to their lower density of mass, under an identical initial force, resulting in a higher velocity than the surrounding hydrogel. A drag force also called fluid resistance can act opposite to the relative motion of an object (living cells with intact membrane) moving within a viscous liquid (108). Therefore, the separation of the printed cells from the jet front can take place only when the acceleration force exerted on the cells is high enough to overcome the drag force between cells and the surrounding hydrogel. After the separation of living cells from the jet front, the cell-laden jet has higher Weber and Reynolds numbers than that from the cell-free jet. The transfer of momentum from the separated single cell to the jet results in a repulsive force, leading to more curved jets. If the initial force acting on cells is not sufficient to overcome the drag force on the cells, thus, no separation of the printed cells from the jet front can be observed. Cells were transferred within the primary droplet with surrounding hydrogel and exhibits a similar diameter as the cell-free primary droplet.

4.3 Hydrogel printing resolution and single cell positioning accuracy

By increasing the applied laser pulse energy, more hydrogel from the first jet and even the second jet can be transferred, resulting in larger hydrogel spot on the acceptor slide, which reduces the spatial printing resolution. Therefore, a minimal pulse energy should be used for obtaining the smallest spots, and thus for obtaining optimal spatial printing resolution for creating 2D and 3D cell structures as shown in Figure 3.9. More threshold energy is required for the transfer with higher focus depth and a larger primary droplet is separated from the first jet. The primary droplet size is proportional to the first jet width, due to the Rayleigh-breakup (74,83,100), resulting in a larger hydrogel spot at the acceptor slide and a reduced the spatial resolution.

The spatial printing accuracy of the transferred cells is of high interest for the generation of nature-mimicking cell environments and cell niches, which can further stimulate cells to migrate, differentiate and proliferate to form functional tissue. As shown in Figure 3.22, the deviation from the target position of a single cell increases with the hydrogel spot size on the acceptor slide, because the transferred cells are located randomly within the hydrogel spot on the acceptor slide. Therefore, for high spatial printing accuracy of the transferred cells, only the primary droplet containing one single cell should be transferred to the accepter slide.

4.4 Analysis of cell-damage

Besides the printing resolution and cell positioning accuracy, high cell survival rates and good cell viability are key parameters for biofabrication techniques in tissue engineering. The most likely causes of cell damage in laser-induced cell transfer are radiation and thermal damage from the applied laser source, mechanical stresses from the expanding cavitation bubble, shear forces, as cells are moving through the hydrogel, and forces caused by the impact of landing cells on the acceptor (42,64,109–111). In this work the laser wavelength of 1030 nm was chosen, which is in the so-called biological optical window: For this wavelength, the linear optical interaction between photons and biological material reaches a minimum, and practically no laser energy is absorbed by cells or other biomaterial (49,50) and thereby the risk of inducing photochemical damage is minimized. As the laser beam is focused underneath the hydrogel surface about 40 to 80 μm and the resulting a laser focus has a beam waist of about 1 μm, thus the cells which are near the hydrogel surface where energy densities

are not sufficient for multi-photon absorption (65,70) hardly interact with near infrared radiation.

In addition, it has been shown, that energy absorption, and cavitation bubble expansion is much faster than energy transport through thermal conductivity, and that heating effects outside of the laser focus can be neglected (64,112). Previous works have demonstrated that tightly focused fs laser pulses can generate spatially extremely confined chemical, thermal, and mechanical effects in transparent materials (65). Therefore, both of the radiation and thermal damage can only occur within the laser focus. The mechanical damage induced by the transfer process itself is therefore believed to be the key remaining source of cell damage.

As shown in Figure 3.32, for the inverted configuration, elongated cavitation bubbles can be generated caused by spherical aberration, which may penetrate the suspended cells and lead to cell damage. Thus, our results demonstrate that only the spherical aberration corrected water immersion objective can be integrated into the inverted microscope setup for printing of living cells.

As demonstrated above, more mechanical energy can be deposited for the bubble expansion with larger bubble size by using higher pulse energy. The acceleration forces on the suspended cells caused by the expanding cavitation bubble can be decreased by increasing the focus depth. By using too much laser pulse energy or a too low focus depth, the suspended cells can be impaired by high acceleration forces or may even be penetrated by the rapid expanding cavitation bubbles, leading to a low cell viability (see Figure 3.34 red area can be regarded as deadly zone). Thus, potential cell damage effect can be minimized by using the threshold pulse energy for the transfer.

By increasing the laser pulse duration, less energy can be converted into mechanical energy for the cavitation bubble expansion, resulting in less energy for jet propagation. Nevertheless, our results show that almost all of the printed cells survived laser pulse durations in the range from 600 fs to 14.1 ps. Thus, effect of the pulse durations in this range on the cell viability plays a minor role for the printing process. The transfer process induced by longer pulse durations such as sub- and nanoseconds and its effect on the cell viability should be carried out in more detail in future.

Finally, the fact that higher cell survival rates are obtained from the slower and thicker second jet (Figure 3.2), suggests that the impact of the landing cells at the acceptor surface is also a source of cell damage. The larger droplets generated by the second jet seem to cushion the impact more effectively than smaller droplets from the first jet. Furthermore, acceleration and shear forces during jet generation and expansion, as well as deceleration forces are reduced for the wider and more slowly moving second jet.

4.5 Analysis of cell-cell interactions

As shown in Figure 3.40 and Figure 3.41, the cell-cell interactions were studied, by printing single cells with different intercellular spacing on a substrate. "*Cells with low intercell spacing below 100 µm start to polarize and elongate toward neighboring cells, while the 200 µm separated cells remain isolated and are seemingly unaffected by their neighbors. This indicates paracrine and/or substrate mediated mechanical communication between the cells, stimulating cell elongation at intercell distances of below 100 µm, while at larger intercell spacing, the biochemical and/or mechanical signals do not reach the neighboring cells. This is most likely due to the lack of external guidance by the ECM. In native tendon, the tenocytes, which in vivo derive from TSPCs, align themselves in parallel longitudinal rows separated by collagen fibers* (113). *The cell-cell contact is mediated via gap and adherens junctions, which are associated to actin stress fibers. The orientation of those fibers aligns with the longitudinal cell orientation and thereby, specific mechano-sensitive signal transductions pathways are triggered allowing cells to sense the tensile loads in the tissue* (114–116). *To engineer tendon tissue, the establishment of such cell-cell contacts is therefore critical to obtain functional tissue mimetic constructs* (5)". The text is obtained from the article (22).

Taken together, by increasing the laser pulse energy or decreasing the focus depth, more laser energy can be converted to kinetic energy driving the jet propagation with higher velocity. For printing higher viscos hydrogels, more energy is dissipated due to higher shear force which leads to less kinetic energy for jet propagation. Less laser energy can be absorbed during the optical breakdown by increasing the pulse durations from 600 fs to 14.1 ps, resulting in less kinetic energy for jet propagation with low jet velocity. By increasing jet velocity, the jet behavior exhibited four characteristic behaviors: (1) The kinetic energy of the jet is too low and not sufficient to overcome the surface tension of the air–hydrogel interface, thus no material is transferred. (2) Laminar jet due to the Rayleigh and the first wind-induced

breakup reaching the target substrate on a linear trajectory. (3) Curved and turbulent jet due to the second wind-induced breakup, as the aerodynamic force cannot be ignored and resulting in unstable surface tension forces oppose the jet propagation. (4) The atomization induced undesired splashing jet. Our results demonstrated that a threshold energy for hydrogel and cell transfer should be used to obtain a laminar jet (well-defined regime). In this case, the kinetic energy for jet propagation is just high enough to overcome the hydrogel surface energy and gravity, only the primary droplet can be transferred, resulting in the highest printing resolution (minimal spot size about 50 µm) as well as the best single cell positioning precision close to 10 µm. In addition, all of the potential sources of cell damage can be significantly reduced and minimized by using the threshold transfer conditions, resulting in a high cell viability (93–99% cell survival, depending on cell type and substrate). The use of a medium immersion objective to correct the spherical aberration is necessary for preserving cell viability in single cell bioprinting. Cells can polarize and elongate towards neighboring cells with low intercell spacing below 100 µm, while at larger intercell spacing the biochemical and/or mechanical signals do not reach the neighboring cells. This result suggests that, controlling the cellular microenvironment *in vitro* with single cell precision is therefore an important factor for the generation of instructive cell environments and cell niches, which stimulate cells to migrate, differentiate, proliferate and can form functional tissue.

5 Conclusion

Laser-induced cell transfer has been developed in recent years for the flexible and gentle printing of cells. Because of the high transfer rates and superior cell survival rates, this technique has great potential for tissue engineering applications. However, the transferred construction can be contaminated with inorganic material or it brings the risk of DNA damage by using UV laser sources. Until now, there is no reliable bioprinting technique enabling efficient and precise printing of living cells at the single cell precision.

The results of this thesis can be summarized as follows:

1. **A novel single cell bioprinting method with ultrashort laser pulses using living cells has been established.**

For the first time, we established laser-based bioprinting technology, which does not require any sacrificial material for energy absorption, or the use of UV lasers. The transferred cells had 93–99% survival rates on the target substrate. They maintained their ability to migrate and proliferate, and show normal, cell type specific behavior after transfer. No DNA double strand breaks could be detected.

2. **A time-resolved imaging setup for visualizing the transfer process and to investigate and optimize the effects of the experimental parameters on the cell viability and the printing precision has been established.**

With a time-resolved imaging system we were able to investigate the transfer kinetics in detail. We then investigated in systematical manner the effects of the experimental parameters such as laser pulse energy, focus depth, hydrogel viscosity, laser pulse duration and spherical aberration of the microscope objectives on the cavitation bubble formation and jet kinetics and the corresponding hydrodynamics. Our results demonstrated that a threshold energy for hydrogel and cell transfer should be used to obtain a laminar jet (well-defined regime). In this case, the kinetic energy for jet propagation is just high enough to overcome the hydrogel surface energy and gravity, only the primary droplet can be transferred, resulting in the highest printing resolution (minimal spot size about 50 µm) as well as the best single cell positioning precision close to 10 µm. For the cell transfer, the cell damage could be

significantly reduced and minimized using the threshold conditions, resulting a high cell viability (93–99% cell survival, depending on cell type and substrate).

3. Single cell sorting method has been established by integrating the bioprinting approach into an inverted epi-florescence microscope.

We successfully integrated laser-induced bioprinting into an inverted optical microscope, which allows to select and sort individual cells from heterogeneous cell populations, based on cell morphology (e.g. cell shape or size) or fluorescence markers.

4. Single cells can be precisely transferred to target substrate or a pre-manufactured scaffold and arranged to create high precision cell nichoids.

Cellular microenvironment *in vitro* can be controlled by single cell printing for a better understanding of cell behavior under normal and pathological conditions. Additionally, the fabrication of precision nichoids can replicate and mimic the complex and unique cellular microarchitecture of the native tissue.

6   Outlook

In the future "the experimental parameters should be further optimized, to increase the cell viability to above 99% and reach a single cell positioning accuracy of less than 5 µm. At present, selecting the cell, focusing and positioning the target surface are the rate limiting steps. The process should be further automated and accelerated: the shown integration into an inverted optical microscope setup, will allow the use of automated image analysis and a cell recognition software, which is a prerequisite for a fully automated process. The cell transfer process alone requires less than 100 µs per cell, which would allow transfer rates of ~10 kHz. By using a multiplexing approach with fast laser scanners, one can envision even faster cell transfer rates in the future, which are limited only by the laser repetition rate. This approach will enable the precise, fast and cell friendly fabrication of cell-chips, organs-on-a-chips, 3D organoids, and ultimately of functional tissue substitutes. With the generated cell niches, cell migration, differentiation and proliferation can be studied on a single cell level, with the prospect of creating functional tissues in the future. More applications, such as exploration of paracrine signaling between the same or different cell types, or cell biomechanics, or single cell sorting and analysis should also be explored in follow up studies". The text is obtained from the article (22).

Using this technology, living cells and extracellular matrix molecules ECM can be precisely transferred and arranged to create 2D and 3D cell nichoids, which can replicate and mimic the complex and unique molecular and cellular microarchitecture of the native tissue in future applications. This single cell printing approach has therefore the potential to become an important tool to study the role of cell and ECM architecture in tissue homeostasis, but also in the pathogenesis of diseases. In addition, it can be used for drug discovery and improve the treatment of lesions caused by injuries or diseases. As an example from the musculoskeletal system, we aim to generate with this technology high precision tendon and cartilage niches exhibiting key molecular and cellular features in follow up studies.

Reference

1.	Kitano K, Schwartz DM, Zhou H, Gilpin SE, Wojtkiewicz GR, Ren X, et al. Bioengineering of functional human induced pluripotent stem cell-derived intestinal grafts. Nat Commun [Internet]. 2017;8(1). Available from: http://dx.doi.org/10.1038/s41467-017-00779-y

2.	Rao L, Qian Y, Khodabukus A, Ribar T, Bursac N. Engineering human pluripotent stem cells into a functional skeletal muscle tissue. Nat Commun [Internet]. 2018;9(1):1–12. Available from: http://dx.doi.org/10.1038/s41467-017-02636-4

3.	Zheng Y, Hong X, Wang J, Feng L, Fan T, Guo R, et al. 2D Nanomaterials for Tissue Engineering and Regenerative Nanomedicines: Recent Advances and Future Challenges. Adv Healthc Mater. 2021;10(7):1–22.

4.	Dex S, Alberton P, Willkomm L, Söllradl T, Bago S, Milz S, et al. Tenomodulin is Required for Tendon Endurance Running and Collagen I Fibril Adaptation to Mechanical Load. EBioMedicine [Internet]. 2017;20:240–54. Available from: http://dx.doi.org/10.1016/j.ebiom.2017.05.003

5.	Richardson SH, Starborg T, Lu Y, Humphries SM, Meadows RS, Kadler KE. Tendon Development Requires Regulation of Cell Condensation and Cell Shape via Cadherin-11-Mediated Cell-Cell Junctions. Mol Cell Biol [Internet]. 2007 Sep 1;27(17):6218–28. Available from: https://mcb.asm.org/content/27/17/6218

6.	Ionov L. 4D Biofabrication: Materials, Methods, and Applications. Adv Healthc Mater [Internet]. 2018 Sep;7(17):1800412. Available from: http://doi.wiley.com/10.1002/adhm.201800412

7.	Onofrillo C, Duchi S, O'Connell CD, Blanchard R, O'Connor AJ, Scott M, et al. Biofabrication of human articular cartilage: a path towards the development of a clinical treatment. Biofabrication [Internet]. 2018 Aug;10(4):45006. Available from: https://doi.org/10.1088%2F1758-5090%2Faad8d9

8.	Moroni L, Burdick JA, Highley C, Lee SJ, Morimoto Y, Takeuchi S, et al. Biofabrication strategies for 3D in vitro models and regenerative medicine. Nat Rev Mater [Internet].

2018 May 26;3(5):21–37. Available from: http://dx.doi.org/10.1038/s41578-018-0006-y

9. Liu T, Yao R, Pang Y, Sun W. Review on biofabrication and applications of heterogeneous tumor models. J Tissue Eng Regen Med [Internet]. 2019 Nov 28;13(11):2101–20. Available from: https://onlinelibrary.wiley.com/doi/abs/10.1002/term.2949

10. Jakab K, Marga F, Kaesser R, Chuang TH, Varadaraju H, Cassingham D, et al. Non-medical applications of tissue engineering: biofabrication of a leather-like material. Mater Today Sustain [Internet]. 2019;5:100018. Available from: https://doi.org/10.1016/j.mtsust.2019.100018

11. Sun W, Starly B, Daly AC, Burdick JA, Groll J, Skeldon G, et al. The bioprinting roadmap. Biofabrication [Internet]. 2020 Feb 6;12(2):022002. Available from: https://iopscience.iop.org/article/10.1088/1758-5090/ab5158

12. Papadimitriou L, Manganas P, Ranella A, Stratakis E. Biofabrication for neural tissue engineering applications. Mater Today Bio [Internet]. 2020 Mar;6(January):100043. Available from: https://doi.org/10.1016/j.mtbio.2020.100043

13. Graney PL, Ben-Shaul S, Landau S, Bajpai A, Singh B, Eager J, et al. Macrophages of diverse phenotypes drive vascularization of engineered tissues. Sci Adv. 2020;6(18):eaay6391.

14. Discher DE, Mooney DJ, Zandstra PW. Growth Factors, Matrices, and Forces Combine and Control Stem Cells. Science (80-) [Internet]. 2009 Jun 26;324(5935):1673–7. Available from: https://www.sciencemag.org/lookup/doi/10.1126/science.1171643

15. Graf T, Enver T. Forcing cells to change lineages. Nature [Internet]. 2009 Dec;462(7273):587–94. Available from: http://dx.doi.org/10.1038/nature08533

16. Barriga EH, Franze K, Charras G, Mayor R. Tissue stiffening coordinates morphogenesis by triggering collective cell migration in vivo. Nature [Internet]. 2018 Feb 14;554(7693):523–7. Available from: http://www.nature.com/articles/nature25742

17. Friedl P, Alexander S. Cancer Invasion and the Microenvironment: Plasticity and

Reciprocity. Cell [Internet]. 2011 Nov;147(5):992–1009. Available from: https://linkinghub.elsevier.com/retrieve/pii/S0092867411013547

18. Reuten R, Zendehroud S, Nicolau M, Fleischhauer L, Laitala A, Kiderlen S, et al. Basement membrane stiffness determines metastases formation. Nat Mater [Internet]. 2021 Jan 25; Available from: http://www.nature.com/articles/s41563-020-00894-0

19. Lautenschläger F, Piel M. Microfabricated devices for cell biology: all for one and one for all. Curr Opin Cell Biol [Internet]. 2013 Feb;25(1):116–24. Available from: https://linkinghub.elsevier.com/retrieve/pii/S0955067412001810

20. Park JA, Yoon S, Kwon J, Now H, Kim YK, Kim WJ, et al. Freeform micropatterning of living cells into cell culture medium using direct inkjet printing. Sci Rep [Internet]. 2017;7(1):14610. Available from: http://dx.doi.org/10.1038/s41598-017-14726-w

21. Nie J, Gao Q, Fu J, He Y. Grafting of 3D Bioprinting to In Vitro Drug Screening: A Review. Adv Healthc Mater [Internet]. 2020 Apr 3;9(7):1901773. Available from: https://onlinelibrary.wiley.com/doi/abs/10.1002/adhm.201901773

22. Zhang J, Byers P, Erben A, Frank C, Schulte-Spechtel L, Heymann M, et al. Single Cell Bioprinting with Ultrashort Laser Pulses. Adv Funct Mater [Internet]. 2021 Mar 26;2100066. Available from: https://onlinelibrary.wiley.com/doi/10.1002/adfm.202100066

23. Gruene M, Unger C, Koch L, Deiwick A, Chichkov B. Dispensing pico to nanolitre of a natural hydrogel by laser-assisted bioprinting. Biomed Eng Online [Internet]. 2011;10(1):19. Available from: http://biomedical-engineering-online.biomedcentral.com/articles/10.1186/1475-925X-10-19

24. Gruene M, Pflaum M, Hess C, Diamantouros S, Schlie S, Deiwick A, et al. Laser Printing of Three-Dimensional Multicellular Arrays for Studies of Cell–Cell and Cell–Environment Interactions. Tissue Eng Part C Methods [Internet]. 2011 Oct;17(10):973–82. Available from: https://www.liebertpub.com/doi/10.1089/ten.tec.2011.0185

25. Koch L, Kuhn S, Sorg H, Gruene M, Schlie S, Gaebel R, et al. Laser Printing of Skin Cells and Human Stem Cells. Tissue Eng Part C Methods [Internet]. 2010 Oct;16(5):847–54.

Available from: https://www.liebertpub.com/doi/10.1089/ten.tec.2009.0397

26.   Ringeisen BR, Kim H, Barron JA, Krizman DB, Chrisey DB, Jackman S, et al. Laser Printing
        of Pluripotent Embryonal Carcinoma Cells. Tissue Eng [Internet]. 2004 Mar;10(3–
        4):483–91.   Available   from:
        https://www.liebertpub.com/doi/10.1089/107632704323061843

27.   Barron JA, Spargo BJ, Ringeisen BR. Biological laser printing of three dimensional cellular
        structures. Appl Phys A [Internet]. 2004 Sep 1;79(4–6):1027–30. Available from:
        http://link.springer.com/10.1007/s00339-004-2620-3

28.   Ivanov DP, Parker TL, Walker DA, Alexander C, Ashford MB, Gellert PR, et al.
        Multiplexing Spheroid Volume, Resazurin and Acid Phosphatase Viability Assays for
        High-Throughput Screening of Tumour Spheroids and Stem Cell Neurospheres. Mancini
        MA, editor. PLoS One [Internet]. 2014 Aug 13;9(8):e103817. Available from:
        https://dx.plos.org/10.1371/journal.pone.0103817

29.   Doraiswamy A, Narayan RJ, Lippert T, Urech L, Wokaun A, Nagel M, et al. Excimer laser
        forward transfer of mammalian cells using a novel triazene absorbing layer. Appl Surf
        Sci   [Internet].   2006   Apr;252(13):4743–7.   Available   from:
        https://linkinghub.elsevier.com/retrieve/pii/S0169433205014467

30.   Koch L, Deiwick A, Franke A, Schwanke K, Haverich A, Zweigerdt R, et al. Laser
        bioprinting of human induced pluripotent stem cells—the effect of printing and
        biomaterials on cell survival, pluripotency, and differentiation. Biofabrication [Internet].
        2018   Apr   25;10(3):035005.   Available   from:
        https://iopscience.iop.org/article/10.1088/1758-5090/aab981

31.   Guillotin B, Souquet A, Catros S, Duocastella M, Pippenger B, Bellance S, et al. Laser
        assisted bioprinting of engineered tissue with high cell density and microscale
        organization. Biomaterials [Internet]. 2010 Oct;31(28):7250–6. Available from:
        https://linkinghub.elsevier.com/retrieve/pii/S0142961210006927

32.   Ali M, Pages E, Ducom A, Fontaine A, Guillemot F. Controlling laser-induced jet
        formation for bioprinting mesenchymal stem cells with high viability and high
        resolution. Biofabrication [Internet]. 2014 Sep 12;6(4):045001. Available from:

https://iopscience.iop.org/article/10.1088/1758-5082/6/4/045001

33.   Piqué A, Chrisey D, Auyeung R, Fitz-Gerald J, Wu HD, McGill R, et al. A novel laser transfer process for direct writing of electronic and sensor materials. Appl Phys A Mater Sci Process [Internet]. 1999 Dec 1;69(7):S279–84. Available from: http://link.springer.com/10.1007/s003390051400

34.   Serra P, Piqué A. Laser-Induced Forward Transfer: Fundamentals and Applications. Adv Mater Technol [Internet]. 2019 Jan;4(1):1800099. Available from: http://doi.wiley.com/10.1002/admt.201800099

35.   Bohandy J, Kim BF, Adrian FJ. Metal deposition from a supported metal film using an excimer laser. J Appl Phys [Internet]. 1986 Aug 15;60(4):1538–9. Available from: http://aip.scitation.org/doi/10.1063/1.337287

36.   Serra P. Laser-induced forward Transfer: a Direct-writing Technique for Biosensors Preparation. J Laser Micro/Nanoengineering [Internet]. 2006 Dec;1(3):236–42. Available from: http://www.jlps.gr.jp/jlmn/assets/bd8c51eeea5c476228d86c28e73635c3.pdf

37.   Duocastella M. Laser-induced Forward Transfer of Liquids for Miniaturized Biosensors Preparation. J Laser Micro/Nanoengineering [Internet]. 2008 Jan;3(1):1–4. Available from: http://www.jlps.gr.jp/jlmn/assets/8ff90736c3226b4de15c8eb3c24acc41.pdf

38.   Colina M, Serra P, Fernández-Pradas JM, Sevilla L, Morenza JL. DNA deposition through laser induced forward transfer. Biosens Bioelectron [Internet]. 2005 Feb;20(8):1638–42. Available from: https://linkinghub.elsevier.com/retrieve/pii/S0956566304003720

39.   Serra P, Colina M, Fernández-Pradas JM, Sevilla L, Morenza JL. Preparation of functional DNA microarrays through laser-induced forward transfer. Appl Phys Lett [Internet]. 2004 Aug 30;85(9):1639–41. Available from: http://aip.scitation.org/doi/10.1063/1.1787614

40.   Koch L, Deiwick A, Chichkov B. Laser-based 3D cell printing for tissue engineering. BioNanoMaterials [Internet]. 2014 Jan 1;15(3–4):71–8. Available from: https://www.degruyter.com/document/doi/10.1515/bnm-2014-0005/html

41.   Barron JA, Ringeisen BR, Kim H, Spargo BJ, Chrisey DB. Application of laser printing to mammalian cells. Thin Solid Films [Internet]. 2004 Apr;453–454:383–7. Available from: https://linkinghub.elsevier.com/retrieve/pii/S004060900301681X

42.   Lin Y, Huang Y, Wang G, Tzeng T-RJ, Chrisey DB. Effect of laser fluence on yeast cell viability in laser-assisted cell transfer. J Appl Phys [Internet]. 2009 Aug 15;106(4):043106. Available from: http://aip.scitation.org/doi/10.1063/1.3202388

43.   Brown MS, Kattamis NT, Arnold CB. Time-resolved study of polyimide absorption layers for blister-actuated laser-induced forward transfer. J Appl Phys [Internet]. 2010 Apr 15;107(8):083103. Available from: http://aip.scitation.org/doi/10.1063/1.3327432

44.   Brown MS, Brasz CF, Ventikos Y, Arnold CB. Impulsively actuated jets from thin liquid films for high-resolution printing applications. J Fluid Mech [Internet]. 2012 Oct 25;709:341–70. Available from: https://www.cambridge.org/core/product/identifier/S0022112012003370/type/journal_article

45.   Xiong R, Zhang Z, Chai W, Chrisey DB, Huang Y. Study of gelatin as an effective energy absorbing layer for laser bioprinting. Biofabrication [Internet]. 2017 Jun 9;9(2):024103. Available from: https://iopscience.iop.org/article/10.1088/1758-5090/aa74f2

46.   Colina M, Duocastella M, Fernández-Pradas JM, Serra P, Morenza JL. Laser-induced forward transfer of liquids: Study of the droplet ejection process. J Appl Phys [Internet]. 2006 Apr 15;99(8):084909. Available from: http://aip.scitation.org/doi/10.1063/1.2191569

47.   Schiele NR, Chrisey DB, Corr DT. Gelatin-Based Laser Direct-Write Technique for the Precise Spatial Patterning of Cells. Tissue Eng Part C Methods [Internet]. 2011 Mar;17(3):289–98. Available from: https://www.liebertpub.com/doi/10.1089/ten.tec.2010.0442

48.   Raof NA, Schiele NR, Xie Y, Chrisey DB, Corr DT. The maintenance of pluripotency following laser direct-write of mouse embryonic stem cells. Biomaterials [Internet]. 2011 Mar;32(7):1802–8. Available from: https://linkinghub.elsevier.com/retrieve/pii/S0142961210014377

49.   Hammer BE. Physical Properties of Tissues. Radiology [Internet]. 1991 Oct;181(1):128–128. Available from: http://pubs.rsna.org/doi/10.1148/radiology.181.1.128

50.   Ronald W. Waynant. Lasers in Medicine [Internet]. Waynant RW, editor. CRC Press; 2011. Available from: https://www.taylorfrancis.com/books/9781420040746

51.   Zhang AM, Cui P, Cui J, Wang QX. Experimental study on bubble dynamics subject to buoyancy. J Fluid Mech [Internet]. 2015 Aug 10;776:137–60. Available from: https://www.cambridge.org/core/product/identifier/S0022112015003237/type/journal_article

52.   Antoshin AA, Churbanov SN, Minaev NV, Zhang D, Zhang Y, Shpichka AI, et al. LIFT-bioprinting, is it worth it? Bioprinting [Internet]. 2019 Sep;15:e00052. Available from: https://linkinghub.elsevier.com/retrieve/pii/S240588661930017X

53.   Koch L, Brandt O, Deiwick A, Chichkov B. Laser assisted bioprinting at different wavelengths and pulse durations with a metal dynamic release layer: A parametric study. Int J Bioprinting [Internet]. 2017 Jan 23;3(1):42–53. Available from: http://ijb.whioce.com/index.php/int-j-bioprinting/article/view/96

54.   Guillemot F, Souquet A, Catros S, Guillotin B, Lopez J, Faucon M, et al. High-throughput laser printing of cells and biomaterials for tissue engineering. Acta Biomater [Internet]. 2010 Jul;6(7):2494–500. Available from: https://linkinghub.elsevier.com/retrieve/pii/S1742706109004395

55.   Pirlo RK, Wu P, Liu J, Ringeisen B. PLGA/hydrogel biopapers as a stackable substrate for printing HUVEC networks via BioLP^{TM}. Biotechnol Bioeng [Internet]. 2012 Jan;109(1):262–73. Available from: http://doi.wiley.com/10.1002/bit.23295

56.   Koch L, Deiwick A, Schlie S, Michael S, Gruene M, Coger V, et al. Skin tissue generation by laser cell printing. Biotechnol Bioeng [Internet]. 2012 Jul;109(7):1855–63. Available from: http://doi.wiley.com/10.1002/bit.24455

57.   Patrascioiu A, Duocastella M, Fernández-Pradas JM, Morenza JL, Serra P. Liquids microprinting through a novel film-free femtosecond laser based technique. Appl Surf Sci [Internet]. 2011 Apr;257(12):5190–4. Available from:

https://linkinghub.elsevier.com/retrieve/pii/S0169433210016168

58.   Zhang Z, Xu C, Xiong R, Chrisey DB, Huang Y. Effects of living cells on the bioink printability during laser printing. Biomicrofluidics [Internet]. 2017 May;11(3):034120. Available from: http://aip.scitation.org/doi/10.1063/1.4985652

59.   Koch L, Deiwick A, Chichkov B. Laser-Based Cell Printing. In: 3D Printing and Biofabrication [Internet]. Cham: Springer International Publishing; 2018. p. 303–29. Available from: http://link.springer.com/10.1007/978-3-319-45444-3_11

60.   Duocastella M, Fernández-Pradas JM, Morenza JL, Zafra D, Serra P. Novel laser printing technique for miniaturized biosensors preparation. Sensors Actuators B Chem [Internet].   2010   Mar   4;145(1):596–600.   Available   from: https://linkinghub.elsevier.com/retrieve/pii/S0925400509009204

61.   Zhu W, Ma X, Gou M, Mei D, Zhang K, Chen S. 3D printing of functional biomaterials for tissue engineering. Curr Opin Biotechnol [Internet]. 2016 Aug;40:103–12. Available from: https://linkinghub.elsevier.com/retrieve/pii/S0958166916300702

62.   Schaffer CB, Nishimura N, Glezer EN, Kim AM-T, Mazur E. Dynamics of femtosecond laser-induced breakdown in water from femtoseconds to microseconds. Opt Express [Internet]. 2002 Feb 11;10(3):196. Available from: http://mazur-www.harvard.edu/

63.   Vogel A, Venugopalan V. Mechanisms of Pulsed Laser Ablation of Biological Tissues. Chem   Rev   [Internet].   2003   Feb;103(2):577–644.   Available   from: https://pubs.acs.org/doi/10.1021/cr010379n

64.   Rau KR, Guerra A, Vogel A, Venugopalan V. Investigation of laser-induced cell lysis using time-resolved imaging. Appl Phys Lett [Internet]. 2004 Apr 12;84(15):2940–2. Available from: http://aip.scitation.org/doi/10.1063/1.1705728

65.   Vogel A, Noack J, Hüttman G, Paltauf G. Mechanisms of femtosecond laser nanosurgery of cells and tissues. Appl Phys B [Internet]. 2005 Dec 15;81(8):1015–47. Available from: http://link.springer.com/10.1007/s00340-005-2036-6

66.   Vogel A, Linz N, Freidank S, Paltauf G. Femtosecond-Laser-Induced Nanocavitation in

Water: Implications for Optical Breakdown Threshold and Cell Surgery. Phys Rev Lett [Internet]. 2008 Jan 23;100(3):038102. Available from: https://link.aps.org/doi/10.1103/PhysRevLett.100.038102

67. Barnes PA, Rieckhoff KE. LASER INDUCED UNDERWATER SPARKS. Appl Phys Lett [Internet]. 1968 Oct 15;13(8):282–4. Available from: http://aip.scitation.org/doi/10.1063/1.1652611

68. Tinne N, Kaune B, Krüger A, Ripken T. Interaction Mechanisms of Cavitation Bubbles Induced by Spatially and Temporally Separated fs-Laser Pulses. Wang Y, editor. PLoS One [Internet]. 2014 Dec 11;9(12):e114437. Available from: https://dx.plos.org/10.1371/journal.pone.0114437

69. Fernández-Pradas JM, Florian C, Caballero-Lucas F, Sopeña P, Morenza JL, Serra P. Laser-induced forward transfer: Propelling liquids with light. Appl Surf Sci [Internet]. 2017 Oct;418:559–64. Available from: https://linkinghub.elsevier.com/retrieve/pii/S0169433216323339

70. Duocastella M, Patrascioiu A, Fernández-Pradas JM, Morenza JL, Serra P. Film-free laser forward printing of transparent and weakly absorbing liquids. Opt Express [Internet]. 2010 Oct 11;18(21):21815. Available from: https://www.osapublishing.org/oe/abstract.cfm?uri=oe-18-21-21815

71. Patrascioiu A, Fernández-Pradas JM, Palla-Papavlu A, Morenza JL, Serra P. Laser-generated liquid microjets: correlation between bubble dynamics and liquid ejection. Microfluid Nanofluidics [Internet]. 2014 Jan 19;16(1–2):55–63. Available from: http://link.springer.com/10.1007/s10404-013-1218-5

72. Juhasz T, Kastis GA, Suárez C, Bor Z, Bron WE. Time-resolved observations of shock waves and cavitation bubbles generated by femtosecond laser pulses in corneal tissue and water. Lasers Surg Med [Internet]. 1996;19(1):23–31. Available from: http://doi.wiley.com/10.1002/%28SICI%291096-9101%281996%2919%3A1%3C23%3A%3AAID-LSM4%3E3.3.CO%3B2-2

73. Zhang J, Hartmann B, Siegel J, Marchi G, Clausen-Schaumann H, Sudhop S, et al. Sacrificial-layer free transfer of mammalian cells using near infrared femtosecond laser

pulses. Witt SN, editor. PLoS One [Internet]. 2018 May 2;13(5):e0195479. Available from: https://dx.plos.org/10.1371/journal.pone.0195479

74. Blake J. Cavitation Bubbles Near Boundaries. Annu Rev Fluid Mech [Internet]. 1987 Jan 1;19(1):99–123. Available from: http://fluid.annualreviews.org/cgi/doi/10.1146/annurev.fluid.19.1.99

75. Pearson A, Cox E, Blake JR, Otto SR. Bubble interactions near a free surface. Eng Anal Bound Elem [Internet]. 2004 Apr;28(4):295–313. Available from: https://linkinghub.elsevier.com/retrieve/pii/S0955799703000791

76. Vogel A, Noack J, Nahen K, Theisen D, Busch S, Parlitz U, et al. Energy balance of optical breakdown in water at nanosecond to femtosecond time scales. Appl Phys B [Internet]. 1999 Feb 10;68(2):271–80. Available from: http://link.springer.com/10.1007/s003400050617

77. Ward B, Emmony DC. Interferometric studies of the pressures developed in a liquid during infrared-laser-induced cavitation-bubble oscillation. Infrared Phys [Internet]. 1991 Jan;32:489–515. Available from: https://linkinghub.elsevier.com/retrieve/pii/0020089191901386

78. Wan D-S, Rajadhyaksha M, Webb RH. Analysis of spherical aberration of a water immersion objective: application to specimens with refractive indices 1.33-1.40. J Microsc [Internet]. 2000 Mar;197(3):274–84. Available from: http://doi.wiley.com/10.1046/j.1365-2818.2000.00635.x

79. Zhang Z, Xiong R, Mei R, Huang Y, Chrisey DB. Time-Resolved Imaging Study of Jetting Dynamics during Laser Printing of Viscoelastic Alginate Solutions. Langmuir [Internet]. 2015 Jun 16;31(23):6447–56. Available from: https://pubs.acs.org/doi/10.1021/acs.langmuir.5b00919

80. Kang B, Shin J, Park H-J, Rhyou C, Kang D, Lee S-J, et al. High-resolution acoustophoretic 3D cell patterning to construct functional collateral cylindroids for ischemia therapy. Nat Commun [Internet]. 2018 Dec 20;9(1):5402. Available from: http://www.ncbi.nlm.nih.gov/pubmed/30573732

81. Zhang Z, Jin Y, Yin J, Xu C, Xiong R, Christensen K, et al. Evaluation of bioink printability for bioprinting applications. Appl Phys Rev [Internet]. 2018 Dec;5(4):041304. Available from: http://aip.scitation.org/doi/10.1063/1.5053979

82. van Hoeve W, Gekle S, Snoeijer JH, Versluis M, Brenner MP, Lohse D. Breakup of diminutive Rayleigh jets. Phys Fluids [Internet]. 2010 Dec;22(12):122003. Available from: http://aip.scitation.org/doi/10.1063/1.3524533

83. Emmadi N, Narumanchi H. Reinforcing Immutability of Permissioned Blockchains with Keyless Signatures' Infrastructure. In: Proceedings of the 18th International Conference on Distributed Computing and Networking [Internet]. New York, NY, USA: ACM; 2017. p. 1–6. Available from: https://dl.acm.org/doi/10.1145/3007748.3018280

84. Reitz RD. Mechanism of atomization of a liquid jet. Phys Fluids [Internet]. 1982;25(10):1730. Available from: https://aip.scitation.org/doi/10.1063/1.863650

85. Vahedi Tafreshi H, Pourdeyhimi B. The effects of nozzle geometry on waterjet breakup at high Reynolds numbers. Exp Fluids. 2003;35(4):364–71.

86. Dias A, Kingsley D, Corr D. Recent Advances in Bioprinting and Applications for Biosensing. Biosensors [Internet]. 2014 Apr 24;4(2):111–36. Available from: http://www.mdpi.com/2079-6374/4/2/111

87. Böcker W, Yin Z, Drosse I, Haasters F, Rossmann O, Wierer M, et al. Introducing a single-cell-derived human mesenchymal stem cell line expressing hTERT after lentiviral gene transfer. J Cell Mol Med [Internet]. 2008 Aug;12(4):1347–59. Available from: http://doi.wiley.com/10.1111/j.1582-4934.2008.00299.x

88. Kohler J, Popov C, Klotz B, Alberton P, Prall WC, Haasters F, et al. Uncovering the cellular and molecular changes in tendon stem/progenitor cells attributed to tendon aging and degeneration. Aging Cell. 2013;12(6):988–99.

89. Gioffredi E, Boffito M, Calzone S, Giannitelli SM, Rainer A, Trombetta M, et al. Pluronic F127 Hydrogel Characterization and Biofabrication in Cellularized Constructs for Tissue Engineering Applications. Procedia CIRP [Internet]. 2016;49(iii):125–32. Available from: http://dx.doi.org/10.1016/j.procir.2015.11.001

90. Graney PL, Ben-Shaul S, Landau S, Bajpai A, Singh B, Eager J, et al. Macrophages of diverse phenotypes drive vascularization of engineered tissues. Sci Adv [Internet]. 2020 May 1;6(18):eaay6391. Available from: http://www.ncbi.nlm.nih.gov/pubmed/32494664

91. Downer MC, Fork RL, Shank C V. Femtosecond imaging of melting and evaporation at a photoexcited silicon surface. J Opt Soc Am B [Internet]. 1985 Apr 1;2(4):595. Available from: https://www.osapublishing.org/abstract.cfm?URI=josab-2-4-595

92. Von Der Linde D, Sokolowski-Tinten K. Physical mechanisms of short-pulse laser ablation. Appl Surf Sci. 2000;154:1–10.

93. Domke M, Gavrilova A, Rapp S, Frentzen M, Meister J, Huber HP. Time-resolved microscopy reveals the driving mechanism of particle formation during ultrashort pulse laser ablation of dentin-like ivory. J Biomed Opt [Internet]. 2015 Jul 14;20(7):076005. Available from: http://biomedicaloptics.spiedigitallibrary.org/article.aspx?doi=10.1117/1.JBO.20.7.076005

94. Reuten R, Patel TR, McDougall M, Rama N, Nikodemus D, Gibert B, et al. Structural decoding of netrin-4 reveals a regulatory function towards mature basement membranes. Nat Commun [Internet]. 2016 Dec 30;7(1):13515. Available from: http://www.nature.com/articles/ncomms13515

95. Fidler IJ. Biological behavior of malignant melanoma cells correlated to their survival in vivo. Cancer Res [Internet]. 1975 Jan;35(1):218–24. Available from: http://www.ncbi.nlm.nih.gov/pubmed/1109790

96. Li H, Liu S, Li L. Rheological study on 3D printability of alginate hydrogel and effect of graphene oxide. Int J Bioprinting. 2016;2(2):54–66.

97. A. Erben, Hörning M, Hartmann B, Becke T, Eisler SA, Southan A, et al. Precision 3D-Printed Cell Scaffolds Mimicking Native Tissue Composition and Mechanics. Adv Healthc Mater. 2020;

98. Engelhardt S, Hoch E, Borchers K, Meyer W, Krüger H, Tovar GEM, et al. Fabrication of

2D protein microstructures and 3D polymer{\textendash}protein hybrid microstructures by two-photon polymerization. Biofabrication [Internet]. 2011;3(2):25003. Available from: https://doi.org/10.1088%2F1758-5082%2F3%2F2%2F025003

99. Patrascioiu A, Florian C, Fernández-Pradas JM, Morenza JL, Hennig G, Delaporte P, et al. Interaction between jets during laser-induced forward transfer. Appl Phys Lett [Internet]. 2014 Jul 7;105(1):014101. Available from: http://aip.scitation.org/doi/10.1063/1.4889802

100. Dumouchel C. On the experimental investigation on primary atomization of liquid streams. Exp Fluids [Internet]. 2008 Sep 22;45(3):371–422. Available from: http://link.springer.com/10.1007/s00348-008-0526-0

101. Payri R, Salvador FJ, Gimeno J, De La Morena J. Analysis of diesel spray atomization by means of a near-nozzle field visualization technique. At Sprays. 2011;21(9):753–74.

102. Zhang Z, Xiong R, Corr DT, Huang Y. Study of Impingement Types and Printing Quality during Laser Printing of Viscoelastic Alginate Solutions. Langmuir [Internet]. 2016 Mar 29;32(12):3004–14. Available from: https://pubs.acs.org/doi/10.1021/acs.langmuir.6b00220

103. Kennedy PK, Hammer DX, Rockwell BA. Laser-induced breakdown in aqueous media. Prog Quantum Electron. 1997;21(3):155–248.

104. Kennedy PK. A First-Order Model for Computation of Laser-Induced Breakdown Thresholds in Ocular and Aqueous Media: Part I—Theory. IEEE J Quantum Electron. 1995;31(12):2241–9.

105. Kennedy PK, Boppart SA, Hammer DX, Rockwell BA, Noojin GD, Roach WP. A First-Order Model for Computation of Laser-Induced Breakdown Thresholds in Ocular and Aqueous Media: Part II—Comparison to Experiment. IEEE J Quantum Electron. 1995;31(12):2250–7.

106. Sheik-Bahae M, Said AA, Wei TH, Hagan DJ, Van Stryland EW. Sensitive Measurement of Optical Nonlinearities Using a Single Beam. IEEE J Quantum Electron.

1990;26(4):760–9.

107.   Noack J, Vogel A. Laser-induced plasma formation in water at nanosecond to femtosecond time scales: calculation of thresholds, absorption coefficients, and energy density. IEEE J Quantum Electron [Internet]. 1999;35(8):1156–67. Available from: http://ieeexplore.ieee.org/document/777215/

108.   B. RS. The Resistance of the Air and Aviation. Nature [Internet]. 1913 Nov;92(2299):342–3. Available from: http://www.nature.com/articles/092342a0

109.   Wang W, Huang Y, Grujicic M, Chrisey DB. Study of Impact-Induced Mechanical Effects in Cell Direct Writing Using Smooth Particle Hydrodynamic Method. J Manuf Sci Eng [Internet]. 2008 Apr 1;130(2):021012. Available from: https://asmedigitalcollection.asme.org/manufacturingscience/article/doi/10.1115/1.2896118/462160/Study-of-ImpactInduced-Mechanical-Effects-in-Cell

110.   Wang W, Li G, Huang Y. Modeling of Bubble Expansion-Induced Cell Mechanical Profile in Laser-Assisted Cell Direct Writing. J Manuf Sci Eng [Internet]. 2009 Oct 1;131(5):505–14. Available from: https://asmedigitalcollection.asme.org/manufacturingscience/article/doi/10.1115/1.4000101/444816/Modeling-of-Bubble-ExpansionInduced-Cell

111.   Gudapati H, Yan J, Huang Y, Chrisey DB. Alginate gelation-induced cell death during laser-assisted cell printing. Biofabrication [Internet]. 2014 Aug 14;6(3):035022. Available from: https://iopscience.iop.org/article/10.1088/1758-5082/6/3/035022

112.   Gerstman BS, Thompson CR, Jacques SL, Rogers ME. Laser induced bubble formation in the retina. Lasers Surg Med [Internet]. 1996;18(1):10–21. Available from: https://onlinelibrary.wiley.com/doi/10.1002/(SICI)1096-9101(1996)18:1%3C10::AID-LSM2%3E3.0.CO;2-U

113.   Docheva D, Müller SA, Majewski M, Evans CH. Biologics for tendon repair. Adv Drug Deliv Rev [Internet]. 2015 Apr;84:222–39. Available from: http://dx.doi.org/10.1016/j.addr.2014.11.015

114.   Waggett AD, Benjamin M, Ralphs JR. Connexin 32 and 43 gap junctions differentially

modulate tenocyte response to cyclic mechanical load. Eur J Cell Biol [Internet]. 2006 Nov;85(11):1145–54.   Available   from: https://linkinghub.elsevier.com/retrieve/pii/S0171933506001178

115. McNeilly CM, Banes AJ, Benjamin M, Ralphs JR. Tendon cells in vivo form a three dimensional network of cell processes linked by gap junctions. J Anat [Internet]. 1996 Dec;189:593–600. Available from: https://pubmed.ncbi.nlm.nih.gov/8982835

116. Ralphs J., Waggett A., Benjamin M. Actin stress fibres and cell–cell adhesion molecules in tendons: organisation in vivo and response to mechanical loading of tendon cells in vitro.   Matrix   Biol   [Internet].   2002   Jan;21(1):67–74.   Available   from: https://linkinghub.elsevier.com/retrieve/pii/S0945053X01001792

Acknowledgements

Curriculum vitae

Personal data

Name:	Jun Zhang
Date of birth:	02. March 1989
Home address:	Schleissheimerstr. 165 80797 Munich
Telephone:	017670725346
E-Mail:	zhangjunj12@hotmail.com
Nationality:	Chinese

Education and degrees

PhD student Dr. rer. physiol.   01.2016 – present

University of Regensburg / Munich University of Applied Sciences
„Laser-induced transfer of human mesenchymal cells using near infrared femtosecond laser pulses for the precise configuration of cell nichoids"

M. Sc. Lasertechnik   09.2013 – 11.2015

Mittweida University of Applied Sciences
„Untersuchungen von laserinduzierten Plasmen in Bohrungen (LIBS)"
Laserinstitut Mittelsachsen

Dipl. Ing. Physikalische Technik   09.2009 – 04.2013

Coburg University of Applied Sciences and Arts
„Optimierung des Beschichtungsprozesses für Brillengläser"
Rupp & Hubrach Optik GmbH

B. Sc. Applied Physics   09.2007 – 09.2013

Zhejiang University of Science and Technology (China)

Awards

Nano Innovation Award 2021, third prize

Publications

J. Zhang, B. Hartmann, J. Siegel, G. Marchi, H. Clausen-Schaumann, S. Sudhop, H. P. Huber, "**Sacrificial-layer free transfer of mammalian cells using near infrared femtosecond laser pulses**". PLoS One 2018, 13, e0195479. https://doi.org/10.1371/journal.pone.0195479

J. Zhang, P. Byers, A. Erben, C. Frank, L. Schulte-Spechtel, M. Heymann, D. Docheva, H. P. Huber, S. Sudhop, H. Clausen-Schaumann, "**Single Cell Bioprinting with Ultrashort Laser Pulses**". Adv. Funct. Mater 2021, 2100066. DOI: 10.1002/adfm.202100066

J. Zhang, Y. Geiger, F. Sotier, S. Djordjevic, D. Docheva, S. Sudhop, H. Clausen-Schaumann, H. P. Huber, "**Single-cell bioprinting by using femto- and picosecond laser pulses**". (to be submitted to Special Issue "Advanced Laser Bio-Printing" in Micromachines)

J. Zhang, C. Frank, P. Byers, S. Djordjevic, D. Docheva, H. Clausen-Schaumann, S. Sudhop, H. P. Huber, "**Jet dynamics study of femtosecond laser-induced single-cell printing**" (manuscript in preparation)

Talks

Poster presentation: "Laser induced forward transfer (LIFT) of living cells using femtosecond laser pulses", Nanoscale Matter – Novel Concepts and Functions, 19.-23. September 2016, Venice, Italian

Oral presentation: "Laser induced forward transfer of living cells using femtosecond laser pulses", Conference on Lasers and Electro-Optics Europe & European Quantum Electronics Conference (CLEO/Europe-EQEC 2017), 25.-29. June 2017, Munich, Germany

Poster presentation: "Laser induced forward transfer of single cells", Annual Meeting of the German Society for Matrix Biology (DGMB), 28-30. March 2019, Regensburg, Germany

Oral presentation: "Femtosecond laser printing of single living human cells", European Conferences on Biomedical Optics (ECBO 2019), 23-27. June 2019, Munich, Germany

Flash presentation: "Femtosecond laser printing of single living mammalian cells", International conference on ultrafast optical science (Ultrafast Light 2020), 28. September - 02. October 2020, Moscow, Russia

Oral presentation: "Printing of living cells by using ultra-short laser pulses", Conference on Lasers and Electro-Optics Europe & European Quantum Electronics Conference (CLEO/Europe-EQEC 2021), 20-24 June 2021, Munich, Germany

Patent

Zhang J., Huber H., Clausen-Schaumann, H., Sudhop S., Docheva D.: *Laser-induced cell transfer and sorting.* International publication number: WO 2020/127640 A1. Published June 25. 2020

SELBSTÄNDIGKEITSERKLÄRUNG

"Ich, Jun Zhang geboren am 02. Märze1989 in JinHua, erkläre hiermit, dass ich die vorliegende Arbeit ohne unzulässige Hilfe Dritter und ohne Benutzung anderer als der angegebenen Hilfsmittel angefertigt habe.

Die aus anderen Quellen direkt oder indirekt übernommenen Daten und Konzepte sind unter Angabe der Quelle gekennzeichnet. Insbesondere habe ich nicht die entgeltliche Hilfe von Vermittlungs- bzw. Beratungsdiensten (Promotionsberater oder andere Personen) in Anspruch genommen.

Die Arbeit wurde bisher weder im In- noch im Ausland in gleicher oder ähnlicher Form einer anderen Prüfungsbehörde vorgelegt.

Ort, Datum   eigenhändige Unterschrift

                                              des Promovenden